Title

REMOTE SENSING OF WATER STRESS IN ALMOND TREES USING UNMANNED AERIAL VEHICLES

Author

Zhao, Tiebiao

Publication Date

2018

UNIVERSITY OF CALIFORNIA, MERCED

REMOTE SENSING OF WATER STRESS IN ALMOND TREES USING UNMANNED AERIAL VEHICLES

by

Tiebiao Zhao

A dissertation submitted in partial satisfaction of the
requirements for the degree of
Doctor of Philosophy

in

Mechanical Engineering

Committee in charge:
Professor YangQuan Chen, Advisor
Professor Reza Ehsani
Dr. Dong Wang

The dissertation of Tiebiao Zhao is approved:

YangQuan Chen, Advisor	Date
Reza Ehsani	Date
Dong Wang	Date

University of California, Merced

To my wife, Yuan Li

ACKNOWLEDGEMENTS

I would like to thank my advisor, Prof. YangQuan Chen first. Thank you for opening the door so that I can appreciate the fun of doing research. Thank you for helping me find the place where I feel happy, peaceful and meaningful. Thanks for your patience, vision, insights, motivation and guidance. Thanks for those great discussions. Though some happened a while ago, I still remember how excited I was.

Thanks go to my academic committee members, Prof. Reza Ehsani and Dr. Dong Wang for their constructive and insightful discussions and suggestions on my research. Thanks go to David Doll for leading and coordinating the project, providing domain knowledge and comments. Thanks go to my master advisor Prof. Meisheng Xue in University of Science and Technology of China and undergraduate advisor Prof. Zhenbin Du in Yantai University for their help on my early study.

Thanks go to Andrew Ray, Cameron At Zuber, Stella Zambrzuski and the undergraduate researchers Andreas Anderson, Yoni Shchemelinin, Jacob Clark, Allan Murillo, Laura Barbosa, Christopher Currier, Zackary Baskin, Alejandro Sanchez, Gregorio Nunez, and Dong Sen Yan for data collection and preprocessing. Thanks go to my lab colleagues Dr. Brandon Stark, Dr. Zhuo Li, Brendan Smith, Dr. Duval Johnson, Guoxiang Zhang, Sina Dehghan, Derek Hollenbeck and Haoyu Niu, Prof. Qi Yang, and Prof. Jianxin Liu.

Thanks go to my wonderful wife for her love, care, support and sacrifice. Thanks go to my parents for their continuous support and understanding.

The work in this dissertation was supported by UCANR Competitive Grants project No. 13-2628 (2014-2019), San Joaquin Valley Agricultural Sciences Center Water Management Research, and Yara North America Almond Fellowship 2016-2017 and 2017-2018.

TABLE OF CONTENTS

Chapter

LIST OF FIGURES

LIST OF TABLES

CURRICULUM VITAE

EDUCATION

- M.S. in Control Theory and Control Engineering, University of Science and Technology of China (Hefei, Anhui, China), 2012.
- B.S. in Automation, Yantai University (Yantai, Shandong, China), 2009.

HONORS AND AWARDS

- UC Merced 2017-2018 Yara North America Almond Fellowship
- UC Merced 2017-2018 Summer Research Travel Fellowship
- UC Merced 2018 Spring Mechanical Engineering's Dissertation Year Fellowship
- UC Merced 2016-2017 ME Bobcat Fellowship
- UC Merced 2016-2017 Yara North America Almond Fellowship
- The honorable award in Food System Innovations category in Big Ideas Competition @UC Berkeley, 2016
- UC Merced 2015-2016 ME Bobcat Fellowship
- The 3rd place in Food System Innovations category in Big Ideas Competition @UC Berkeley, 2015
- UC Merced 2015 Summer ME Bobcat Fellowship

JOURNAL PAPERS

1. T. Zhao, B. Stark, Y. Chen, A. L. Ray, D. Doll, Challenges in water stress quantification using small unmanned aerial system (SUAS): Lessons from a growing season of almond, Journal of Intelligent & Robotic Systems 88 (2-4) (2017) 721–735.

2. J. Liu, T. Zhao, Y. Chen, Maximum power point tracking with fractional order high pass filter for proton exchange membrane fuel cell, IEEE/CAA Journal of Automatica Sinica 4 (1) (2017) 70–79.
3. Q. Yang, D. Chen, T. Zhao, Y. Chen, Fractional calculus in image processing: a review, Fractional Calculus and Applied Analysis 19 (5) (2016) 1222–1249.

CONFERENCE PAPERS

1. T. Zhao, Y. Yang, H. Niu, D. Wang, Y. Chen, Comparing U-Net convolutional network with mask R-CNN in the performances of pomegranate tree canopy segmentation, in: the Proceeding of Multispectral, Hyperspectral, and Ultraspectral Remote Sensing Technology, Techniques and Applications VII, Vol. 10780, International Society for Optics and Photonics, 2018, p. 107801J.
2. S. Dehghan, T. Zhao, Y. Zhao, J. Yuan, A. Ates, Y. Chen, PID2018 benchmark challenge: Model predictive control with conditional integral control using a general purpose optimal control problem solver-RIOTS, arXiv preprint arXiv:1806.01976.
3. T. Zhao, A. Koumis, H. Niu, D. Wang, Y. Chen, Onion irrigation treatment inference using a low-cost hyperspectral scanner, in: the Proceedings of Multispectral, Hyperspectral, and Ultraspectral Remote Sensing Technology, Techniques and Applications VII, Vol. 10780, International Society for Optics and Photonics, 2018, p. 107800D.
4. T. Zhao, H. Niu, E. de la Rosa, D. Doll, D. Wang, Y. Chen, Tree canopy differentiation using instance-aware semantic segmentation, in: the Proceedings of 2018 ASABE Annual International Meeting, American Society of Agricultural and Biological Engineers, 2018, p. 1.
5. T. Zhao, H. Niu, A. Anderson, Y. Chen, J. Viers, A detailed study on accuracy of uncooled thermal cameras by exploring the data collection workflow, in: the Proceedings of Autonomous Air and Ground Sensing Systems for Agricultural Optimization and Phenotyping III, Vol. 10664, International Society for Optics and Photonics, 2018, p. 106640F.
6. T. Zhao, C. Currier, A. Bonnin, G. Mellos, N. Martinez, Y. Chen, Low cost autonomous battery replacement system for quadrotor small unmanned aerial systems (SUAS) using 3D printing components, in: the Proceedings of 2018 International Conference on Unmanned Aircraft Systems (ICUAS2018), IEEE, 2018, pp. 103–107.

7. T. Zhao, Z. Wang, Q. Yang, Y. Chen, Melon yield prediction using small unmanned aerial vehicles, in: the Proceedings of Autonomous Air and Ground Sensing Systems for Agricultural Optimization and Phenotyping II, Vol. 10218, International Society for Optics and Photonics, 2017, p. 1021808.
8. T. Zhao, D. Doll, Y. Chen, Better almond water stress monitoring using fractional-order moments of non-normalized difference vegetation index, in: the Proceedings of 2017 ASABE Annual International Meeting, American Society of Agricultural and Biological Engineers, 2017, p. 1.
9. T. Zhao, D. Doll, D. Wang, Y. Chen, A new framework for UAV-based remote sensing data processing and its application in almond water stress quantification, in: the Proceedings of 2017 International Conference on Unmanned Aircraft Systems (ICUAS2017), IEEE, 2017, pp. 1794–1799.
10. T. Zhao, Y. Chen, A. Ray, D. Doll, Quantifying almond water stress using unmanned aerial vehicles (UAVs): correlation of stem water potential and higher order moments of non-normalized canopy distribution, in: the Proceedings of ASME 2017 International Design Engineering Technical Conferences and Computers and Information in Engineering Conference, American Society of Mechanical Engineers, 2017, pp. V009T07A058–V009T07A058.
11. T. Zhao, Z. Li, Y. Chen, Fractional order nonlinear model predictive control using RIOTS_95, in: the Proceedings of 2014 International Conference on Fractional Differentiation and Its Applications (ICFDA2014), IEEE, 2014, pp. 1–6.
12. B. Shang, J. Liu, T. Zhao, Y. Chen, Fractional order robust visual servoing control of a quadrotor UAV with larger sampling period, in: the Proceedings of 2016 International Conference on Unmanned Aircraft Systems (ICUAS2016), IEEE, 2016, pp. 1228–1234.
13. B. Stark, T. Zhao, Y. Chen, An analysis of the effect of the bidirectional reflectance distribution function on remote sensing imagery accuracy from small unmanned aircraft systems, in: the Proceedings of 2016 International Conference on Unmanned Aircraft Systems (ICUAS2016), IEEE, 2016, pp. 1342–1350.
14. T. Zhao, B. Stark, Y. Chen, A. Ray, D. Doll, More reliable crop water stress quantification using small unmanned aerial systems (SUAS), IFAC-PapersOnLine 49 (16) (2016) 409–414.
15. T. Zhao, M. Cisneros, Q. Yang, Y. Zhang, Y. Chen, Almond canopy detection and segmentation using remote sensing data drones, in: the Proceedings of the

13th International Conference on Precision Agriculture (unpaginated, online), Monticello, IL, International Society of Precision Agriculture, 2016.

16. T. Zhao, B. Stark, Y. Chen, A. L. Ray, D. Doll, A detailed field study of direct correlations between ground truth crop water stress and normalized difference vegetation index (NDVI) from small unmanned aerial system (SUAS), in: the Proceedings of 2015 International Conference on Unmanned Aircraft Systems (ICUAS2015), IEEE, 2015, pp. 520–525.

17. J. Liu, T. Zhao, Y. Chen, Maximum power point tracking of proton exchange membrane fuel cell with fractional order filter and extremum seeking control, in: the Proceedings of ASME 2015 International Design Engineering Technical Conferences and Computers and Information in Engineering Conference, American Society of Mechanical Engineers, 2015, pp. V009T07A026–V009T07A026.

18. B. Smith, B. Stark, T. Zhao, Y. Chen, An outdoor scientific data drone ground truthing test site, in: the Proceedings of 2015 International Conference on Unmanned Aircraft Systems (ICUAS2015), IEEE, 2015, pp. 436–443.

19. Z. Li, T. Zhao, Y. Chen, A low cost research platform for modeling and control of multi-input multi-output fractional order dynamic systems, in: the Proceedings of 2014 International Conference on Fractional Differentiation and Its Applications (ICFDA2014), IEEE, 2014, pp. 1–6.

LIST OF ABBREVIATIONS

AIC	Akaike Information Criterion
AGL	Above Ground Level
ANN	Artificial Neural Network
ANVOA	Analysis of Variance
ASM	Angular Second Moment
ATP	Adenosine Triphosphate
BIC	Bayesian Information Criterion
BRDF	Bidirectional Reflectance Distribution Function
Chl	Chlorophyll
CON	Contrast
COR	Correlation
COTS	Commercial-Off-The-Shelve
CWSI	Crop Water Stress Index
DI	Derivative Indices
DN	Digital Number
DVI	Difference Vegetation Index
ENT	Entropy
ET	Evapotranspiration
FWHM	Full Width At Half Maximum
GCP	Ground Control Point

GI	Green Index
HSV	Hue, Saturation, and Value
IDM	Inverse Different Moment
JPEG	Joint Photographic Expert Group
KL	Kullback-Leibler
GEMI	Global Environment Monitoring Index
GLCM	Gray Level Concurrence Matrix
Gs	Stomatal Conductance
GSAVI	Generalized Soil-Adjusted Vegetation Index
GSD	Ground Sample Distance
ISO	International Organization of Standardization
KNN	K-Nearest Neighbors
LASSO	Least Absolute Shrinkage And Selection Operator
LDA	Linear Discriminant Analysis
NADPH	Nictinamide Adenine Dinucleotide Phosphate
NIR	Near Infrared
ND	Normalized Difference
NDGVI	Normalized Difference Greenness Vegetation Index
NDRI	Normalized Difference Red-Edge Index
NDVI	Normalized Difference Vegetation Index
MADVI	Modified Soil Adjusted Vegetation Index
MAE	Mean Absolute Error
MODIS	Moderate Resolution Imaging Spectroradiometer
MRI	Magnetic Resonance Imaging
MSE	Mean Square Error

OSAVI	Optimized Soil Adjusted Vegetation Index
PCA	Principal Component Analysis
PCR	Principal Component Regression
PLS	Partial Least Squares
PLSR	Partial Least Squares Regression
PRI	Photo-Chemical Reflectance Index
PST	Polar Stockwell Transform
RDVI	Renormalized Difference Vegetation Index
RGB	Red-Green-Blue
RI	Red-edge Indices
RMSE	Root Mean Square Error
RSS	Residual Sum Of Squares
RVI	Ratio Vegetation Index
SIPI	Structure Independent Pigment Index
SIF	Solar-Induced Fluorescence
SR	Simple Ratio
SWIR	Short-Wave Infrared
SWP	Stem Water Potential
TCARI	Transformed Chlorophyll Absorption In Reflectance Index
TIR	Thermal Infrared
TIF	Tagged Image File Format
UAV	Unmanned Aerial Vehicle

ABSTRACT

The technologies of unmanned aerial vehicles (UAVs) and miniature cameras have been improved significantly in the last decade. It becomes more and more popular to use UAVs and onboard cameras to collect high resolution multispectral images with better operation flexibility. Although remote sensing using satellites or field scanners has been researched for many years, there is still lack of a workflow to fully explore the benefits of high resolution images from UAV-based remote sensing. In this dissertation, three key parts of the workflow are discussed: extraction of region of interest from high resolution images, extraction of related features for further classification or regression problems and optimization of UAV-based remote sensing practices, using almond tree water status detection as a case study.

Unlike satellites providing low resolution images, or field scanners with limited field of view, UAV-based remote sensing platforms can collect very high resolution images with flexible temporal resolution and spectral band configuration. To extract the region of interest more accurately, two types of methods are evaluated. One uses manual features such as color, texture and morphological features, and the other is based on the latest deep learning based instance-segmentation models.

After accurate extraction of region of interest, the next step is to extract application related information from these high resolution images. A methodology is proposed to convert the feature extraction problem to a dimensionality reduction problem. According to this methodology, moments, histograms and traditional dimensionality reduction methods are discussed based on the performances of irrigation treatment classification and almond tree variety classification, and stem water potential (SWP) regression. For SWP regression, different regression regularization methods are also experimented to extract more information from given tree canopy pixels.

Finally, best remote sensing practices are discussed using irrigation treatment classification and variety classification as reference applications. Effects of spatial resolution, spectral configuration, band-to-band registration and image formats are evaluated in terms of classification accuracies.

Chapter 1

INTRODUCTION

1.1 Background

1.1.1 Water and Plants

Water plays an important role in plants [5]. Water is a constituent of cell protoplasm and it weighs over 90% of fresh weights in plants. Water can serve as a solvent, where nutrients are dissolved and then absorbed by plants.

In plants, water is pulled into the roots by transpiration, a process that water evaporates via the stomata of leaves [6]. Nearly 90% of water in plants is used in transpiration, with the remaining 10% used for photosynthesis and plant growth. While water moves from the soil into roots, along stems and into leaves, nutrients and minerals from the roots and sugars produced by photosynthesis are also transported to different areas of the plants. As water vapors leave leaf stomata, they take lots of energy from surroundings, cool down plant tissues and help maintain proper temperature for plants.

Transpiration also helps maintain turgor pressure [7]. The hydrostatic system is generated when water moves due to osmosis between semipermeable membranes. The turgor pressure is the key for plants to interact with the environment. For example, blood pressure in animals is around 0.003 Mpa, whereas turgor pressure is around 0.6 Mpa. This is central to many plant functions, such as growth, transport, movement and cell metabolism. Plant growth is driven by cell extension, because of the forces generated by turgor pressure. Plant movements such as turning leaves and flowers to track the sun to maximize photosynthesis or pollination are made by turgor variation in different parts of the stems. Another important process driven by turgor is the stomatal opening and closing. When water is available to plants, turgor is increased and stomatal pores are opened. When water is scarce, pores are closed to save water. It also helps transport proteins and pump solutes into plant cells.

Water is also required in plants photosynthesis, a process that plants produce their food using light energy, carbon dioxide and water [8]. Water is directly involved in the photosynthesis and indirectly in the food creation, helping plants avoid dehydration. During the photosynthesis process, electrons are excited by light energy and have reaction with the pigment chlorophyll. As a result, the light energy is converted into adenosine triphosphate (ATP) and nictinamide adenine dinucleotide

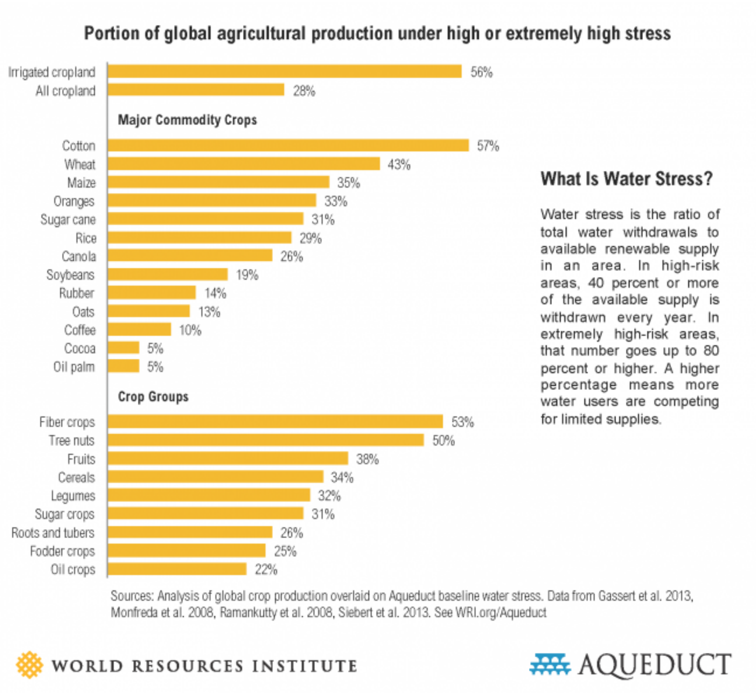

What Is Water Stress?

Water stress is the ratio of total water withdrawals to available renewable supply in an area. In high-risk areas, 40 percent or more of the available supply is withdrawn every year. In extremely high-risk areas, that number goes up to 80 percent or higher. A higher percentage means more water users are competing for limited supplies.

Sources: Analysis of global crop production overlaid on Aqueduct baseline water stress. Data from Gassert et al. 2013, Monfreda et al. 2008, Ramankutty et al. 2008, Siebert et al. 2013. See WRI.org/Aqueduct

Figure 1.1: Portion of cropland under water stress [1].

phosphate (NADPH). Water is required to provide the hydrogen, which is combined with carbon dioxide in the form of sugar. Gas exchanges such as carbon dioxide uptake and oxygen release occur along with water transpiration through leaf stomata. When plants are under stress during dry seasons, stomata are closed to prevent water loss. As a result, the photosynthesis slows down or even stops [9].

If water evaporation exceeds absorption from the soil, plants experience water stress [10]. Even short-term water deficits may affect growth processes [11]. On the contrary, too much water in the soil prevents plants from getting enough oxygen and even makes roots rotted [12]. Plant species vary in water use and their response to water stress. A mature almond orchard for example, though a drought tolerant species [13, 14], can exhibit an evapotranspiration rate 50% greater than that of cotton [15, 16].

1.1.2 Agriculture Is Under Water Stress

However, water is a limited resource. Water crises have become the biggest concern for the next 10 years [17]. According to Hoekstra's study, two-thirds of the population all over the world are under severe water scarcity no less than 1 month during the year [18]. Agriculture is under stress too. As indicated in Fig. 1.1, more than a quarter of global cropland is under high water stress. The portion of irrigated crop land under stress is more than 50%. Agriculture already consumes more than 70 % of water withdrawn globally. In Unites States, around one third was under drought in April, 2018 [19] and the size of the area in drought was as three times large as that in 2017. In California, even after the long-lasting drought ended in September, 2017, nearly 63% of the state was still experiencing drought conditions in October, 2018 [20]. Considering water competition from urbanization and industrialization, 25 % to 40 % water in stressed regions will be reallocated among different sections based on productivity and employment activities [21]. Because agriculture takes such a big portion of water use, it is highly probable that water in agriculture will be allocated from agriculture to other use. On the contrary, the population is predicted to expand to over 10 billion by 2050. To supply the growing population and increasing food consumption, agriculture production needs to rise 70% by 2050. To resolve this quandary, we need to produce more food with less water. So it is imperative to come up with better water management to increase water use efficiency to achieve "more crop per drop" [22].

1.1.3 UAV-based Remote Sensing

Agriculture technologies such as precision agriculture, drip irrigation etc. promise to increase the global yield as much as 67% by 2050 [23]. For example, drip irrigation helped growers save water required for maize production by 50% and 86% compared with sprinkler and surface irrigation respectively [24]. Precision agriculture is a management system based on information and technology and focuses on the optimal use of the data of soil, crops, nutrients, pests, moisture or field for optimum profitability, sustainability and the protection of the environment (USDA). Through customized management input, precision agriculture improves crop productivity, water efficiency and farm profitability [25] and leads to better environment sustainability [26–28]. By monitoring soil moisture status, one of the precision agriculture practices, over 25% of water savings were achieved in citrus orchard in Spain and wheat fields in China, where irrigated agriculture has already been under stress [24]. Studies showed that, if adequate and timely irrigation is applied based on realtime water status monitoring , both yield and quality of plants will be improved without consuming extra amount of water [29].

Generally, the operation of precision agriculture includes data collection, variability mapping, decision making and field practice. Remote sensing, involved in the first three stages, is the key part in the whole process [30,31]. The use of remote sensing based on satellite images in precision agriculture is limited by low spatial resolution and/or poor acquisition times [30, 32]. Moreover, the use of manned planes is limited by operational complexity and high cost [32–34]. There was a study applying remote sensing in melon fields for pest monitoring [35]. However,

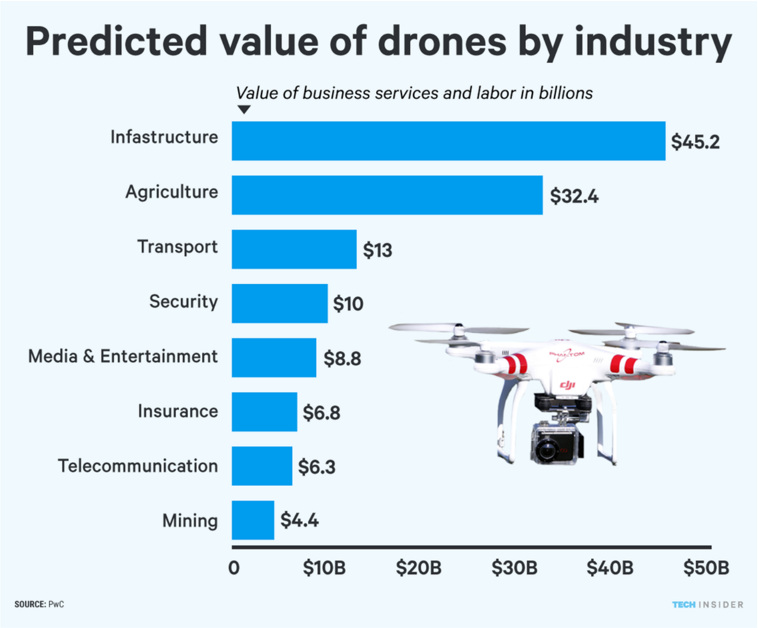

Figure 1.2: Predicted value of drones in industries [2]

due to low resolution (10 m/pixel and 7 days for both cases) the imagery did not show immediate help in pest management.

Unmanned aerial vehicles (UAVs), also called drones, as one of ten breakthrough technologies by MIT Technology Review in 2014 [36], have become increasingly popular. According to a FAA report in March 2018 [37], commercial drones will be quadrupled in the next five years, from 110,604 in 2017 to 451,800 by 2022. Drone technologies are estimated to provide service worth $127 billion, disrupting many industries such as infrastructure, agriculture, and transport [2], as shown in Fig. 1.2.

Drones are becoming very low cost. Small UAVs equipped with cameras are less than $1000. Drones are easy to fly. Unlike old radio-controlled aircrafts, with kinds of sensors such as accelerators, gyros, GPS modules and micro-processors, these new model aircrafts are controlled by autopilots. They can take off, land, fly autonomously and trigger cameras to capture images according to pre-programmed flight paths. Growers can fly the drones and monitor fields monthly, weekly, daily and even hourly, whereas traditionally they need to wait for satellites passing by the fields, or turn to manned aircrafts with a much higher price.

Recently, small UAVs have shown great potential to collect up-to-date images for decision making in agriculture. Studies about UAVs, the smart farmer companion, have been reported in many crops, like rice [38], wheat [39], corn [40], turf grass [41], vineyard [42] and coffee [43]. It is promising that UAV-based remote sensing can monitor crops, provide inter- and intra- field variability of crops information [44], and help optimize irrigation schedule and increase water use efficiency.

1.2 Literature Review

1.2.1 Crop Feature Extraction from Aerial Images

Popular technologies to measure physiological plant response under water stress include stomatal conductance [45], water potential [46, 47], canopy temperature [48–51], chlorophyll (Chl) fluorescence [45], sap flow measurement [52, 53], dendrometry [54], gas exchanges [55], net assimilation [56], air vapor pressure dificit [57] and leaf vibration [58], etc.

Currently, there are four types of vegetation indices for crop monitoring [59], including simple ratio (SR), normalized difference (ND), red-edge indices (RI) and derivative indices (DI) [60, 61]. Red-edge indices use the reflectance of the inflection point in the range from 680 nm to 780 nm [62], because of a strong chlorophyll absorption in the red band and a high relfectance in the near-infrared (NIR) band. Derivative indices are suggested to overcome variations due to bidirectional reflectance distribution function (BRDF), leaf surface scattering and background noise [63].

Water potential has been applied effectively to monitor crop water stress [64–66]. Research has shown that it can serve as an indicator in many fruit tree species [67] to quantify both short-term and mid-term plant response to water stress.

It is, however, labor-intensive and time-consuming to take accurate water potential measurements using pressure chambers [68]. Traditionally, to understand water stress in the field level, growers have to measure some sentinel plants, assumed to represent the whole field. There are, however, heterogeneous biophysical features spatially in fields, trees and even leafs [69]. It is hard to obtain the spatial variability of water stress by just measuring sample trees [29, 70, 71]. Remote sensing based methods have been proposed to access the spatial distribution of water stress in the larger field to replace field measurements [72].

Higher spatial and temporal resolution on water status monitoring is necessary to optimize irrigation. Many studies have been conducted on water stress detection using different sensors such as multispectral or hyperspectral cameras, thermal cameras and fluorescence sensors based on UAVs.

The most popular index using canopy temperature to quantify water stress is crop water stress index (CWSI) [73]. CWSI showed good correlations with SWP in peach trees [74], pistachio trees [75], almond trees [76] and vineyards [77]. In [56], tree canopy pixels were divided into four different regions according to the 25th, 50th and 75th quartiles. Correlation between CWSI calculated using the pixels of the entire crown, the region under the 25th quartile, the region under 50th quartile, the region above 75th quartile and leaf stomatal conductance (Gs) was analyzed. Relationships with Gs were improved remarkably, using colder areas pixels from under the 25th quartile and the 50th quartile, and yielding the coefficients of $R^2 = 0.77$ and $R^2 = 0.78$. CWSI was used to map spatial water status across using aerial thermal images at different imaging time and resolution [78]. Experiments showed that the relationship between CWSI and leaf water potential was the best around noon with the highest resolution. In the early morning, it was hard to separate canopies from the soil in thermal images. The sensitivity analysis of varying pixel resolution showed that R^2 decreased as the resolution increased from 0.3 m to 2.0 m. This was explained that the lower resolution of pixels made it hard to differentiate canopies from soil and therefore the canopy temperature was less accurate. Studies showed temperature difference between canopies and air correlated well with SWP in almond trees [76] and peach trees [51]. In [79], a hand-operated thermal camera was used to evaluate the feasibility of canopy temperature as a water stress indicator in citrus and persimmon trees during two seasons. Studies were conducted to explore the relationship between standard deviation of the canopy temperature and CWSI based on aerial images with resolution 2.5 m/pixel [80] using cotton crops under different irrigation treatments. For both low and high stress treatments, the standard deviation was not well correlated with CWSI. For moderately stressed crops, the standard deviation had a linear relation with field-scale CWSI. Furthermore, the relationship between standard deviation and CWSI was compared at different grid size. The coefficient of determination was reduced from 0.77 to 0.4 when the scale was aggregated from 5 m to 90 m. The use of thermal cameras was investigated to monitor water stress of grape vines in [81] in the scale of plots. It was shown that the variability of stomatal conductance increased when crop water stress increased. However, the standard deviation of canopy temperature was weakly correlated with stomatal conductance. Simulations in [82] demonstrated that spatial averaging of the pixel DN value in the field of view decreased the sensitivity of the thermal measurement of water stress. Studies in [83] showed that when the standard deviation of midday canopy temperature in a corn plot was over 0.3°C , some plants experienced water stress. In addition, within-crown structure of canopy temperature showed a good relationship with physiological measurements. Studies have demonstrated that canopy heterogeneity was also a good indicator for early plant water stress [82, 83].

Xanthophyll, chlorophyll and structure related spectral indices were used to detect water stress [84, 85]. In [85], the vegetation indices such as CWSI, photochemical reflectance index (PRI) [86], normalized PRI, red edge ratio (ρ_{700}/ρ_{670}), transformed chlorophyll absorption in reflectance index (TCARI) normalized by optimized soil adjusted vegetation index (OSAVI) [87], were obtained via the average measurement at the object level in five different fruit tree species from aerial images. Relationships between SWP, stomatal conductance and those vegetation indices were analyzed for the five fruit tree species, including almond trees, apricot trees, peach trees, lemon trees and orange trees. The temperature and PRI were the first and second most sensitive to water stress conditions in all the fruit trees except apricot trees. Normalized PRI was least sensitive to water stress. Experiments in maize crops [84] showed that red-edge position was sensitive to water conditions in terms of leaf water content, whereas PRI and normalized difference vegetation index (NDVI) were sensitive indices to productive indicators. The temperature was measured using a hand-held infrared thermometer, and the reflectance was measured with a field spectroradiometer. PRI, visible bands, the red-edge band and the NIR band within the light spectrum were able to detect water stress in the canopy level [88], considering the mechanism that water stress slows or even stops photosynthesis process [89].

It has been demonstrated that solar-induced fluorescence (SIF), associated with the photosynthetic reaction can indicate vegetation stress [90,91]. Imagery captured with both narrow bands (below 1 nm full width at half maximum (FWHM)) and broader bandwiths (5-7 nm) can detect fluorescence signal, so it can serve to monitor photosynthesis status [92].

Artificial neural network (ANN), capable of modeling complex systems, was used in water status monitoring for vine crops [93]. Compared with linear regression models, it yielded a higher accuracy with $R^2 = 0.96$ to predict SWP using soil moisture. In [94], an ANN model was built to estimate vineyard SWP, using multispectral images in the bands 550, 570, 670, 700 and 800 nm, achieving the performance with the coefficient of determination $R^2 = 0.56 - 0.87$, root mean quare error (RSME) of 0.12 MPa and mean absolute error (MAE) of 0.1 Mpa. It was in the plot level, with six plants in each plot. The ANN model was applied in every canopy pixel to calculate SWP. Then the field was classified into four stress levels according to the predicted SWP, including non-water stress, moderate water stress, strong water stress and severe water stress.

Five bands were used to predict SWP for vineyards [95] using ANN models [96]. Two ANN models were applied to predict SWP. For every pixel at a spatial resolution of 10 cm/pixel, ten vegetation indices were calculated first, including difference vegetation index (DVI) [97], green index (GI) [98], modified soil adjusted vegetation index (MADVI) [99], NDVI [100], normalized difference greenness vegetation index (NDGVI) [101], normalized difference red-edge index (NDRI) [102], OSAVI [103], red green ratio index [101], renormalized difference vegetation index (RDVI) [104] and simple ratio (SR) [105]. At the pixel level, the first ANN model was composed of the above ten indices as inputs and SWP as outputs and the second ANN model included ten indices as inputs and three stress levels as outputs.

Five vegetation indices were taken to differentiate effects of different treatments including two light treatments and three nitrogen treatments [106] in Engelmann spruce. Experiments showed that the reflectance at 550 nm [107], red edge position and simple ratio were sensitive to both light and nitrogen treatments in terms of chlorophyll concentration. Structure independent pigment index (SIPI) [108], and PRI were related to chlorophyll and carotenoid concentrations. PRI was sensitive to both treatments, whereas SIPI was just affected by nitrogen treatment.

Effects of water stress were quantified using leaf spectrum measurement. A one-way analysis of variance (ANOVA) was used to assess the effect of irrigation treatment on both plant physiological parameters and spectral measurements [109]. In [70], the usefulness of high-spatial NDVI and soil electrical properties to define water stress zones was evaluated. Significant differences in mean values of vine physiological features, yield and water status were observed in NDVI based zones with three years' experiments according to non-parametric Krushkal-Wallis test.

In [59], 144 broad-band and narrow-band vegetation indices were evaluated and compared to predict chlorophyll content within two years at both the leaf scale and the canopy scale. Both spectral measurements were made in the scale of both leaves and canopies. The canopy-scale measurement was made 1 meter above each quadrat of the size 50 cm by 50 cm. The relationship at the canopy level was generally stronger than that of the leaf scale, because leaf samples were collected when chlorophyll in plants was uniform. Broad-band indices were found to be as effective as narrow-band indices. Both narrow-band and broad-band indices were stronger at the canopy than the leaf level in terms of temporal performance, the capability to predict chlorophyll content variability between years.

1.2.2 Crop Segmentation in Aerial Images

Soil background exerts considerable influence on vegetation indices of crops with partial canopy [110]. For example, the ratio vegetation index (RVI) and NDVI increase when given crops are planted in darker soil [111–113]. In addition, temperature based indices also rely on accurate segmentation of canopies from soil background. The canopy edge and soil pixels usually have higher temperature, so inclusion of non-canopy pixels can introduce significant errors in CWSI [29].

Previously, limited by low spatial resolution, adjusted indices were proposed to address this issue such as TSAVI [114], SAVI [112], OSAVI [103], and generalized soil-adjusted vegetation index (GSAVI) [115]. These indices minimize soil background related effects by introducing a soil-adjustment parameter, which has to be determined empirically case by case.

With increased imagery resolution, it is possible to differentiate crop from soil, and sunlit parts from shaded parts. Various methods were introduced to separate crops from soil background. Visible images were used to create a binary mask of potato canopies based on statistic descriptions of illumination levels first [116], and the mask was used for the co-registered thermal images to calculate temperature of sunlit leaves [117]. Then sunlit canopies were separated from shaded canopies, mixture of canopies and soil according to NDVI. An empirical temperature threshold was applied to distinguish canopy pixels in thermal images [118]. NDVI was used to differentiate vegetation from soil background, where the NDVI threshold was the lowest point between two peaks of NDVI distribution [94, 119]. This method was further compared with an ANN based method [120] and results showed the performances of these two methods were similar. Because canopies are cooler than their surroundings, canopies objects can be considered as basins. Inspired by this, watershed algorithms were used for canopy segmentation in thermal images [56, 71, 121]. Edge detection methods were also used for canopy detection. Experiments [29] showed that Sobel and Canny methods were better than Prewitt and Robert methods.

1.3 Motivation

UAV-based remote sensing has lower altitude and more flexible operation. Though traditional methods for satellite-based remote sensing could be applied as well without surprise, as the reviewed studies show. Lower altitude remote sensing makes it possible to collect much higher resolution images. However, there is still lack of a workflow to fully leverage such high resolution for better plant health monitoring. Throughout the workflow, three key problems are as follows,

1. how to extract the region of interest with higher accuracy,
2. how to extract related features from these high resolution images for further regression or classification,
3. what is the best remote sensing practice for specific applications, i.e., the best spatial resolution and the best spectral configuration.

In this dissertation, these three problems will be discussed using almond tree water stress monitoring as a case study.

1.4 Dissertation Contributions

Major contributions of this dissertation are as follows:

1. Developed a method to segment tree canopies using manual features such as color, texture, morphological features.
2. Developed a deep-learning-based instance-segmentation model to segment tree canopies.
3. Proposed a new methodology that each band or vegetation index can be considered as an image layer and that each pixel of a tree canopy in a layer represents an observation for the tree.

4. Proposed moments- and histograms-based dimensionality reduction methods to extract information from UAV-based high resolution images at the tree level.

5. Proposed distance-based methods using distribution distance for irrigation treatment classification.

6. Evaluated effects of spatial resolution, spectral configuration, band-to-band registration and image formats on classification accuracy.

7. Examined how view angles affect NDVI using a real-world flight mission.

8. Proposed regression models using stepwise and principal component analysis (PCA) for SWP prediction.

1.5 Dissertation Outline

The dissertation is organized as follows. Motivations and contributions are listed in Chapter 1. Chapter 2 examines the workflow of remote sensing using UAVs. Chapter 3 discusses almond tree canopy segmentation using both manual features and deep learning based instance-segmentation. In Chapter 4, different dimensionality reduction methods are proposed and irrigation treatment classifiers are designed and compared. Chapter 5 evaluates how image spatial resolution, spectral configuration, image band-to-band registration and image formats affect the accuracy of irrigation treatment classification and almond tree variety classification. Chapter 6 researches how view angles change the observed NDVI. Then SWP prediction models are built and compared between combinations of different dimensionality reduction methods and regression regularization methods. Finally, the dissertation is concluded in Chapter 7 and challenges and future work are presented.

Chapter 2

PRELIMINARIES

2.1 Basics of Remote Sensing

Remote sensing is the science of acquiring and interpreting information about objects without being in physical contact [122]. It includes sensing and recording reflected or emitted energy, processing and analyzing that information.

The energy sensed is in the form of electromagnetic radiation. There are two important characteristics to describe electromagnetic radiation, wavelength and frequency. The electromagnetic spectrum is the range of frequencies and wavelengths of electromagnetic radiations. There are several regions useful for remote sensing. The region we see the objects is a part of visible spectrum. The visible wavelength ranges from around 0.4 to 0.7 μm. Another portion of the spectrum is the infrared region, from 0.7 μm to 100 μm. The infrared region can be divided into NIR, short-wave infrared (SWIR) and thermal infrared (TIR), covering wavelengths from 0.7 μm to 1.4 μm, from 1.4 μm to 3.0 μm, and from 3 μm to 100 μm.

Although a primary electromagnetic energy source is the sun, all the objects can emit electromagnetic energy when their absolute temperature is above zero. The peak of thermal emission on the earth's surface is around 10 μm. Therefore, thermal detectors are usually designed to be sensitive to the radiation with the wavelength from 7 μm to 14 μm [122].

When radiation reaches and interacts with objects, three forms of interaction take place, absorption, transmission and reflection. The energy involved in each form depends on the wavelength and the material. In remote sensing, the radiation reflected by the objects or emitted from the objects is measured.

The ratio of reflected energy to incident energy is defined as reflectance. This wavelength-dependent reflectance, denoted as spectral reflectance, plays a key role in discriminating features of different materials. For example, green leaves have a high reflectance in the NIR range, whereas clear water absorbs the energy of wavelengths longer than the visible range, resulting a low reflectance in the NIR range. Additionally, reflectance is directional and it depends on both incident and view angles [123]. Bidirectional reflectance distribution function (BRDF) is used to quantify the geometric reflectance distribution with regard to incoming and outgoing directions.

When the energy is recorded in an image, three resolutions help describe the image measurement: spatial resolution, spectral resolution and temporal resolution. Spectral resolution describes the ground dimension of an image pixel. Spectral resolution describes the ability to differentiate different bands of measured wavelengths. Temporal resolution is defined as the time interval between successive remote sensing measurements [124].

2.2 Remote Sensing Using UAVs

UAV-based remote sensing system consists of unmanned aerial vehicles equipped with an autopilot, imaging sensors, ground control stations and communication systems. With the help of the onboard autopilot, human intervention during flight missions is minimized. However, special care needs to be taken for UAV-based remote sensing to obtain accurate and meaningful information. To summarize these required operations in UAV-based remote sensing, a workflow diagram is constructed in Fig. 2.1. Different from the workflow proposed for environment management in [125], radiometric correction and region of extraction are added, which are especially important for crop monitoring across days or growing stages. In the following sections, we will discuss these steps in more detail.

2.2.1 Image Collection

The first thing in image collection is to select a UAV platform. The most popular drone platforms are multi-rotors. They can take off and land vertically. They can hover in one spot and allow very precise position control for framing. It is easy and cheap to get an aerial view with multi-rotors. The downside of multi-rotors is their limited flight time. They need a lot of energy to fight against gravity and stay in the air. Fixed-wing drones have wings, they can fly like normal airplanes. They are very energy efficient and can fly for a very long time, covering a large area. The downside is that fixed-wing drones can not hover in one spot. It is also very hard to launch and land because they require a runway and a skillful pilot. Therefore, multi-rotors are ideal platforms for remote sensing studies in small agriculture research test sites, whereas fixed-wings are better for large and long distance areas.

Cameras are the core component for image collection. Aerial cameras should be small and light, so that they can be carried on a given UAV platform. In addition, light weight and low power consumption allow a longer flight time and a larger mapping area.

Spectral specifications of cameras are particularly important for remote sensing. There are multispectral cameras providing a few broad spectral bands (less then 10), hyperspectral cameras with a large number of narrow spectral bands (more then 100). To make these cameras lightweight, special design is required to balance their spectral resolution and performance. Spectral resolution is characterised by the

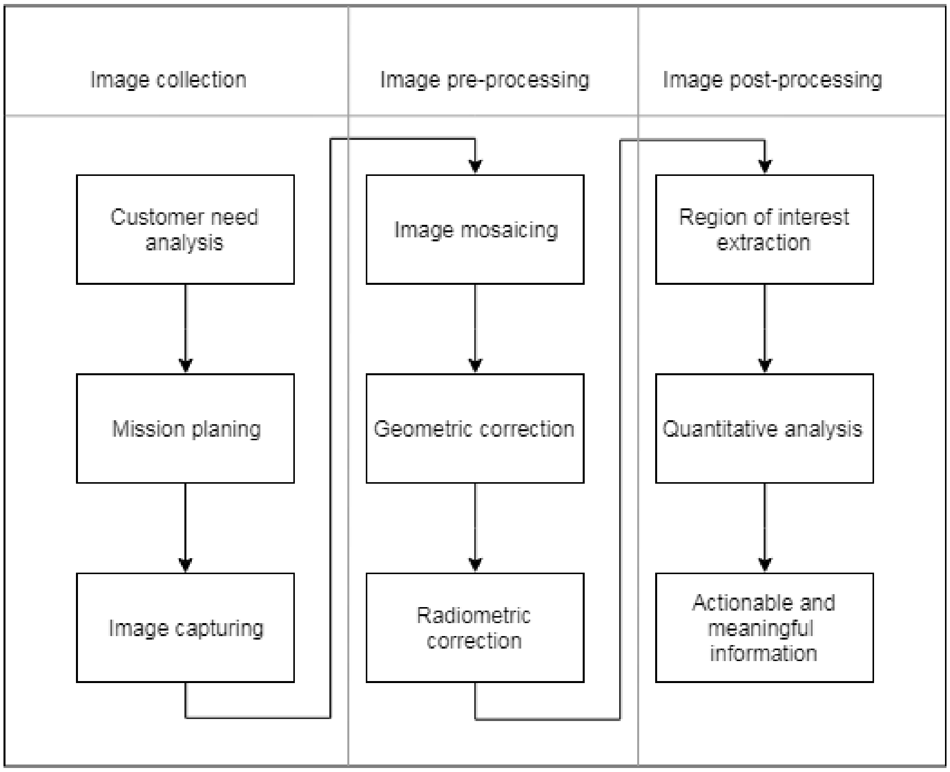

Figure 2.1: The workflow of UAV-based remote sensing

number of the spectral bands, band locations and band width. For agriculture applications, camera spectral range of interest includes red-green-blue (RGB), NIR, SWIR, and TIR bands [126].

Sensor size, along with focal length and flight altitude, determines the ground sample distance (GSD) of a mapping configuration, as described in equation (2.1), where H is flight altitude above the ground, pz is pixel pitch, the size of each pixel in the sensor,and f is focal length. According to equation (2.1), lower altitude, smaller pixel pitch and longer focal length result to a smaller GSD. For the same target, smaller GSD indicates that there are more image pixels recorded. In other words, this target is described with a higher spatial resolution. On the contrary, for a given camera, a larger GSD provides a larger field of view and, therefore, reduces flight passes over an area to be mapped.

$$GSD = \frac{H \times pz}{f}. \tag{2.1}$$

Mission planning entails a lot of considerations. It is important to design the flight paths. Flight paths need to ensure a decent amount of both forward and side overlap so these aerial images can be stitched together. Large overlaps are also required to overcome the flight drift caused by wind or GPS error [127]. There are two ways to increase the overlap while designing flight missions, increasing flight altitude and reducing flight speed. When the distance between two captures is kept, increasing flight altitude will increase the coverage of each capture, and hence increases the overlap between images. As required by the cameras, especially those cameras recording raw images, the time interval between two captures has to be longer than certain seconds. As a result, drones have to fly slowly enough between two images to achieve the target overlap. However, higher flight altitude means lower spatial resolution and lower flight speed causes a smaller mapping area under a given flight endurance. Therefore, flight altitude and flight speed have to be tuned to balance between image resolution, flight time and image overlap during the path design [128].

Last but not the least, aerial photography requires different camera setting from that of ground photography. To get rid of motion blur due to both flight and vibration, shutter speed needs to be as high as possible. Figure 2.2 shows that lower shutter speed causes motion blur in the capture. With higher shutter speed, larger aperture and high ISO are needed, so that the sensor can capture enough light energy. Figure 2.3 shows that small apertures result in dark images. On the other hand, high ISO leads to low signal-to-noise ratio and large apertures decrease the depth of view.

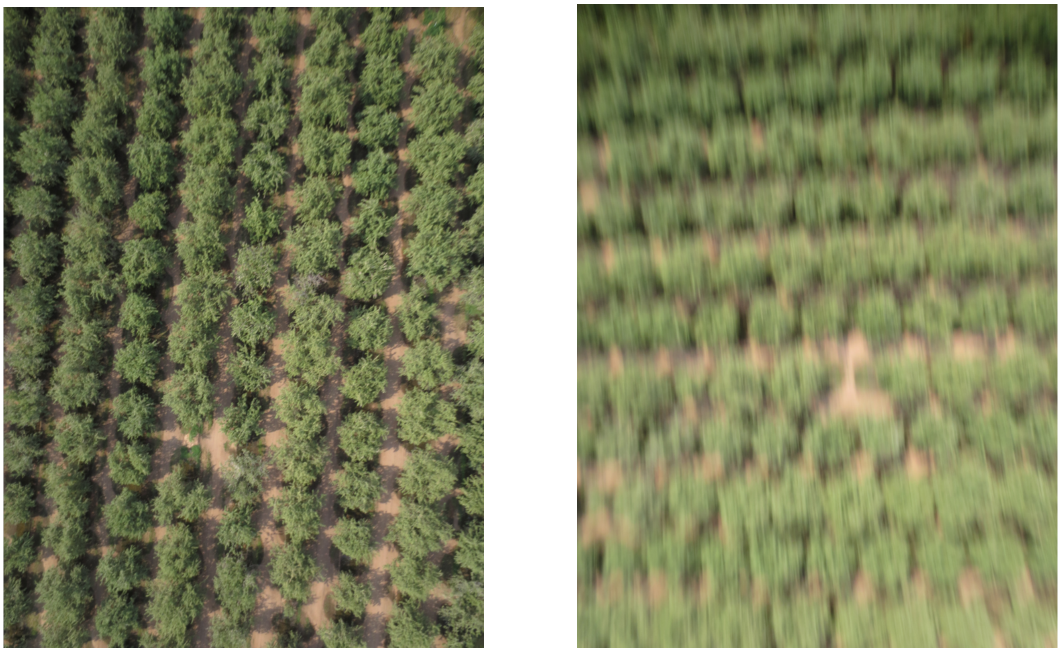

(a) Camera setting of ISO 100, f-stop f/2.7, shutter speed 1/1600

(b) Camera setting of ISO 100, f-stop f/2.7, shutter speed 1/1000

Figure 2.2: Compare images under different shutter speed

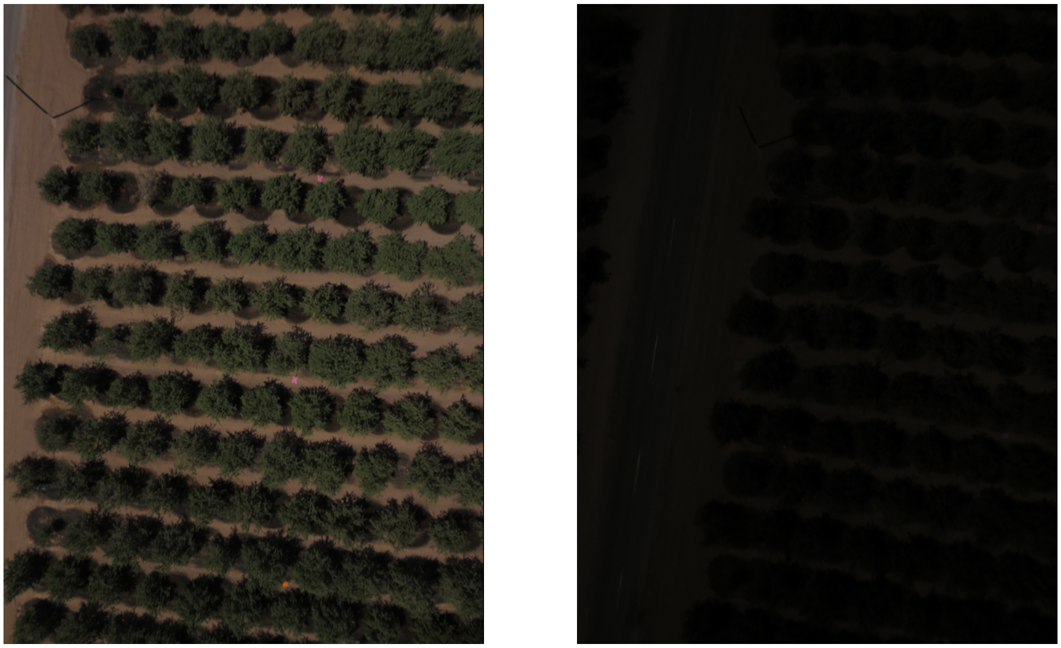

(a) Camera setting of ISO 100, f-stop f/2.7, shutter speed 1/2000

(b) Camera setting of ISO 100, f-stop f/8.0, shutter speed 1/2000

Figure 2.3: Compare images under different apertures

2.2.2 Image Pre-processing

Image mosaicing is the process to stitch images together to obtain an entire view of a scene. Typically, the onboard camera has a limited field of view. It can only capture images of a small area when it is stationary. When being fixed onboard the moving UAVs, cameras are triggered according to the programmed overlap setting. The individual images, each covering a slice of an area, are then mosaicked. This process increases the field of view and does not sacrifice the spatial resolution of the cameras [125].

All aerial images contain some degree of geometric distortion. These geometric distortion might come from both cameras and targets [129]. Camera optical distortion, aspect ratio and camera position variations introduce scale variations. Viewing geometry also causes scale variations, because the distance between the target and the camera increases when the target is away from nadir view angle. Distortion may be introduced by targets surface characteristics. For instance, targets of the same size appear bigger when they are captured with cameras at a lower altitude. Two approaches are used for correction of geometric distortion [130]. One is to model the sources of distortion when the distortions are well characterized. The other is to establish mathematical relationships between the position of pixels in an image and the corresponding coordinates of these pixels in a map. These pixels in the map are often referred to as ground control points (GCPs). Geometric correction is necessary for geo-scientific measurements, band-to-band registration and the detection of the changes between images of different time.

Usually there is noise or error in the remote sensed images caused by the sensors and the environment [131]. Within the sensors, these radiometric distortions may come from either pixel-to-pixel sensitivity variations or vignetting effect. Environmental factors such as solar angles, topography and atmospheric effects also cause radiometric disturbances. Furthermore, when remote sensing data are compared between different time, sensors, or sensor settings such as ISO, exposure and apertures, radiometric calibration is especially important [132]. Flat field correction can help remove the effects of pixel-to-pixel variations and vignetting [133]. Ground reference targets with known reflectance can be used for correction of atmospheric effects [131], changes of environment conditions and sensor settings.

2.2.3 Image Post-processing

With the development of sensing technologies, remote sensing images are acquired with higher spatial resolution and temporal resolution, posing an increasingly large challenge to process all the parts of these images. Region of interest extraction, an operation that differentiates interesting areas from uninteresting areas in the images, has been recognized as an important part of remote sensing image process to solve this problem [134–136]. The process of extracting region of interest is called segmentation. Many methods have been introduced on segmentation based on global threshold, edge detection and contour filling, region growing and region splitting etc [137]. Most recently, deep learning based methods are used for segmentation in remote sensing images [138, 139].

In the stage of quantitative analysis, features are extracted within the region of interest in the images and high-level models are built for specific applications. Most importantly, these models are validated with ground-truth field measurements. Physiological measurement predictions regarding the target crops are then obtained with these ground-truth calibrated models. These predictions are further combined with agronomists' knowledge to become actionable information for farmers.

Take irrigation monitoring of an almond orchard as an example. Given an orthomosaic image of the orchard after geometric and radiometric calibration, an individual almond tree canopy is segmented from background first. Then a regression model is built to predict water stress measurements according to canopy pixel digital number (DN) values. These predictions are further combined with agronomists' recommendation to become more specific actionable information. Therefore, a question like how much water is needed for the target orchard can be answered.

2.3 Chapter Summary

In the previous sections, we discussed image pre-processing and image post-processing in the operation workflow of UAV-based remote sensing. However, if we consider UAV-based remote sensing as a system taking payload configurations, camera settings and mission plans as input, generating crop feature information in the desired spatial resolution, image collection and image processing can be examined together by means of dimensionality reduction. Taking images with less bands and lower resolution can also be considered as a way of dimensionality reduction operationally. In other words, rather than focusing on dimensionality reduction on the collected images, it is necessary to reduce dimensionality in a systematic way and try to collect images with less bands and lower resolution from the first step, the beginning of UAV-based remote sensing. This systematic view also indicates that if better dimensionality reduction methods can be applied in the second step, it may relax certain restrictive requirements of image collection. Therefore, it is possible to reduce operation time by canceling flight missions using cameras with different band configuration, or flying the cameras at a higher altitude.

In the following chapters, we will examine how band selection and imaging spatial resolution configuration as dimensionality reduction methods affect the modeling performance in UAV-based remote sensing. Furthermore, we are interested in whether it is possible to obtain comparable performance by exploring new dimensionality reduction methods in both image pre-processing and post-processing stages.

Chapter 3

ALMOND TREE CANOPY SEGMENTATION IN AERIAL IMAGES

3.1 Introduction

When individual aerial images of almond are stitched and converted to an orthomosaic, almond tree canopy segmentation is necessary to extract water stress information in the single-tree level. More specifically, instead of semantic segmentation, the process of labeling each pixel within a class, instance-based segmentation [140] is required for water stress monitoring in the single-tree level. Instance-based segmentation differentiates pixels not only between classes, but also between objects of the same class.

It has been found that [110] soil brightness affects vegetation indices. For example, darker soil background results in a higher vegetation index value of NDVI. Therefore, it is necessary to get rid of soil pixels and hence minimize the influence before any further quantitative analysis. Moreover, classifying pixels in a single-tree instance level makes it possible to make quantitative analysis in the single-tree level, instead of the level of a single pixel or a block composed of multiple trees. A better understanding about the tree stress could be achieved by leveraging the relationship between these single pixels, as demonstrated by studies [76]. Aside from water stress monitoring, as a general crop feature, crop size can serve other applications such as evapotranspiration (ET) estimation [141], pesticide usage estimation [142] and yield estimation [143].

Studies were conducted on citrus tree counting based on QuickBird satellite images [144], where plant region was classified using K-means. Morphological skeleton algorithm was used to extract tree rows. Within tree rows, individual trees were separated and initial tree positions were generated after morphological erosion. In the end, tree positions and shapes were optimized by genetic algorithm. In [145], an approach for olive tree extraction was proposed. Nonlinear diffusion algorithms were used first to remove noise, smooth regions and prevent blurring edges. The second step was to delineate olive blobs using blob detection. In [146], the images were converted to binary images using a threshold. Then region growing was used to generate candidate olive tree region. Finally, these candidate areas were filtered according to shape and size parameters. Lidar was applied to delineate apple trees [147], where

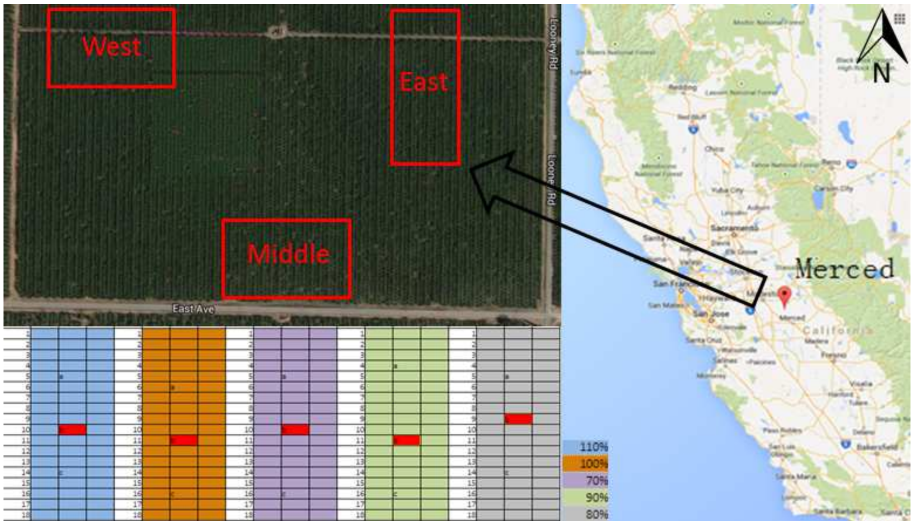

Figure 3.1: Overview of the test field, including three test blocks in the orchard, each composed of five plots treated with 70%, 80%,90%,100%,110% of crop evapotranspiration.

local maxima points were classified as tops of crowns, and local minima points were considered as boundary between trees. Lidar was also applied for forest tree segmentation [148]. Similar to [147], local maxima points were extracted as seed points. Seed growing methods were used to label the neighbor pixels. In [149], tree and nursery segmentation was studied using airborne images. Green index (2*Green-Blue-Red) was used to classify nursery from background. Morphological operations were further applied to filter small falsely identified regions. As for Christmas tree counting, color images were converted to gray images using index (Green-Rlue). Then local maximum pixels in the sliding window of size 25 pixels by 25 pixels were marked as tree locations. A minimum distance filter was further used to remove the neighboring pixels belonging to the same tree, whereas background pixels falsely identified as trees were filtered according to histogram difference between trees and background. Darius [150] developed tree identification and delineation algorithm for native Eucalypt trees using airborne images of spatial resolution approximately 1 meter/pixel. It involved three steps, local maxima detection, local minima detection and top-down clustering.

3.2 Materials and Methods

3.2.1 Test Field

This work was conducted in a mature, commercial almond (Prunus dulcis) orchard in Looney, Merced County, California (37.493498°N, -120.634914°W). There are three varieties of almond trees, Nonpareil, Carmel, and Monterey, planted on

Lovell peach rootstock. These trees are 15 years old, spacing at 5.5m×6.1m. The soil is composed of Rocklin loam and Greenfield sand. The region has typical Mediterranean climate, characterized by rainy, cool winters and hot, dry summers. Its average annual lowest temperature ranges from 25 to 30 (°F). In the orchard, five water treatments were carried out in different plots, with the amount of irrigation water from 70% to 110% of crop evapotranspiration (ET_c), with increasement of 10%. These irrigation treatments started in 2013. Each treatment was replicated in three blocks: the middle block, the west block and the east block. Each plot is composed of three lines with 18 trees each. One line of 18 trees lies between two adjacent plots (Fig. 3.1). Crop evapotranspiration was obtained according to Food and Agriculture Organization (FAO) method [151],

$$ET_c = K_c * ET_o, \tag{3.1}$$

where ET_o is the evapotranspiration rate of a reference surface under optimum treatment and certain climatic conditions, and K_c crop coefficient is defined as the ratio ET_c/ET_o.

3.2.2 Data Collection

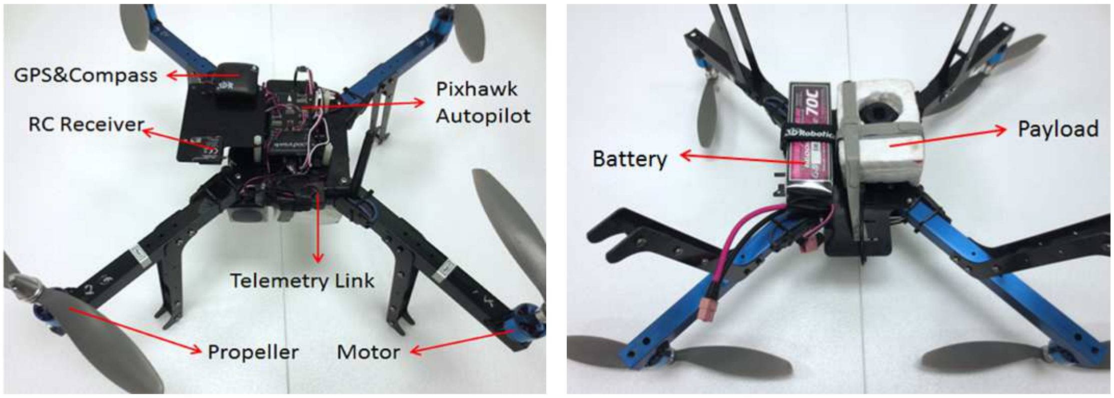

(a) Top view (b) Bottom view

Figure 3.2: The quadcopter platform used for data collection

The UAV used in this study was built using DIY Quadkit (3DRobotics, Berkeley, USA), modified to carry a single camera payload to do the remote sensing. Its top view and bottom view of the quadcopter are shown in Fig. 3.2. The maximum takeoff weight of the aircraft is 2.0 Kg and its flight time is about 15 minutes. One modified commercial-off-the-shelve (COTS) NIR camera (ELPH110HS, Canon, Japan) was flown at an altitude 60 m above ground level (AGL) on May 20th, 2015. It includes three bands, NIR, green and blue, centered at 720 nm, 520

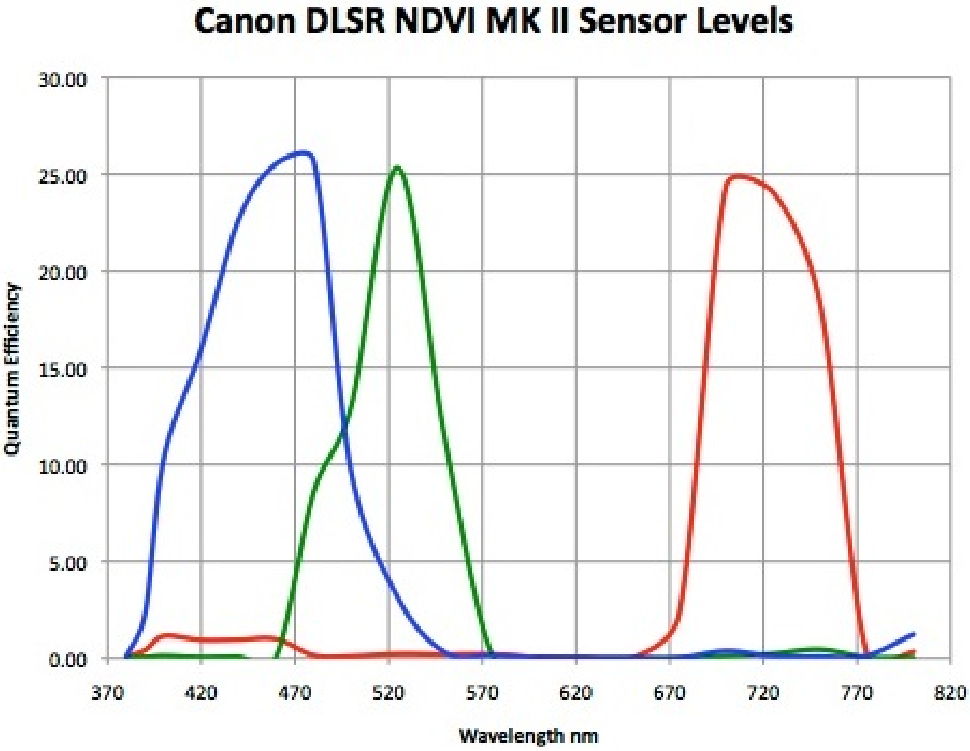

Figure 3.3: Spectrum configuration of the modified NIR camera [3].

nm, and 470 nm, as shown in Fig. 3.3. It has a resolution of 4608×3459, with 16 bit radiometric resolution. More specifications are listed in Tab. 3.1. The aerial images were then stitched using Photoscan (Agisoft, Russia) to generate an orthomosaic image. Canopy classification and segmentation were based on the orthomosaic image.

3.2.3 Otsu's Method

Otsu's method provides a powerful tool for threshold selection which facilitates image segmentation. It was devised as a way of easily evaluating the effectiveness of a threshold to produce an automated means of threshold selection [152]. This variant of clustering creates tight clusters to prevent overlap. It is done by altering thresholds, increasing the spread of one threshold while resulting in the decrease in another threshold. As a rule, one needs to choose the threshold that will minimize the combined spread. Through computational analysis Otsu is able to come up with the between-class variance $\sigma_\omega^2(t)$ which can be simplified to:

Table 3.1: Specifications of the modified NIR camera

Camera	ELPH110HS
Image width (horizontal, pixels)	4608
Image height (vertical, pixels)	3456
Focal length (mm)	4.3
CCD-width (mm)	6.16
CCD-height (mm)	4.62

$$\sigma_\omega^2(t) = \omega_0(t)\sigma_0^2(t) + \omega_1(t)\sigma_1^2(t), \tag{3.2}$$

$$\omega_0(t) = \sum_{i=0}^{t-1} p(i), \tag{3.3}$$

$$\omega_1(t) = \sum_{i=t}^{L-1} p(i), \tag{3.4}$$

$$\mu_0(t) = \sum_{i=0}^{t-1} \frac{ip(i)}{\omega_0(t)}, \tag{3.5}$$

$$\mu_1(t) = \sum_{i=t}^{L-1} \frac{ip(i)}{\omega_1(t)}, \tag{3.6}$$

$$\sigma_0^2(t) = \sum_{i=0}^{t-1} (i - \mu_0(t))^2 \frac{p(i)}{\omega_0(t)}, \tag{3.7}$$

$$\sigma_1^2(t) = \sum_{i=t}^{L-1} (i - \mu_1(t))^2 \frac{p(i)}{\omega_1(t)}, \tag{3.8}$$

where $\omega_0(t)$ and $\omega_0(t)$ are the probabilities of pixels assigned to two classes according to a threshold t, $\mu_0(t)$ and $\mu_1(t)$ are pixel digital value means of two classes, and $\sigma_0^2(t)$ and $\sigma_1^2(t)$ are class variances.

3.2.4 HSV Color Space

Hue, saturation, and value (HSV) is a three dimensional color space which is used primarily in the generation of computer graphics. In the HSV space, hue describes the color in an image in the form such as an angle, typically in the range of 0° to 360°. Saturation denotes the span of grey in the HSV color space, usually in a range of 0% to 100%, where 0% represents the color grey, 100% a primary color, and anything in between is a mixture of the two. Value is the brightness of a color which is dependent on the amount of saturation present. It is usually within the scale of 0% to 100% in which 0% corresponds to a hue that is completely black while one with 100% gives a very bright hue. By converting images from the RGB plane into the HSV, an object's specific hue, saturation, and value or intensity in a given image can be exploited to isolate the selected image via color segmentation and a threshold mask based on hue, saturation, or intensity [153].

3.2.5 Gray Level Concurrence Matrix

The unique texture of an image in question makes it distinguishable from the textures of other objects or even from the background when combined with the k-nearest neighbors (KNN) algorithm [154]. The two-step process first requires the use of the gray level concurrence matrix (GLCM) method which extracts textural features from a given image and stores them in matrix that has the same number of rows and columns that a given image has gray levels [155]. The GLCM shows how often two pixels p_i and p_j representing pixel intensity i and j respectively occur at a given pixel distance $(\Delta x, \Delta y)$ within a neighborhood denoted by the GLCM element $p(i, j|\Delta x, \Delta y)$. Additionally, the GLCM element $p(i, j|d, \theta)$ accounts for changes in the gray levels of i and j at a distance d positioned at an angle θ. Haralick et al. [156] developed a set of features for classifying pictorial data. Specifically, they provided a general technique for the extraction of textural properties from gray-tone special-dependency matrices. Haralick, et al. [156] created 14 measures for the extraction of textural features. However, Newsam and Kamath [157] showed that only about five are frequently used. These five include angular second moment (ASM), contrast (CON), inverse different moment (IDM), entropy (ENT), and correlation (COR). Denote the quantization levels of images as L. These five features are described as

$$ASM = \sum_{i=1}^{L}\sum_{j=1}^{L} p(i,j), \tag{3.9}$$

$$CON = \sum_{i=1}^{L}\sum_{j=1}^{L} |i-j|^2 p(i,j), \tag{3.10}$$

$$IDM = \sum_{i=1}^{L}\sum_{j=1}^{L} \frac{p(i,j)}{1+|i-j|^2}, \tag{3.11}$$

$$ENT = \sum_{i=1}^{L}\sum_{j=1}^{L} -ln(p(i,j))p(i,j), \tag{3.12}$$

$$COR = \sum_{i=1}^{L} \sum_{j=1}^{L} \frac{(ij)p(i,j) - \mu_i \mu_j}{\sigma_i \sigma_j}, \tag{3.13}$$

where

$$\mu_i = \sum_{i=1}^{L} \sum_{j=1}^{L} ip(i,j), \tag{3.14}$$

$$\mu_j = \sum_{i=1}^{L} \sum_{j=1}^{L} jp(i,j), \tag{3.15}$$

$$\sigma_i^2 = \sum_{i=1}^{L} \sum_{j=1}^{L} p(i,j)(i - \mu_i)^2, \tag{3.16}$$

$$\sigma_j^2 = \sum_{i=1}^{L} \sum_{j=1}^{L} p(i,j)(j - \mu_j)^2. \tag{3.17}$$

3.2.6 K-Nearest Neighbors

K-nearest neighbors (KNN) classification is one of the most popular machine learning methods [158]. It classifies an unknown sample according to its neighbors. Usually to increase the accuracy, more than one neighbors are used. Given a test sample and a training set with known labels, the distances between the test sample and all the samples in the training set are calculated. Then the test sample is assigned with the most frequent label of its k nearest neighbors.

The distance used in KNN is commonly based on the Euclidean distance [159]. Denoting $\mathbf{x}_i$ as an test sample with p features $\mathbf{x}_i = (x_{i1}, x_{i2}, ..., x_{ip})$, n as the total number of training samples, the Euclidean distance between $\mathbf{x}_i$ and $\mathbf{x}_t$ $(t = 1, 2, ..., n)$ is defined as

$$d(\mathbf{x}_i, \mathbf{x}_t) = \sqrt{(x_{i1} - x_{t1})^2 + ((x_{i2} - x_{t2})^2 + \cdots + (x_{ip} - x_{tp})^2}. \tag{3.18}$$

3.2.7 Instance Segmentation Using Deep Learning

Deep learning [160] methods, composed of multiple levels of non-linear modules, extract representations automatically from the raw data. It has achieved surprisingly good results in object detection [161] and image segmentation [162]. As a general framework, it can solve the problem in an end-to-end way and save the effort to design manual features and classifiers based on these features. Published studies on aerial image processing using deep learning showed that deep learning methods are robust to lighting conditions, camera settings, and background changes [163].

Different from semantic segmentation, where different objects of the same class are classified as the same, instance segmentation classifies different objects of the same class as different instances. Considering the application of water stress detection at an individual tree level, instance-aware segmentation can detect and locate pixels of each individual tree. Many deep learning methods have been proposed for instance segmentation [164–167]. As a case study, the method in [165] is evaluated for tree canopy instance segmentation.

The basic idea of instance segmentation [165] is to separate two connected instances by detecting segment instances. Then these segment instances are assembled into instances according to the their relative positions in an instance. It is converted from fully convolutional neural network segmentation [162] by adding two fully convolutional networks. One is used for segment instance detection and the other is estimating instance objectness score. Then an assembling module generates the instance by combining the segment instance map and instance objectness map.

3.3 Canopy Segmentation Using Manual Features

The test image for this paper was taken on May 20th, 2015. In this section two types of classification methods to differentiate trees from non-tree parts are presented. One is an unsupervised Otsu threshold method. The other is a supervised method based on histogram similarity in HSV color space and text features described by GLCM. 20 samples are prepared as model samples for supervised classifications, including 10 tree samples, 2 shade samples (the soil surface part shaded by trees), 3 soil samples and 5 grass samples. All these samples are of size 10×10. It is clear that grass and trees have almost the same color, so the grass samples account for 50 percent of non-tree samples. All the 20 samples are displayed in Fig. 3.4. In addition to 20 model samples, there are another 100 samples selected to test the classification performance, composed of 50 tree samples and 50 non-tree samples.

3.3.1 Canopy Classification

3.3.1.1 Otsu's Method

According to the fact that the difference of crops between the NIR band and the visible band is larger than that of soil, the original image is converted to a gray image by taking the difference between the NIR band and the blue band. The threshold is calculated based on the large image in Fig. 3.5(a) using the Otsu's method. For each test sample, if the number of pixels, whose intensity is larger than the threshold, is greater than 50, then this sample is classified as a tree sample. Otherwise, it is marked as a non-tree sample. According to the results in Tab. 3.2, all the tree samples are predicted as trees. The problem is that, however, more than 40 non-tree samples are recognized as trees, which will cause a big trouble to measure the size of tree canopies.

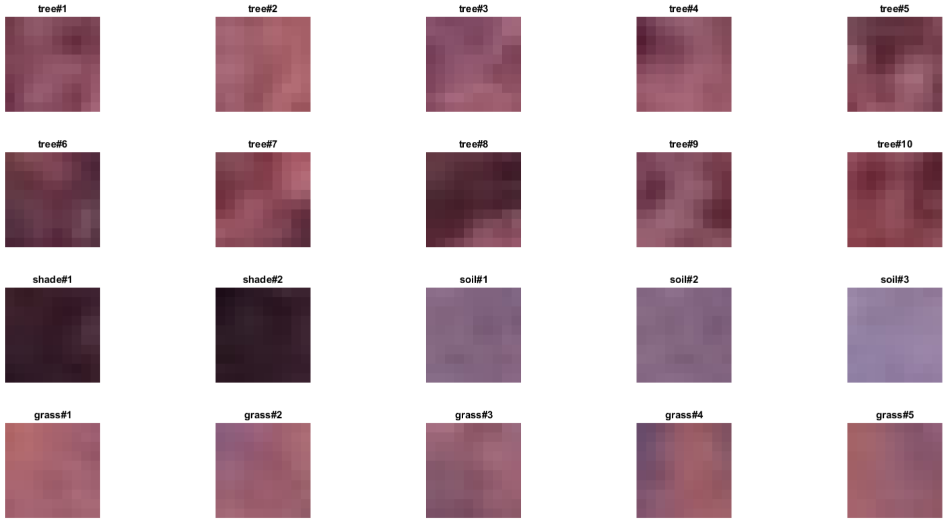

Figure 3.4: Model samples, including 10 tree samples, 2 shade samples, 3 soil samples and 5 grass samples

Table 3.2: Classification performance of Otsu's method

Otsu (gray image)	Tree (Predicted)	Non-tree (Predicted)
Tree (Real)	50	0
Non-tree (Real)	40	10

3.3.1.2 HSV Histogram

The RGB color space is nonlinear and it is better to convert the image from RGB to more uniform color space HSV. First, all the samples are converted to the HSV color space. Then, histograms of all the samples in H, S, V are calculated individually. The histograms are divided into 32 bins and each bin cuts 3.125 (1/32) percent of the range of H, S, V intensity. The empty bins are set to one to make the definition of distance between histogram distributions applicable according to Kullback's minimum cross-entropy principle, as described in Equ. 3.19, where $sandm$ stand for two histograms with n bins, s_i, m_i represent the fractions of each bin i. The distance in H, S, V is added together as the overall distance between training samples and test samples. Finally, KNN is applied to predict the label of the sample, where k is set as 5 in the test.

$$d(s,m) = \sum_{i=1}^{n} s_i ln \frac{s_i}{m_i}. \tag{3.19}$$

Table 3.3 shows that HSV method helps filter non-tree pixels, where only 10 non-tree samples are labeled as trees, although it increases the possibility to classify tree pixels as non-tree pixels at the same time. Further checking indicates that all the non-tree samples recognized as tree samples are grass samples, which means grass and trees have similar color even in HSV space.

Table 3.3: Classification performance of HSV method

HSV	Tree (Predicted)	Non-tree (Predicted)
Tree (True)	45	5
Non-tree (True)	10	40

3.3.1.3 Combining GLCM and HSV Histogram

In order to get better classification accuracy, texture and color are combined to help differentiate grass from trees. As an important texture feature, GLCMes has been widely used in many applications. The GLCMes is calculated in 8 directions, 0, 45, 90, 135, 180, 225, 315, at 16 gray levels in NIR, red and blue bands. Contrast, correlation, energy and homogeneity are obtained based on the matrixes and then are averaged in 8 directions to become rotation invariant. For each sample, there are three GLCM feature vectors composed of contrast, correlation, energy and homogeneity in NIR, green and blue bands. The GLCM distance between samples is measured by sum of square of distance between their GLCM vectors in three bands. The HSV distance and GLCM distance are normalized individually before being added as a combined feature. Similarly, KNN is applied in the tests. As shown in Tab. 3.4, the combined method decreases the fault rate of classifying non-trees as trees, which is better than both HSV method and Otsu's method. At the same time, all the tree samples are recognized, which further indicates that the combined method is better than the HSV method, and as good as the Otsu's method.

3.3.2 Canopy Segmentation

As shown in Fig. 3.5, the original image is converted to binary images using three methods, the Otsu's method, the HSV method and the combined method. HSV method does help filter out some grass patches. However, the combined method recognizes many soil parts as canopies. Its performance is not as good as the one in test samples. Considering the requirement of labeled samples, and downsampling

Table 3.4: Classification performance of HSV combined with GLCM

HSV+GLCM	Tree (Predicted)	Non-tree (Predicted)
Tree (True)	50	0
Non-tree (True)	7	43

effect of texture methods, the Otsu's method is used as for canopy pixel classification. The Otsu's method is unsupervised, so it does not need training samples. As for the high fault rate of classifying grass as trees, morphological features can be used in the postprocessing part to filter these pixels.

3.3.2.1 Filtering Small Grass Regions

There are some isolated patches labeled as canopies in the image obtained directly from the Otsu's method (Fig. 3.6(a)). These patches are either small grass regions or soil regions, which can be deleted based on their size. Figure 3.6(b) shows the image obtained after white patches with area less than 500 pixels are deleted. In addition, there are some patches, shaded region in the canopies are labeled as non-tree. These patches can be corrected according to their sizes too. Figure 3.6(c) shows the image after the dark patches with area less than 500 pixels are re-labeled as tree canopies. Note that erosion and dilation are not appropriate here, since they will change the size of canopies in the images.

3.3.2.2 Filtering Large Grass Regions

Small isolated patches are easy to process according to their sizes. However, there are still some large grass patches left connected with tree canopies. More features are needed to cut these patches away from canopies according to certain features. First, they are narrower than canopies. Figure 3.7(a) filters all the patches less than 25 pixels wide. The problem is that two types of canopy regions are filtered too. One part is from the top or bottom of the canopy circle. The other part is from the region connecting two canopies. These two parts are characterized by their orientations, height and major axis length. Figure 3.7(b) shows the image with patches height less than 5 pixels. After patches with orientation angles (absolute value) less than 5 degree and major axis length less than 25 pixels are deleted, the obtained image is as Fig. 3.7(c), where all the large grass patches are left. After taking all these large grass patches away, the final result is shown in Fig. 3.7(d). There are two remaining troubles preventing counting trees and the pixels in each canopy. First, there are certain regions between the forth row and the fifth row connected. Second, there are many tree canopies connected in each row.

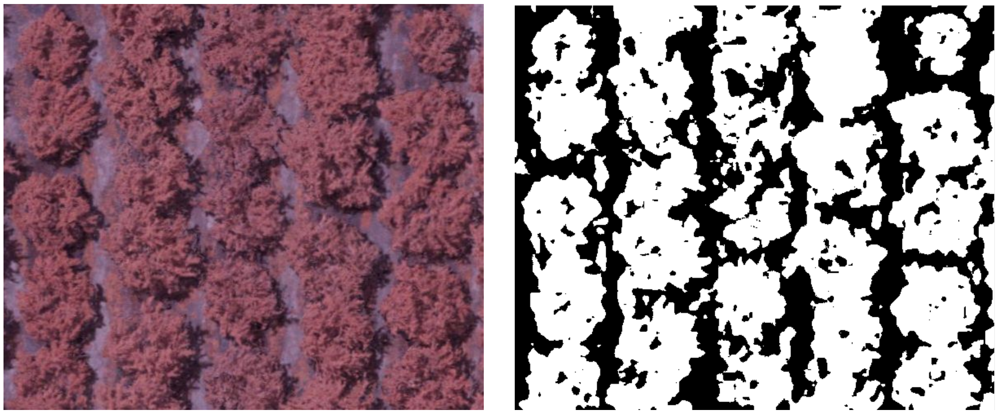

(a) Original image

(b) Binary image with the Otsu's method

(c) Binary image with the HSV method

(d) Binary image with the combined method of HSV and GLCM. Tree canopy is white and others are black

Figure 3.5: Comparing canopy classification using different features

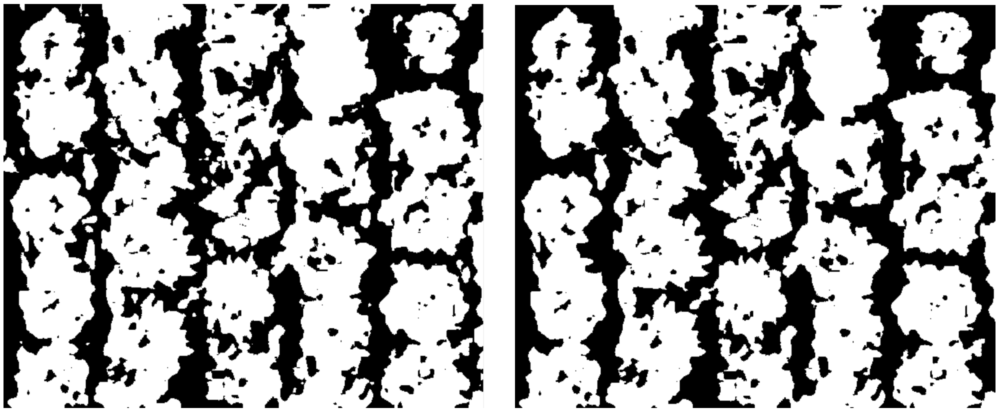

(a) The binary image obtained with the Otsu's method (b) The binary image after deleting small patches outside canopies

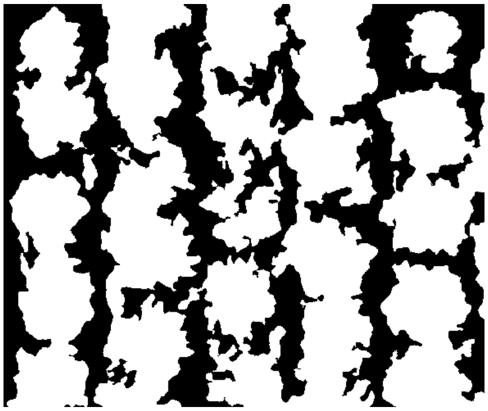

(c) The binary image after deleting small patches within canopies.

Figure 3.6: Filtering small grass regions and shaded regions.

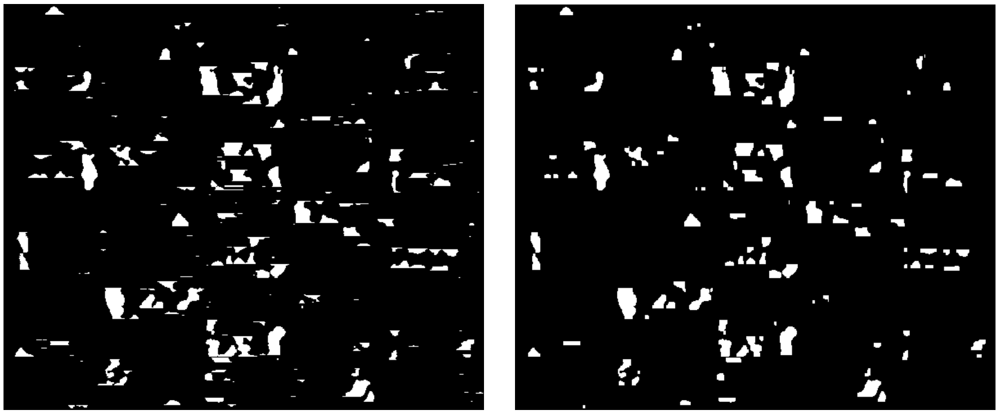

(a) Connected regions less than 25 pixels in the horizontal direction.

(b) After deleting regions less than 5 in the vertical direction.

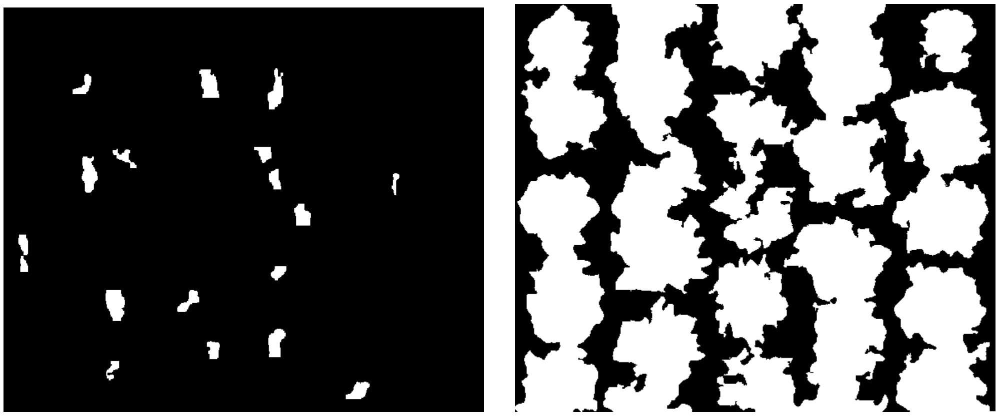

(c) After deleting regions with orientation angles (absolute value) less than 5 degree, major axes less than 25 pixels long.

(d) The cleaned result

Figure 3.7: Filtering large grass regions

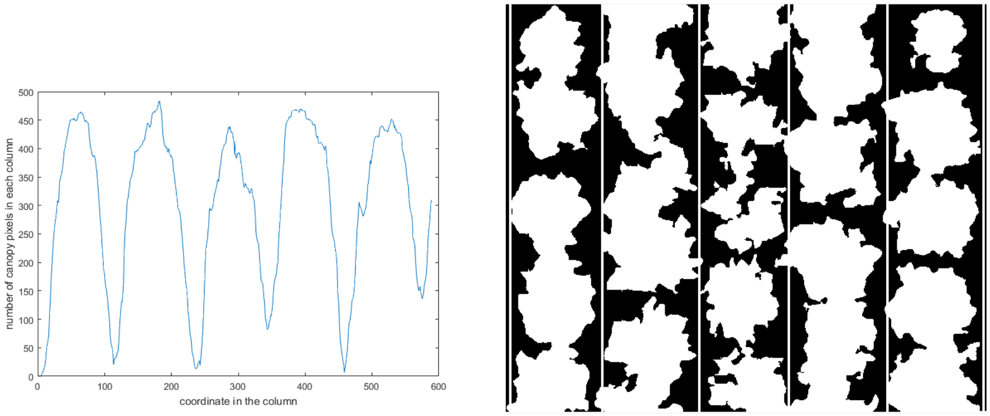

(a) Number of canopy pixels in each column (b) The binary image with lines separating each row of trees

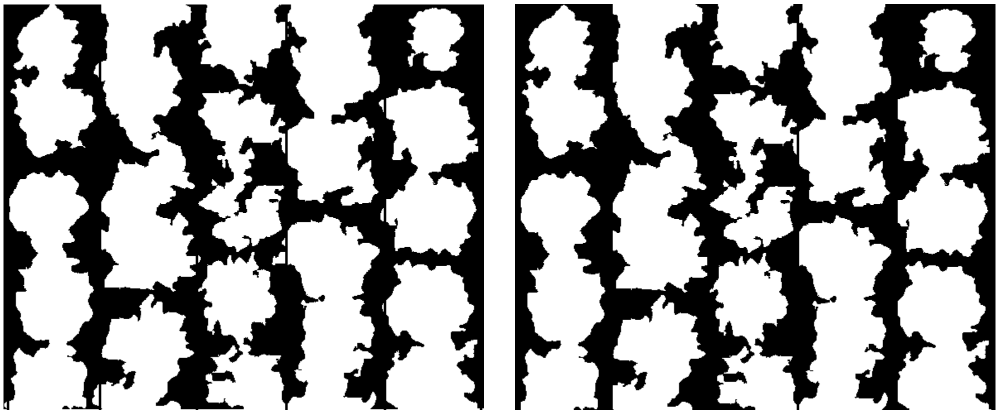

(c) Pixels on the lines marked as non-canopy (d) The binary image after deleting regions smaller than 100.

Figure 3.8: Separating every row.

3.3.2.3 Separating Every Row

To separate the connected rows, the border for each row needs to be detected. By calculating the number of pixels in each column, six local minimum points show up in Fig. 3.8(a). In Fig. 3.8(b), lines are put between rows right at the points with locally minimum number of canopy pixels. It turns out these lines are good estimations of borders to separate each row. After deleting the canopy pixels in the lines and small isolated patches generated, five separate rows are obtained in Fig. 3.8(d).

3.3.2.4 Separating Every Tree

After obtaining the border for each row, the remaining step is to separate each tree in a row. Similarly, segmentation of each tree can rely on the number

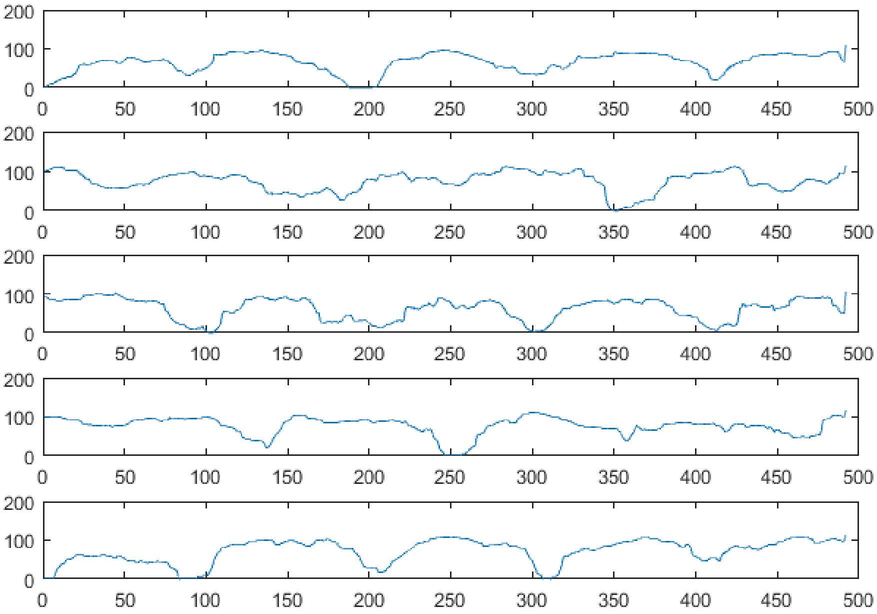

Figure 3.9: Number of canopy pixels in each line within a row of trees.

of canopy pixels in each line within a row. Figure 3.9 shows the number of pixels in each line in each row, where there is a local minimum every around 100 lines. After deleting the pixels in the lines where these local minimum are, all the trees are separated in Fig. 3.10(a). In both Fig. 3.10(a) and Fig. 3.10(b), centroid of each tree canopy is marked in blue.

3.4 Canopy Segmentation Using Instance-aware Segmentation Method

3.4.1 Experiment Setting

In the study, 162 NIR images of tree canopies are manually labelled. Each image covers around 6 trees, with the size 229×232. These images were collected in May, June, July, August, September, and October 2014. So they can represent tree canopies under all different growing stages. These images are further mirrored and flipped to generate a larger dataset. After image augmentation, there are 648 images in all, where 500 images are used as the training set, and 158 images are used as the validation set. The images are then organized in the same format as VOC2012 [168]. This experiment is based on the released code along with the paper [165], where the number of classes changes to 2 for only tree canopy segmentation, canopies and background. The thresholds are set to 0.5 for both canopies and background.

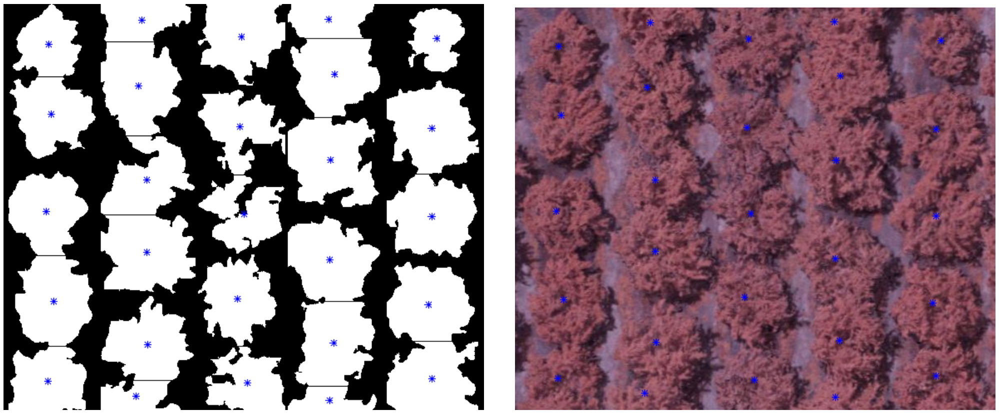

(a) Each tree is separated and its centroid is marked in the binary image.

(b) The centroid of each tree is marked in the original image.

Figure 3.10: The final results of tree canopy segmentation.

3.4.2 Results and Discussion

The instance-segmentation model is evaluated on the validation dataset in terms of precision and recall while the model is under training, as shown in Fig. 3.12. Precision and recall are defined as the following:

- True Positive(TP): A true canopy pixel is predicted as a canopy pixel.
- False Positive(FP): A true non-canopy pixel is predicted as a canopy pixel.
- False Negative(FN): A true canopy pixel is predicted as a non-canopy pixel.
- True Negative(TN): A true non-canopy pixel is predicted as a non-canopy pixel.
- Precision: The ability of a model to identify only the correct objects, defined as

$$Precision = \frac{TP}{TP + FP}. \tag{3.20}$$

- Recall: The ability of a model to detect all the correct objects, defined as

$$Recall = \frac{TP}{TP + FN}. \tag{3.21}$$

The results are better than that of canopy classification using textures and colors. For example, the recall could be as high as 97.1% when the precision is still above 90%. Considering these images were collected in different growing stages of almond trees and different time of the day, the good performance indicates that the trained model is robust to canopy size and lighting conditions. More detail about

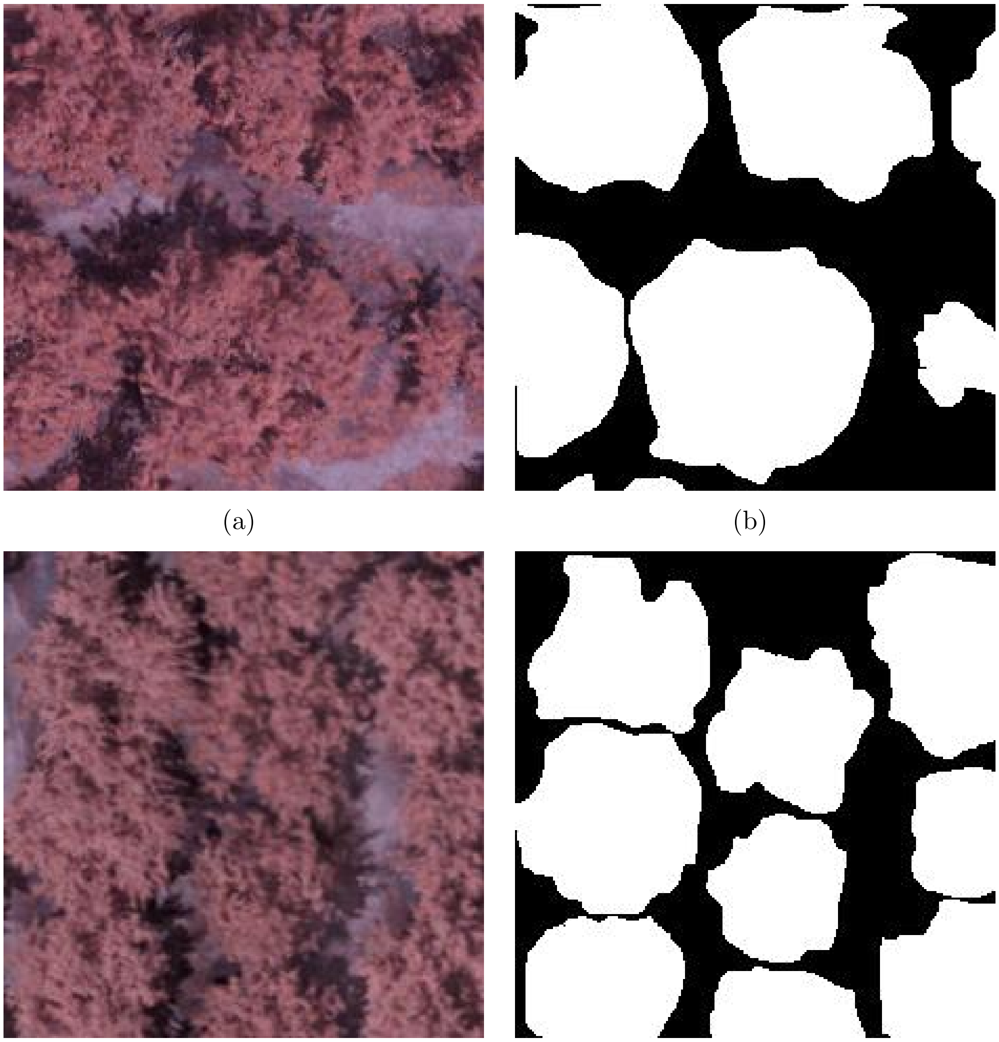

(a) (b)

(c) (d)

Figure 3.11: Canopy images (a), (c) and their masks (b), (d).

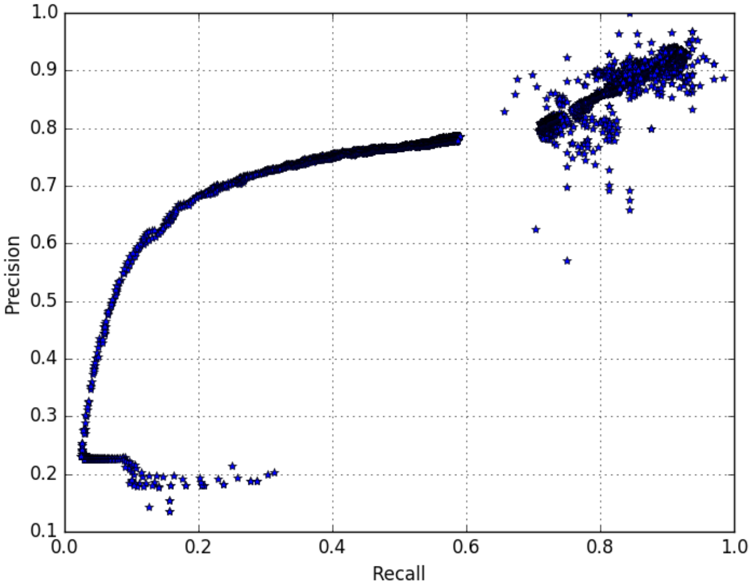

Figure 3.12: Precision and recall of canopy instance-segmentation in the validation dataset.

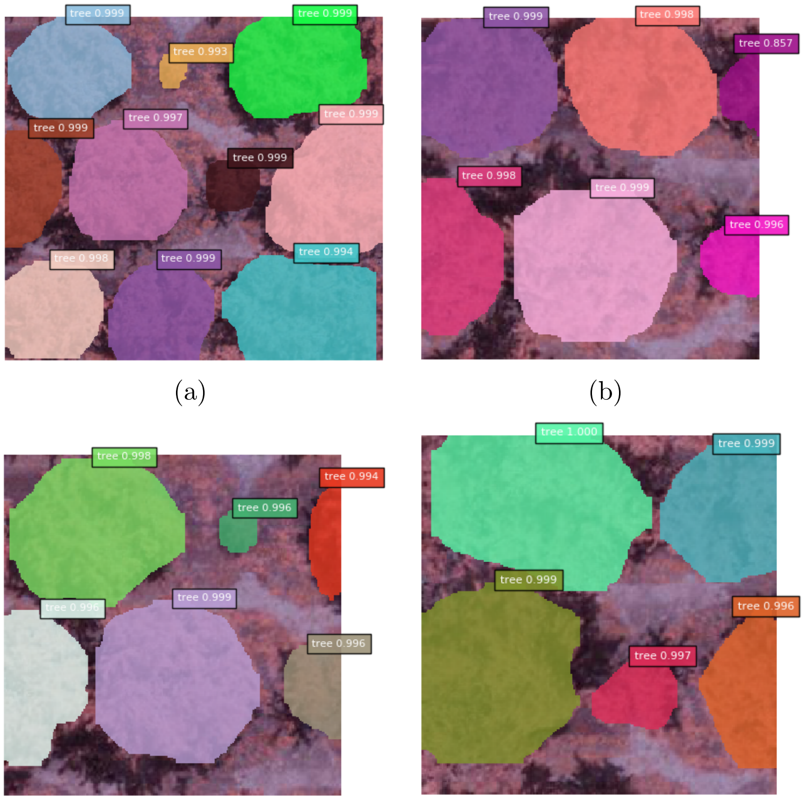

(a) (b)

(c) (d)

Figure 3.13: Canopy segmentation results in test images using instance-segmentation method.

the instance-segmentation performance is shown in Fig. 3.13. The grass pixels which are really similar to canopy pixels in color and texture are also classified correctly as background. It is able to detect canopies of both big and small size (the green canopy in Fig. 3.13(c)). The connected tree canopies (top right part in Fig.3.13(a), 3.13(b)) can be segmented well. Trees in Fig. 3.13(a) and 3.13(b) are not well aligned in horizontal or vertical rows, indicating that the model is robust to row orientation. However, segmentation using manual features assumes that trees are aligned in horizontal or vertical rows.

3.5 Chapter Summary

With such high resolution aerial images, it is possible to monitor and analyze the health of almond trees in the level of an individual tree. The first step for tree-level monitoring and analysis is to segment canopies for each individual tree.

Two different approaches are discussed in this chapter to segment almond tree canopies in high resolution aerial images. In the first approach, lots of effort were involved in designing manual features, where color and texture features are used to classify canopy pixels and morphological features are extracted to filter grass pixels and segment tree canopies. The second approach is based on modern deep learning convolutional neural networks. Instead of leveraging many manmade features and parameters, deep learning instance-segmentation is an end-to-end method. It learns all the related features automatically according to the prepared training images and masks. More importantly, it is shown that these self-learned features are robust to object size, object orientation, and lighting conditions.

The downside of deep learning instance-segmentation is time-consuming labeling and hyper-parameter tuning. Fortunately, there are many released models pre-trained on million of images. These models will save the requirement of dataset volume and the effort in hyper-parameter tuning as well. Moreover, with the extensive research activities on few-shot learning [169], one-shot learning [170], transfer learning [171], deep learning based segmentation will be more accurate while requiring less labeling effort and training process.

Chapter 4

IRRIGATION TREATMENT CLASSIFICATION OF ALMOND TREES

4.1 Introduction

With the help of UAV-based remote sensing, it becomes much easier to collect aerial images at a spatial resolution up to centimeters per pixel. The high spatial resolution makes it possible not only to differentiate individual trees, as described in Chapter 3, but also to analyze features at individual tree level.

Although many existing methods from satellite-based remote sensing can be used for analyzing UAV-based remote sensing images, these methods are initially designed for low-resolution images. They are mainly about various types of vegetation indices based on either broad band or narrow band spectral measurements for a single pixel. Because the spatial resolution of these images is from kilometers per pixel to meters per pixel, it is hard to conduct plant-level analysis. Considering the task to monitor almond trees, there are only a few pixels for a single tree even with the most recent satellite GeoEye-2, which can deliver multi-spectral images at 1.24 meter per pixel.

There have been many studies on plant-level water stress monitoring based on high resolution UAV images [172] or hand-held scanners. In [173], spectral data acquired via a fixed-wing airplane were used to detect physiological changes of citrus trees under both water stress and saline stress. Average spectral indicators of reflectance in the red band, reflectance in the NIR band, and NDVI showed significant differences among treatments. In [174], reflectance of sugar beet between 720 nm and 1100 nm showed difference of irrigation levels. Yet small variations in irrigation levels could not be distinguished with only spectral reflectance. In [175], the plant senescence reflectance index [176] and area under curve in the SWIR region were used to detect water stress of pear tress under deficit irrigation, yet the stress was detected 17 days after the implementation of the treatment.

However, all the above studies used vegetation indices based on average reflectance of the region of interest. Studies in [177, 178] showed that, the averages of vegetation indices such as NDVI, were similar even if they were calculated with different image resolutions, whether the images were acquired using satellites, UAVs, ground spectrometers or hand-held scanners.

Inspired by this phenomenon, a new methodology beyond average vegetation indices is proposed to fully explore the benefits of high spatial resolution enabled by UAVs. Instead of just averaging the pixel DN values or vegetation indices in different spatial scale, i.e., tree levels, row levels or plot levels, and in different bands such as red band, green band and blue band, each pixel in each band or each type of vegetation indices is considered as an individual observation for the tree the pixel belongs. Furthermore, each observation adds one dimension to the measurement of that tree. Therefore, high spatial resolution images provide a measurement with significant higher dimensions.

For example, considering an image covering a single tree with the size of w pixels in width and h pixels in height, the number of different bands b, the number of different vegetation indices v based on b bands, the measurement dimension for this tree is v in the traditional practice where only averages of vegetation indices are used, whereas the measurement dimension becomes $w * h * (b + v)$ according to the proposed methodology.

The remainder of this chapter addresses a classification problem, how to differentiate the integral effects of irrigation levels of 70%, 80%, 90%, 100%, 110% on almond trees using multispectral aerial images according to this proposed methodology. Section 4.2 describes data collection, preprocessing and basics of descriptive statistics, dimensionality reduction methods of principal components analysis (PCA), linear discriminant analysis (LDA), artificial neural network (ANN), and distribution distance. Section 4.3.1 compares classification performances using descriptive statistics. Histograms based treatment classification is presented in Section 4.3.2. Section 4.3.3 introduces treatment classification with distribution distance between canopy histograms. Finally, all these methods are compared in Section 4.4.

4.2 Materials and Methods

4.2.1 Data Collection

Two flight missions were conducted in the almond test field around noon on June 29 and June 30 in 2017. RGB (Survey 2, MAPIR, USA), NIR (Survey 2, MAPIR, USA), TIR (ICP9640P, ICI, USA) and SWIR (320P, ICI, USA) cameras were flown at the altitude of 60 m above ground level (AGL) on June 29, 2017 over the middle block and at the altitude of 120 m AGL on June 30, 2017 over the west, middle and east blocks. Specifications for these cameras are listed in Fig. 4.1, Tables. 4.2, 4.3 and 4.4. Image spatial resolutions of different cameras at 60 m and 120 m are listed in Tab. 4.1.

Raw images of RGB, NIR, TIR, SWIR cameras are collected during flights and then converted into tagged image file format (TIF) images in the lab. These TIF images are stitched into orthomosaic images using Photoscan (Agisoft, Russia). These orthomosaic images are georeferenced in ArcGIS (Esri, USA) with ground

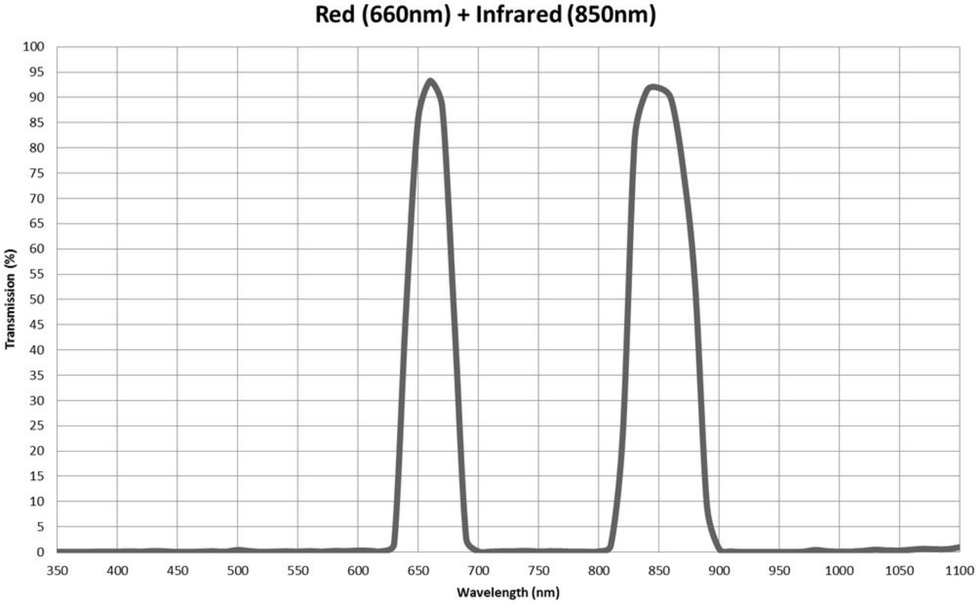

Figure 4.1: Spectrum configuration of the Survey II camera (NDVI NIR+RED) [4].

Table 4.1: Spatial resolutions of four cameras

Camera	Spatial Resolution (60 m)	Spatial Resolution (120 m)
RGB	2.03 cm/pixel	4.06 cm/pixel
NIR	2.03 cm/pixel	4.06 cm/pixel
TIR	6.25 cm/pixel	12.50 cm/pixel
SWIR	7.50 cm/pixel	15.0 cm/pixel

Table 4.2: Specifications of the NIR/RGB camera

Camera	NIR/RGB
Image width (horizontal, pixels)	4608
Image height (vertical, pixels)	3456
Focal length (mm)	4.0
CCD-width (mm)	6.17
CCD-height (mm)	4.63

Table 4.3: Specifications of the TIR camera

Camera	TIR
Image width (horizontal, pixels)	640
Image height (vertical, pixels)	480
Focal length (mm)	1.0
CCD-width (mm)	0.8
CCD-height (mm)	0.6
Spectral band (μm)	7-14
Accuracy (°C)	± 1

Table 4.4: Specifications of the SWIR camera

Camera	SWIR
Image width (horizontal, pixels)	320
Image height (vertical, pixels)	240
Focal length (mm)	1
CCD-width (mm)	0.4
CCD-height (mm)	0.3
Spectral band (μm)	0.9-1.7

control points in the field. To exclude non-canopy pixels for post-processing, all the tree canopies in three blocks are segmented manually in the NIR image, the image collected via the NIR camera. This NIR image is georeferenced as well and served as the mask for images of red, green, blue, TIR and SWIR bands. During the process, all these images are in the format TIF.

Besides three bands red, green and blue in the RGB camera (Survey 2, MAPIR, USA), two bands red and NIR in the camera NIR (Survey 2, MAPIR, USA), two more layers are added in the image array. One layer is the difference between the NIR band and the red band, as described in Equ. 4.1, where DN_{NIR} and DN_{red} stand for digital value for a pixel. The other layer is normalized difference, in the format of Equ. 4.2, where pixels with zero sum of DN_{NIR} and DN_{red} are filtered out. The band difference layer and the normalized difference layer are used red and NIR bands from the NIR camera (Survey 2, MAPIR, USA). Therefore, canopy images of 7 layers serve as input for irrigation treatment classification.

$$DVI = DN_{NIR} - DN_{red}. \tag{4.1}$$

$$NDVI = \frac{DN_{NIR} - DN_{red}}{DN_{NIR} + DN_{red}}. \tag{4.2}$$

The canopy pixels and their coordinates for each tree are extracted using the function *regionprops* in MATLAB2013b (Mathworks, USA). An irrigation treatment label is assigned to a tree according to which irrigation experiment plot it is planted in. Classification studies are based on Python libraries scikit-learn [179].

Finally, the dataset for irrigation treatment classification includes an orthomosaic TIF image of 7 layers, with spatial resolution of 2.03 cm/pixel, covering the middle block of 285 trees, and irrigation treatment labels for all these 285 trees. These 285 trees are divided into two parts, 75% of the trees used for training and 25% used for validation. The designed classifiers are evaluated using 5-fold cross-validation. The accuracies of these classifiers are evaluated using the fraction of correctly classified samples in the validation dataset.

4.2.2 Descriptive Statistics

Given a dataset, when there exists a strong central tendency that these values cluster around a particular value, it maybe useful to summarize the set by its moments [180].

Denoting this data set of N values as $x1, x2, ..., x_n$, the mean of these values is defined as,

$$x_{mean} = \frac{1}{N}\sum_{i=0}^{N}(x_i). \tag{4.3}$$

Having the central value of a dataset characterized by mean, another measure is to characterize its "width" around mean. One of the most popular measures is the variance,

$$x_{var} = \frac{1}{N-1}\sum_{i=1}^{N}(x_i - x_{mean}), \tag{4.4}$$

or the standard deviation, the square root of the variance,

$$\sigma = \sqrt{\frac{1}{N-1}\sum_{i=1}^{N}(x_i - x_{mean})}. \tag{4.5}$$

The skewness is used to characterize the degree of asymmetry around the mean of a distribution. Its definition is

$$x_{skewness} = \frac{1}{N}\sum_{i=1}^{N}(\frac{x_i - x_{mean}}{\sigma})^3. \tag{4.6}$$

.

The kurtosis is to measure the relative peakedness or flatness of a distribution to a normal distribution, defined as

$$x_{kurtosis} = \{\frac{1}{N}\sum_{i=1}^{N}(\frac{x_i - x_{mean}}{\sigma})^4\} - 3. \tag{4.7}$$

A positive skewness signifies a distribution whose asymmetric tail is extending towards right and a negative skewness signifies distribution with a tail extending towards left. In other words, the mass of a left-skewed distribution is leaning to the right, whereas the mass of a right-skewed distribution is leaning to the left [181].

A kurtosis less than three means the distribution produces less extreme outliers than the normal distribution. For example, the uniform distribution has a smaller kurtosis, and it does not produce outliers. A distribution with the kurtosis greater than three produces more outliers, such as Laplace distribution [182].

4.2.3 Dimensionality Reduction

4.2.3.1 Principal Component Analysis

Principal component analysis (PCA) is a projection method that can project the inputs from the original space to a new space, where the variances of the inputs are maximized along the principal components.

Denote a measurement $\boldsymbol{x}$ containing d attributes as $(x_1, x_2, ..., x_d)^T$, then N measurements can be viewed as a data matrix:

$$\boldsymbol{X} = \begin{bmatrix} x_1^1 & x_1^2 & ... & x_1^N \\ x_2^1 & x_2^2 & ... & x_2^N \\ ... & & & \\ x_d^1 & x_d^2 & ... & x_d^N \end{bmatrix}. \tag{4.8}$$

Its projection on the new direction $\boldsymbol{w}_1$, the first principal component, is

$$\boldsymbol{z}_1 = \boldsymbol{w}_1^T\boldsymbol{X}. \tag{4.9}$$

The variance of the projection is

$$\mathrm{Var}(\boldsymbol{z}_1) = \boldsymbol{w}_1^T\boldsymbol{\Sigma}\boldsymbol{w}_1, \tag{4.10}$$

where $\boldsymbol{\Sigma}$ is the covariance matrix $\mathrm{Cov}(\boldsymbol{X})$. To obtain a unique solution, it is set that $\|\boldsymbol{w}_1\|^2 = 1$. Then the problem is described as

$$\begin{aligned} &\max_{\boldsymbol{w}_1} \mathrm{Var}(\boldsymbol{z}_1) \\ &s.t \;\; \|\boldsymbol{w}_1\|^2 = 1. \end{aligned} \tag{4.11}$$

According to the Lagrange method, the following equation holds

$$\boldsymbol{\Sigma} \boldsymbol{w}_1 = \alpha \boldsymbol{w}_1. \tag{4.12}$$

Substituting equation 4.15 into equation 4.10, the variance is

$$\mathrm{Var}(\boldsymbol{z}_1) = \boldsymbol{w}_1^T \boldsymbol{\Sigma} \boldsymbol{w}_1 = \alpha. \tag{4.13}$$

Therefore, the maximum variance can be obtained by choosing the largest eigenvector of the covariance matrix, and the principal component is the eigenvector with that largest eigenvalue.

For the second principal component $\boldsymbol{w}_2$, it is also required to be orthogonal to $\boldsymbol{w}_1$, in addition to the property of unit length and maximum variance of the projection

$$\boldsymbol{w}_1^T \boldsymbol{w}_2 = 0. \tag{4.14}$$

Again, according to the Lagrange method, the following equation holds

$$\boldsymbol{\Sigma} \boldsymbol{w}_2 = \alpha \boldsymbol{w}_2, \tag{4.15}$$

which indicates that $\boldsymbol{w}_2$ is the eigenvector with the second largest eigenvalue of the covariance matrix. Similarly, the other principal components can be obtained by eigenvectors with smaller eigenvalues.

4.2.3.2 Linear Discriminant Analysis

Rather than PCA, an unsupervised method that does not use class label information, Fisher-linear discriminant analysis (LDA) is a supervised method for dimensionality reduction [183].

Considering a problem of two classes, the purpose of LDA is to find the direction $\boldsymbol{w}$, so that after the data $\boldsymbol{x}$ are projected along $\boldsymbol{w}$, the data are separated as well as possible. Denoting the between-classes scatter matrix as

$$\boldsymbol{S}_B = (\boldsymbol{\mu}_1 - \boldsymbol{\mu}_2)(\boldsymbol{\mu}_1 - \boldsymbol{\mu}_2)^T, \tag{4.16}$$

the within-classes scatter matrix as

$$\boldsymbol{S}_W = \sum_{c=1,2} \sum_{i \in c} (\boldsymbol{x}_i - \boldsymbol{\mu}_c)(\boldsymbol{x}_i - \boldsymbol{\mu}_c)^T, \tag{4.17}$$

Fisher's linear discriminant is to find the direction maximizing

$$\boldsymbol{J}(\boldsymbol{w}) = \frac{\boldsymbol{w}^T \boldsymbol{S}_B \boldsymbol{w}}{\boldsymbol{w}^T \boldsymbol{S}_w \boldsymbol{w}}, \tag{4.18}$$

where $\boldsymbol{\mu}_c$ is the means of data in classes $c = \{1, 2\}$. In the case of K $(K > 2)$ classes, it amounts to finding the matrix $\boldsymbol{W}$ to maximize

$$\boldsymbol{J}(\boldsymbol{w}) = \frac{|\boldsymbol{W}^T \boldsymbol{S}_B \boldsymbol{W}|}{|\boldsymbol{W}^T \boldsymbol{S}_W \boldsymbol{W}|}, \tag{4.19}$$

where $\boldsymbol{S}_B$ is the between-classes scatter matrix,

$$\boldsymbol{S}_B = \sum_{c=1}^{K} (\boldsymbol{\mu}_c - \bar{\boldsymbol{x}})(\boldsymbol{\mu}_c - \bar{\boldsymbol{x}})^T, \tag{4.20}$$

$\boldsymbol{S}_W$ is the within-classes scatter matrix,

$$\boldsymbol{S}_W = \sum_{c=1}^{K} \sum_{i \in c} (\boldsymbol{x}_i - \boldsymbol{\mu}_c)(\boldsymbol{x}_i - \boldsymbol{\mu}_c)^T \tag{4.21}$$

$\bar{\boldsymbol{x}}$ is the overall mean of all classes c and the determinant is used to measure the spread of a scatter matrix.

4.2.4 Artificial Neural Network

ANN is a computational model developed under inspiration from the human brains [184]. It can be used for both classification and regression.

The structure of ANN with one hidden layer ANN is shown in Fig. 4.2. At the top, $o_k, k = 1, 2, ..., K$ are outputs of the network. Each output o_k is a weighted sum of the hidden units $z_m, m = 1, 2, ...M$,

$$o_k = \sum_{m=1}^{M} w_{km} z_m + w_{k0}. \tag{4.22}$$

Hidden units z_m are defined as

$$z_m = \sigma(\sum_{p=1}^{P} v_{mp} x_p + v_{m0}), \tag{4.23}$$

where $\sigma(\cdot)$ is an activation function and $x_p, p = 1, 2, ..., P$ are the inputs. Some popular activation functions are the sigmoid function, the hyperbolic tangent function and Gaussian radial basis function.

For a K-class classification problem, the outputs are transformed further via softmax functions to indicate the probability of the class k,

$$y_k = \frac{e^{o_k}}{\sum_{k=1}^{K} e^{o_k}}, k = 1, 2, .., K, \tag{4.24}$$

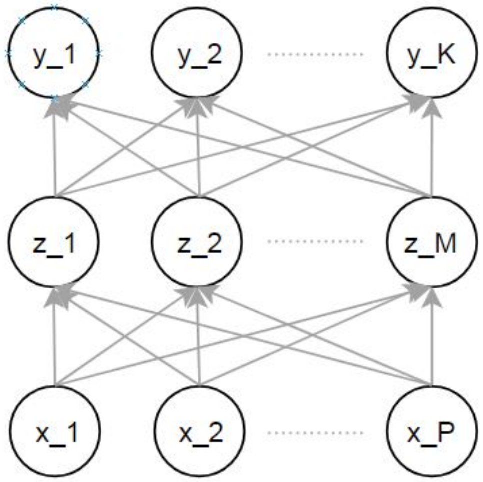

Figure 4.2: The structure of a single hidden layer neural network

and the error function is

$$E_\theta = -\sum_{k=1}^{K}\sum_{i=1}^{N} r_{ik}\log y_{ik}, \tag{4.25}$$

where θ is the set of weights, r_{ik} is the desired class label for the sample input $\boldsymbol{x}_i = [x_{i1}, x_{i2}, ..., x_{iP}], i = 1, 2, ..., N$, N is the number of samples,

$$r_{ik} = \begin{cases} 1 & if\ \boldsymbol{x}_i \in C_k \\ 0 & if\ \boldsymbol{x}_i \in C_t, t \neq k \end{cases}. \tag{4.26}$$

Finally, weights are obtained by minimizing the error function E_θ using back-propagation [185]. More than one hidden layers are applied to implement more complex functions, but many hidden layers will cause the network hard to analyze [186].

4.2.5 Distribution Distance

In addition to classification based on linear dimensionality reduction PCA and LDA, and nonlinear dimensionality reduction ANN, there is another type classification methods called non-parametric methods. Instead of making any assumption about the data input, it only assumes that similar inputs have similar outputs. It makes prediction based on its nearby training instances using a suitable distance measure.

Many studies [187, 188] have been published on finding distance measures because it is very important in classification, clustering problems [189]. Generally, these distance measures for histograms can be divided into two types: bin-to-bin and cross-bin [190].

Given two histograms $\boldsymbol{P}$ and $\boldsymbol{Q}$, each histogram contains n bins, with the value at the bin i denoted as P_i and Q_i respectively.

Examples of bin-to-bin measures are Euclidean distance (4.27), city block distance (4.28), Minkowski distance (4.29), Sørensen distance (4.30) [191], fractional distance [192], intersection (4.31) [189], inner product (4.32) [189], fidelity (4.33) [193], Chi square distance (4.34) [194], KL (Kullback-Leibler) divergence (4.35) [195].

$$d_{Euc} = \sqrt{\sum_{i=1}^{d} |P_i - Q_i|^2} \tag{4.27}$$

$$d_{city} = \sum_{i=1}^{d} |P_i - Q_i| \tag{4.28}$$

$$d_{Mink} = \sqrt[p]{\sum_{i=1}^{d} |P_i - Q_i|^p} \tag{4.29}$$

$$d_{S\o r} = \frac{\sum_{i=1}^{d} |P_i - Q_i|}{\sum_{i=1}^{d} (P_i + Q_i)} \tag{4.30}$$

$$d_{inter} = \sum_{i=1}^{d} min(P_i, Q_i) \tag{4.31}$$

$$d_{inner} = \sum_{i=1}^{d} (P_i Q_i) \tag{4.32}$$

$$d_{fid} = \sum_{i=1}^{d} \sqrt{(P_i Q_i)} \tag{4.33}$$

$$d_{Chi} = \frac{1}{2} \sum_{i=1}^{d} \frac{(P_i - Q_i)^2}{P_i + Q_i} \tag{4.34}$$

$$d_{KL} = \sum_{i=1}^{d} P_i ln \frac{P_i}{Q_i}. \tag{4.35}$$

Mahalanobis distance (4.36) [196] is one example of cross-bin distance,

$$d_{Mah} = \sqrt{(\boldsymbol{P} - \boldsymbol{Q}) \boldsymbol{S}^{-1} (\boldsymbol{P} - \boldsymbol{Q})}, \tag{4.36}$$

where $\boldsymbol{S}$ denotes the covariance matrix.

Table 4.5: Accuracies of treatment classification using ANN and moments

Features	Accuracy(%)	Hidden Layer Setting
Mean	46.94	(15, 15)
Mean+Variance	51.94	(13, 15)
Mean+Variance+Skewness	54.16	(17, 5)
Mean+Variance+Skewness+Kurtosis	52.50	(5, 17)

4.3 Results and Discussion

4.3.1 Treatment Classification Using Descriptive Statistics

Considering mean as the first order moment statistics for the canopy pixel distribution, it is necessary to use one order moment features as well as higher order moment features to extract more information from the distributions.

To explore whether higher order moment features can extract more information and increase classification accuracy, four classifiers using ANN are designed for the image input of 7 layers. These ANN classifiers are implemented in Scikit-learn [179], where the solver for weights optimization is 'lbfgs', L2 penalty (regularization term) parameter α is set to 1e-05, and all the other parameters are default setting. There are two hidden layers and the number of hidden neurons for each layer is determined by using grid search in the range 5 to 20, with the step of 2.

The first classifier uses means of 7 layers as input, where each tree is described with a vector of 7 dimensions. The second classifier uses means and variances of 7 layers as input, where each tree is described with a vector of 14 dimensions. Similarly, the third classifier based on means, variances and skewness has a input of 21 dimensions, and the forth classifier based on means, variances, skewness and kurtosis has an input of 28 dimensions.

Table 4.5 lists the accuracies and hidden layer setting of these four classifiers. It can be seen that adding features of higher order moments increases the accuracy of irrigation treatment classification. Compared with the mean-based classifier, the mean-variance-based classifier gains an accuracy increase of 5%. Adding skewness features increases the accuracy with another around 3%. Adding kurtosis features does not increase the accuracy further, though its performance is still better than mean-based classifier with 5%. The reason might be that large number of features makes the classifier overfitted in the relatively small training set.

4.3.2 Treatment Classification Using Dimensionality Reduction

Both means and other higher order moments can be considered as a process of dimensionality reduction for the target canopy pixel distribution. According

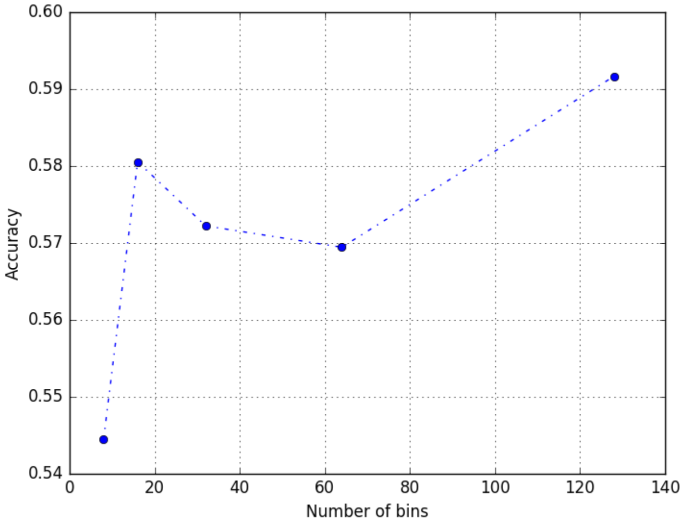

Figure 4.3: Comparing accuracies of treatment classification using ANN and histograms with different bin sizes

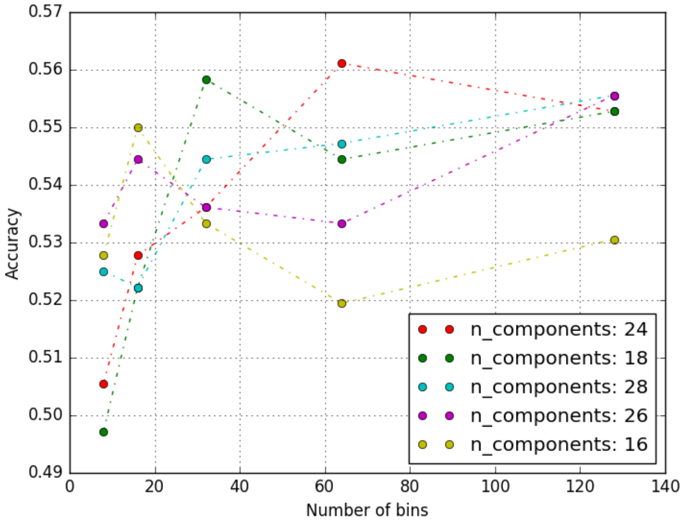

Figure 4.4: Comparing accuracies of treatment classification using ANN, PCA with different number of extracted components, histograms with different bin sizes

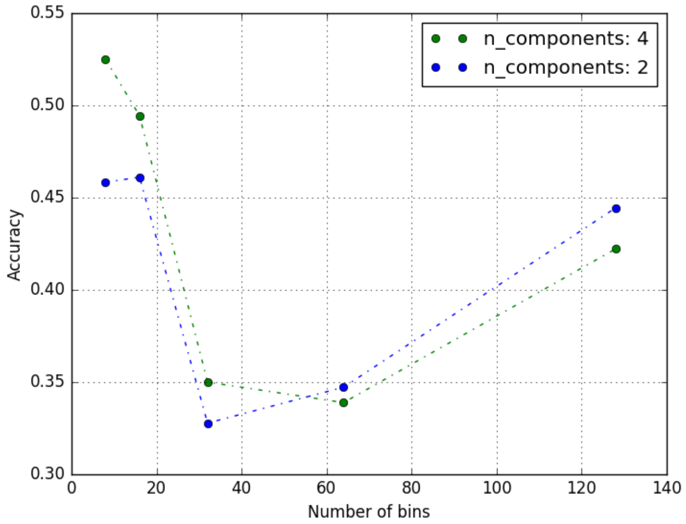

Figure 4.5: Comparing accuracies of treatment classification using ANN, LDA with different number of extracted components, histograms with different bin sizes

to this viewpoint, many other dimensionality reduction methods can also help extract information from distributions for treatment classification. One of the popular methods to describe distributions is to use histograms. Therefore, dimensionality reduction methods based on histograms are more general approaches to extract related information.

The two most popular dimensionality methods are PCA and LDA, where PCA is unsupervised and LDA is supervised. Both of these methods are linear transformation of inputs. Considering ANN can not only serve as a classifier but also a dimensionality reduction method, ANN can be an option of a nonlinear transformation. Thus, three models based on canopy pixel distributions are explored for treatment classification, PCA plus ANN, LDA plus ANN, and ANN. At the same time, the number of components in PCA, LDA and the number of bins in histograms are studied in these experiments.

The ANN configurations for these three types of models are the same as Section 4.3.1. The number of components for both PCA and LDA is searched between 2 to 28, where the maximum number of components is the same as the input dimension of the classifier with means, variances, skewness and kurtosis features.

Five different bin sizes are explored at 8, 16, 32, 64, 128. The histogram of a tree for one layer is extracted using minimum value and maximum values among pixel DN values of all the trees in the same layer. The histograms of 7 layers are

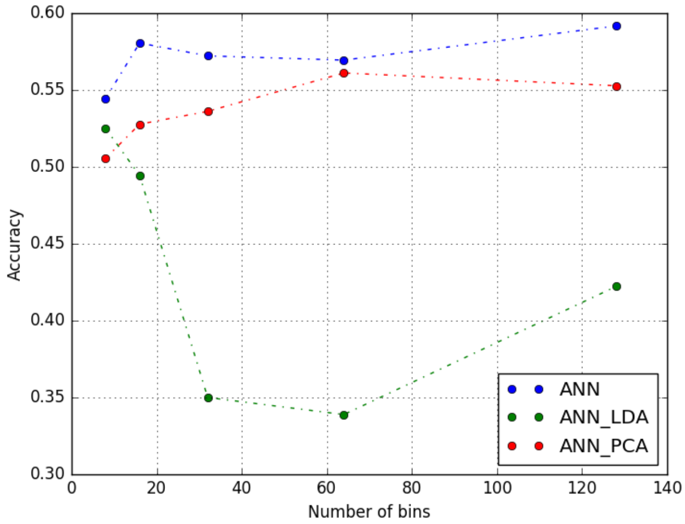

Figure 4.6: Comparing accuracies of treatment classification using ANN, LDA plus ANN, PCA plus ANN based on histograms with different bin sizes

then concatenated into one histogram for each tree. For example, when the number of bins is set as 8, the feature vector for each tree would be 56 dimensions.

Results of the classifier using ANN are in Fig. 4.3. Results of PCA plus ANN classifiers are in Fig. 4.4 where top five classifiers are plotted. Results of LDA plus ANN classifiers are in Fig. 4.5. Only the classifiers with the number of components at 2, 4 are plotted, because the results of classifiers with more than 4 components are the same as the classifiers with 4 components.

It can be seen that the best performance of ANN classifiers is with 128 bins in histograms. For PCA plus ANN classifiers, the best performance is achieved with 24 components and 64 bins in the histograms. LDA plus ANN classifiers achieve the best performance with 4 components and 8 bins.

ANN, PCA plus ANN, LDA plus ANN classifiers are compared in Fig. 4.6, which shows that the best model is ANN with 128 bins. This indicates that the irrigation treatment related features might be nonlinear transformations of original input. Furthermore, it can be seen that this model is also better than the model based on moments with an accuracy improvement by around 5%.

4.3.3 Treatment Classification Using Distribution Distance

Another type of classifiers is called distance based methods, a type of non-parameter model. Instead of transforming original input space to lower dimension

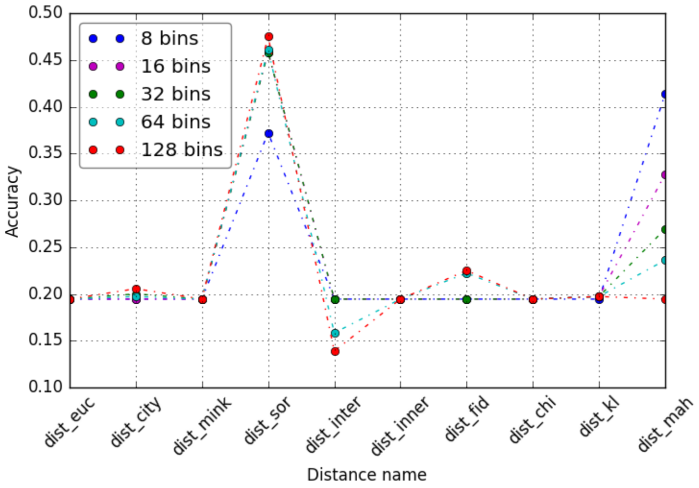

Figure 4.7: Comparing accuracies of treatment classification using KNN and different distribution distances.

feature space, distance based methods operate in original input space. This saves effort for extracting features, although high dimensions of the input cause big variance in the model performance.

KNN classifiers using ten different distribution distances described in Section 4.2.5 are evaluated based on canopy pixel histograms. Two other hyperparameters are explored, the number of nearest neighbors k at $5, 7, 9, 11, 13, 15$ and the bin sizes of histograms at $8, 16, 32, 64, 128$.

Because there exist negative values in band difference and normalized band difference, the input for the distance based classifiers is only with 5 layers, with layers of band difference and normalized band difference excluded. Similar to Section 4.3.2, histograms of 5 layers are concatenated into one histogram for each tree, and then the distance is calculated based on these concatenated histograms between trees.

The results of these classifiers are plotted in Fig. 4.7, where only the classifier with the best k is chosen. It shows that most distances do not perform well except Sørensen distance and Mahalanobis distance. The best performance is achieved with Sørensen distance and histograms of 128 bins. Its performance is as good as the ANN classifier using means of 7 layers input. It is interesting that the format of Sørensen distance is similar to traditional normalized difference, although Sørensen distance adding the difference and distribution respectively before normalization.

4.4 Chapter Summary

In this Chapter, a new methodology for fully leveraging the high spatial resolution of UAV-based remote sensing is proposed. According to this methodology, the physical band can be considered as a layer. A vegetation index can also be viewed as a new layer. In addition, each pixel in a layer of a tree is considered as an observation for the tree. Then classification or regression using tree canopy pixels can rely on dimensionality reduction to extract more related information.

As a case study, three types of models are built for irrigation treatment classification, moments based classifiers, histograms based classifiers and distance based classifiers. Experiments show that the best model is ANN with histograms of 128 bins, which produces an accuracy of 69%, 12% better than the model only using means as feature input. In addition, as a simple non-parameter classifier, Sørensen distance based KNN model also shows promising results.

The implications for UAV-based remote sensing based precision agriculture practice are as follows.

- High resolution images enable plant health monitoring in the single-plant level. This provides more flexibility for both feature description and extraction.
- Canopy histograms help keep more information to describe plant health.
- For the analysis of plant health in the instance level, beyond-mean feature extraction can yield better classification accuracy.
- For a certain application, nonlinear feature extraction might work better than linear feature extraction. For example, as a feature extraction method, ANN might work better than both PCA and LDA.

Chapter 5

DEPENDENCE OF IRRIGATION TREATMENT AND VARIETY CLASSIFICATION ON IMAGE COLLECTION

5.1 Introduction

As discussed in Chapter 2, UAV-based remote sensing can be divided into three steps, image collection, image pre-processing and image post-processing. Unlike traditional satellite-based remote sensing, UAV-based remote sensing provides great flexibility in image collection. Image spatial resolution can be modified by flying the vehicles at different altitudes. Image spectral resolution can be configured via mounting different cameras. Other adjustable factors during image collections may include image formats, image overlap, flight speed, imaging angles and flight time window etc.

So far, the main research focus on UAV-based remote sensing is image pre- and post-processing, whereas little attention is put on image collection and its effect on final quantitative analysis. In [197], optimal vegetation index global environment monitoring index (GEMI) was proposed with the guidelines that optimal index should be very sensitive to the desired vegetation property but not sensitive to possible perturbing factors such as soil background and atmospheric effects. Various functions based on the red and near-infrared reflectances were evaluated in an approach that isolines of these functions were orthogonal to the displacements because of target properties. In [198], optimal band was identified under the assumption that the linear relationships between the vegetation index and green leaf area index (LAI) had similar slopes and intercepts for four different crops of maize, potato, soybean and wheat. When the NIR band was fixed in the range of 841-876 nm, the other band was tuned between 500 nm and 750 nm. Most recently, optimization criteria for remote sensing was proposed in [199] with regard to spatial resolution, spectral bands and optimal time, yet no experiments were provided for further discussion.

Moving forward from Chapter 4, this Chapter studies how various factors in UAV-based remote sensing affect the final analysis results and what is the best practice. Examples of these factors include spatial resolution, spectral band configuration, image registration and image formats. To avoid problems dependent conclusions, these factors are evaluated according to classification accuracies in two problems, irrigation treatment classification and treat variety classification.

The rest of this Chapter is organized as follows. Data collection and preprocessing, basics of image registration and image formats are described in Section 5.2. In Section 5.3.1, effects of spatial resolution under the same band configuration on classification accuracies are discussed. Effects of band configuration on classification accuracies under the same spatial resolution are presented in Section 5.3.2. How image fusions of different band configuration and spatial resolution affect accuracies is studied in Section 5.3.3. In Section 5.3.4, effects of image band-to-band registration are presented. In Section 5.3.5, classification accuracies using images of different formats are compared. Finally, best UAV-based remote sensing practices are described based on results of these experiments.

5.2 Materials and Methods

5.2.1 Data Collection

This study continues to use the data collected in Section 4.2.1. Images of different spatial resolution but same band configuration were collected via flights at 120 m and 60 m AGL using the same cameras. Images of different band configuration were collected using four different cameras, RGB, NIR, TIR and SWIR cameras. Images of same spatial resolution but different band configuration were obtained by registering RGB, NIR and TIR orthomosaic images to SWIR orthomosaic images after downsampling in ArcGIS (Esri, USA).

Variety labels for each tree are provided by the owner of the almond orchard. Experiments are based on Python library Scikit-learn [179]. Similar as Section 4.2, the dataset includes 285 trees in the middle block, and two labels for each tree, irrigation treatment and variety. 75% of the trees are in the training dataset and 25% of the trees are in the validation dataset. 5-fold cross-validation is used to evaluate accuracies of different models using ANN based on histograms of canopy pixels. Configuration of the ANN model is the same as Section 4.3.1.

5.2.2 Image Registration

Image registration, as a fundamental process in remote sensing, align images of different spectral bands and different times [200]. It has a significant impact on remote sensing tasks, such as change detection and image fusion [201].

Even misalignment greater than 0.25 pixels can be visually noticed in pseudocolor image [202]. In [203], the impact of band-to-band registration in moderate resolution imaging spectroradiometer (MODIS) images was analyzed. Snow classification results were compared using MODIS snow mapping algorithm before and after registration correction, via which the image was shifted one pixel in the track direction and kept unchanged in the scan direction. 8% out of around 2000 pixels were classified differently because of the correction, and the correlation coefficient between band 4 and 7 changed from 0.115 to 0.405.

In addition to band-to-band shift error, image registration also introduces pixel DN value changes during resampling and interpolation. For example, polar Stockwell transform (PST) energy was used to analyze the impact of image registration on textures of magnetic resonance imaging (MRI) [204]. Results showed that resampling by using linear, Blackman and B-spline led to significant difference between interpolated images and original images.

Although many methods have been proposed for automatic image registration [200, 205], the most popular approach still uses ground control points [206]. It was shown that, 15 to 20 ground control points out of 160 images are required to achieve good accuracy for image registration, where RMSE_X and RMSE_Y are 3.3±0.346 cm and 3.2±0.441 cm, similar as flight GSD of 3.291 cm.

5.2.3 Image Formats

Image formats are also an important consideration for remote sensing using digital cameras [207]. In most digital cameras, there are two popular image formats, tagged image file format (TIFF or TIF) and joint photographic expert group (JPEG or JPG). TIF files support lossless compression, so images can be saved without introducing information loss. JPG uses loss compression, which makes JPEG files significantly smaller than those of TIF. It compresses images by retaining image details that are most visually impactful and by taking the advantages that brightness difference is more noticeable than color difference to human eyes [208].

Considering limited flight time of small unmanned aerial vehicles, it is desired that cameras can capture images at a high speed. A higher capture speed means more images are collected during a flight and hence larger area can be covered within a single flight. The capture speed of a camera in JPG configuration is twice or ten times as that in TIF or RAW configuration. For example, the NIR camera (Survey 2, MAPIR, USA) supports JPG video collection. It takes three seconds to capture one RAW image.

It showed that mean reflectances calculated from JPG and TIF are the same over a micro plot [209]. Again, in a plot level, mean normalized green-red difference index calculated from JPG images was shown to be linear correlated with the mean normalized difference between green and red reflectances [210]. Similar studies showed that, mean vegetation indices from JPG images provided results as good as mean vegetation indices from TIF images in the target plots [211]. Soil color indices based on average of the values in JPG images indicated similar or better correlation than the field spectrometer [212].

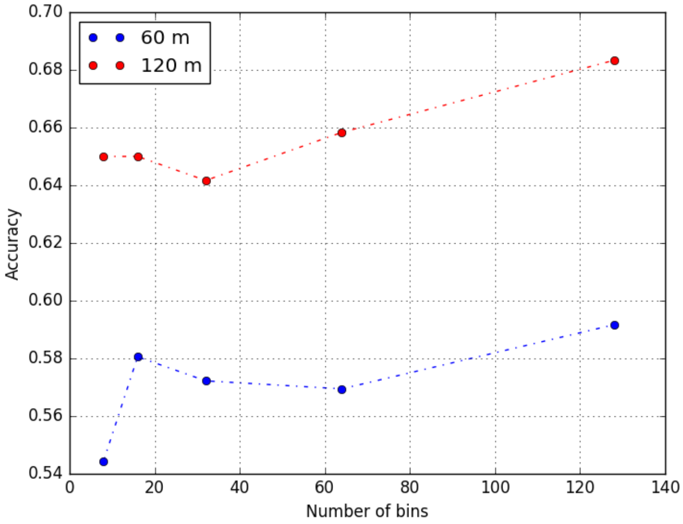

Figure 5.1: Comparing accuracies of treatment classification using images of same bands but different spatial resolution.

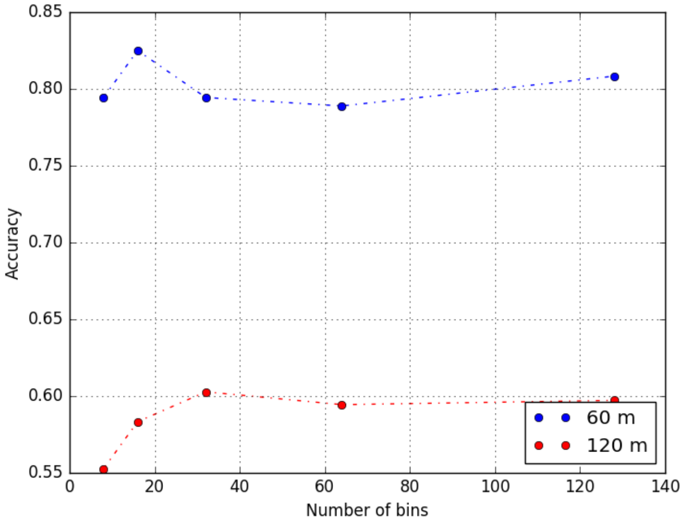

Figure 5.2: Comparing accuracies of variety classification using images of same bands but different spatial resolution.

5.3 Results and Discussion

5.3.1 Effects of Spatial Resolution on Irrigation Treatment and Variety Classification

Two orthomosaic images are used to compare classification accuracies of different spatial resolution. One image is with the resolution 2.03 cm/pixel collected at 60 m. The other is with the resolution 4.06 cm/pixel collected at 120 m. Both images include 7 layers, red, green, blue bands provided in the RGB camera (Survey 2, MAPIR, USA), red and NIR bands in the camera NIR (Survey 2, MAPIR, USA), difference and normalized difference between the red band and the NIR band.

The performance of treatment classification at 60 m and 120 m is plotted in Fig. 5.1 and the performance of variety classification is plotted in Fig. 5.2. Surprisingly, it shows that higher spatial resolution does not always help improve the accuracy. Lower spatial resolution helps increase the accuracy of treatment classification from 59% to 68%, whereas higher spatial resolution increases the accuracy of variety classification from 60% to 83%. In addition, more bins in the histograms help increase the accuracy of treatment classification, whereas the best accuracy of variety classification is achieved at 8 bins.

It could be explained that lower spatial resolution helps filter high frequency noise, which might cause trouble for later feature extraction with regard to certain applications. On the other hand, for some applications, high frequency information might be part of the target features.

Generally speaking, more bins in histograms provide better description about distributions, and hence help increase classification accuracy. Although there is a saturation effect in the parameter, the accuracy does not increase further with the number of bins. Sometimes better performance is achieved with 8 bins in histograms than that with 16 bins and this might be due to better optimization result with less input dimensions.

5.3.2 Effects of Band Configuration on Irrigation Treatment and Variety Classification

An orthomosaic image with 9 layers is used to compare accuracies under different band configurations. These 9 layers include the red band, the green band and the blue band from the RGB camera (Survey 2, MAPIR, USA), the red band and the NIR band from the NIR camera (Survey 2, MAPIR, USA), difference and normalized difference between the red band and the NIR band of the NIR camera (Survey 2, MAPIR, USA), the TIR band, and the SWIR band. Spatial resolution of all these 9 layers is 7.50 cm/pixel.

Five different band configurations are explored in this experiment for classification of treatments and varieties, the first 7 layers, the first 7 layers plus the TIR band, the first 7 layers plus the SWIR band, the 7 layers plus both the TIR band and the SWIR band.

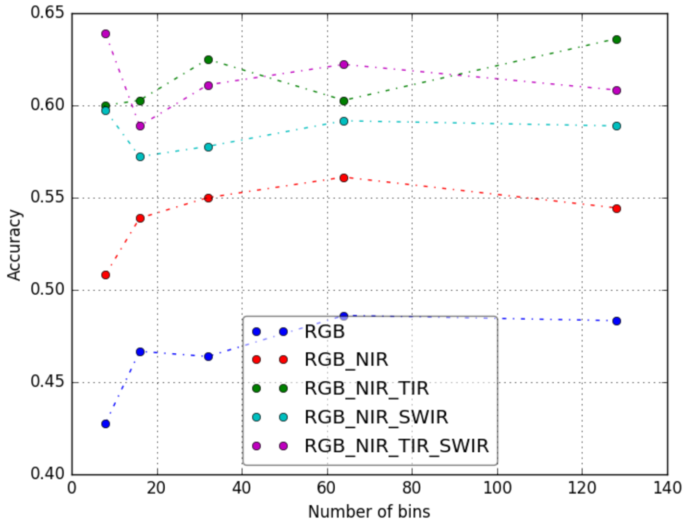

Figure 5.3: Comparing accuracies of treatment classification using images of same spatial resolution but different bands.

The results of treatment classification are in Fig. 5.3 and the results of variety classification are in Fig. 5.4. For both treatment and variety classification, adding the NIR band does help significantly.

For treatment classification, adding the TIR band or the SWIR band can further increase the accuracy by almost 5%. It shows that the TIR band helps increase the accuracy better than the SWIR band. 8 layers configuration with the TIR band can achieve almost the same accuracy as the configuration of 9 layers with both the TIR band and the SWIR band, showing that the TIR band has better sensitivity to irrigation effects on almond trees.

According to Fig. 5.1, lower resolution helps increase the treatment classification accuracy. However, further lower resolution does not increase the accuracy,but rather reduces it from 68% to 55%. This difference might also come from artificial downsampling such as nearest neighbor or bilinear resampling, where some information gets lost.

For variety classification, adding the TIR band or the SWIR band does not further improve the classification accuracy too much, although the best accuracy is achieved with 9 layers of spectral configuration, around 3% better than the accuracy without the TIR band or the SWIR band.

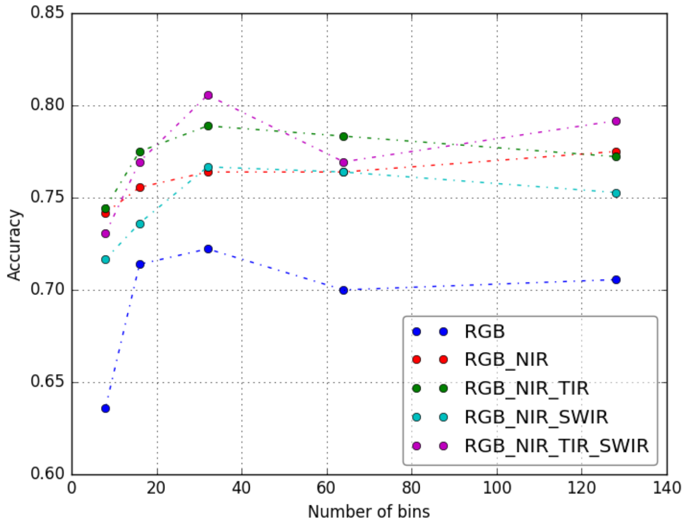

Figure 5.4: Comparing accuracies of variety classification using images of same spatial resolution but different bands.

5.3.3 Effects of Combining Images of Different Spectral Bands and Different Spatial Resolutions on Irrigation Treatment and Variety Classification

Because specifications of various cameras are not the same, the spatial resolutions of obtained images between bands are usually different. Traditional practice to use all these images is based on band-to-band image registration. During this process, images of source bands are either downsampled or upsampled to the same resolution as the image in the target band for further registration.

Enabled by instance-segmentation of trees, image registration in the pixel level is no longer needed. It is only necessary to register two images in the instance level, which is much easier and saves lots of effort for ground control point calibration.

Three stitched orthomosaic images are prepared for experiments. The first image RGB_NIR is collected using the RGB camera (Survey 2, MAPIR, USA) and the NIR camera (Survey 2, MAPIR, USA), with the spatial resolution of 2.03 cm/pixel. It contains the red band, the green band and the blue band from the RGB camera (Survey 2, MAPIR, USA), the red band and the NIR band from the NIR camera (Survey 2, MAPIR, USA), difference and normalized difference between the red band and the NIR band of the NIR camera (Survey 2, MAPIR, USA). These layers are registered band to band in the pixel level to obtain the layers of difference

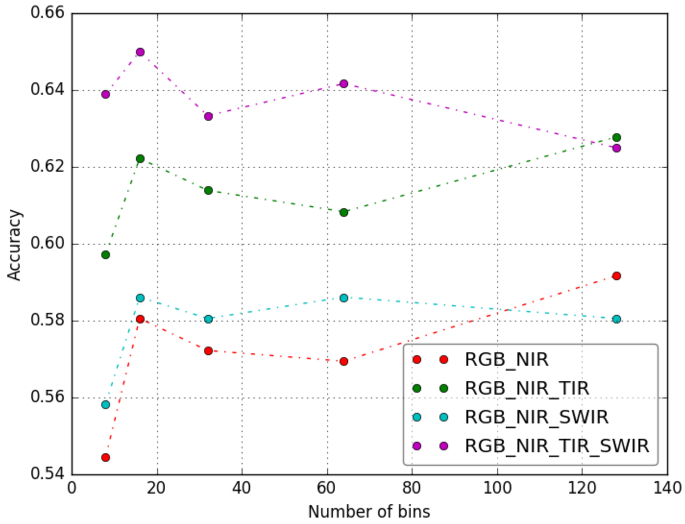

Figure 5.5: Comparing accuracies of treatment classification using fused images of different bands and different spatial resolution.

and normalized difference. The second image and the third image are in the TIR band and the SWIR band respectively. These two images are registered band to band in the pixel level, and they have the same spatial resolution 7.5 cm/pixel. For abbreviation, these three images are denoted as RGB_NIR, TIR and SWIR.

Four fusions of these three images are RGB_NIR, RGB_NIR and TIR, RGB_NIR and SWIR, RGB_NIR, TIR and SWIR. Note that RGB_NIR and TIR, SWIR are registered in the tree level, not in the pixel level. The histograms of RGB_NIR, TIR and SWIR were then concatenated for each tree as the classifier input.

The results are shown in Fig. 5.5 and Fig. 5.6. For treatment classification, similar results are obtained to Fig. 5.3. SWIR helps increase the accuracy slightly, whereas TIR increased the accuracy a lot. For variety classification, similar to Fig. 5.3, SWIR and TIR do not add extra improvement in the accuracy. The accuracy becomes even worse with fusion of more layers into RGB_NIR images. This indicates that adding more layers does not always help increase the accuracy. The best band fusion strategy is really application dependent.

5.3.4 Effects of Image Registration on Irrigation Treatment and Variety Classification

In Section 5.3.3, although RGB_NIR and SWIR, TIR are registered in the tree level, difference and normalized difference layers are still included in the RGB_NIR

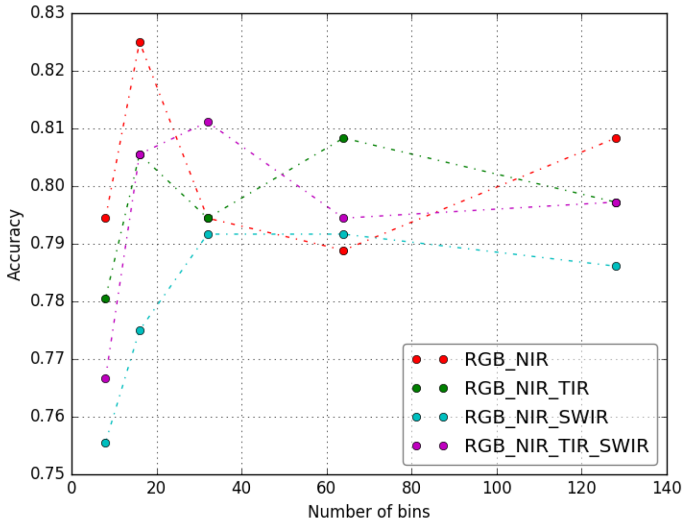

Figure 5.6: Comparing accuracies of variety classification by fused images of different bands and different spatial resolution.

image. In the purpose of figuring out how much gains in accuracy introduced by the layers of difference and normalized difference, accuracies of images with and without the layers of difference and normalized difference are compared.

As shown in Fig. 5.7 and Fig. 5.8, accuracies of treatment classification improve by 5% with layers of difference and normalized difference, and accuracies of variety classification increase only 2%. Therefore it does help by adding layers of difference and normalized difference, but the improvement of accuracies depends on the specific application.

5.3.5 Effects of Image Formats on Irrigation Treatment and Variety Classification

Published research shows means of vegetation indices extracted from JPG or TIF images are similar. In the hope that the proposed feature extraction methods have better capability to extract information, classification accuracies of treatments and varieties are compared with images of different formats.

Images of different formats are made in the image pre-processing. Two configurations to generate orthomosaic images determine the image formats. This first one is to choose the desired format to convert individual RAW camera images for further stitching. The second is to choose the desired format to export the stitched orthomosaic image. Therefore, there are four possible different image formats to

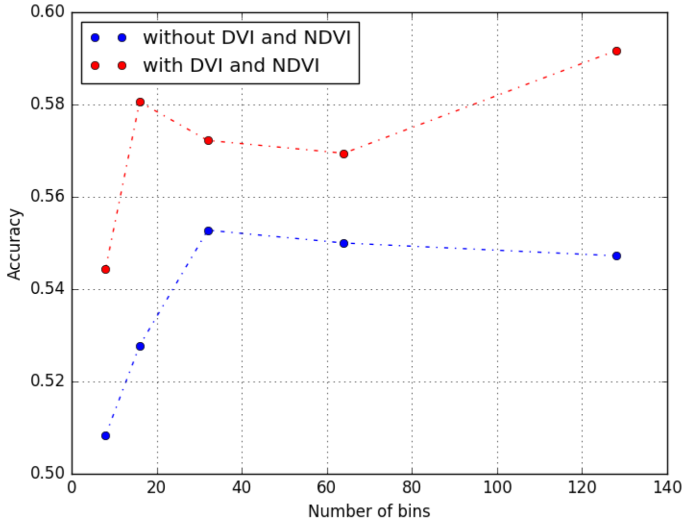

Figure 5.7: Comparing accuracies of treatment classification with or without band difference between Red and NIR.

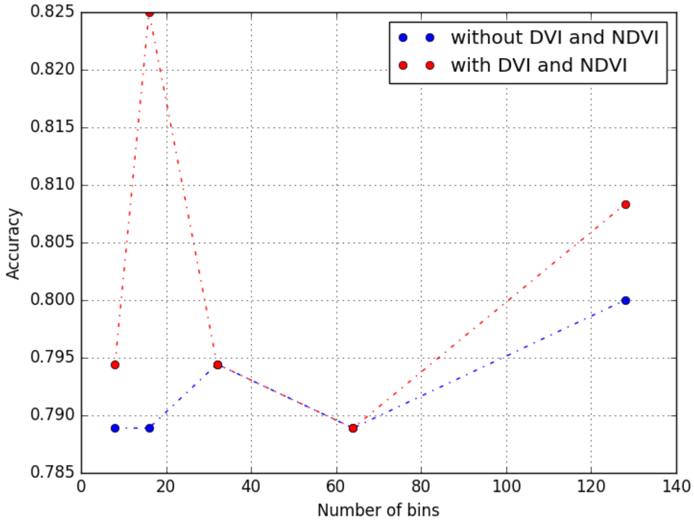

Figure 5.8: Comparing accuracies of variety classification with or without band difference between Red and NIR.

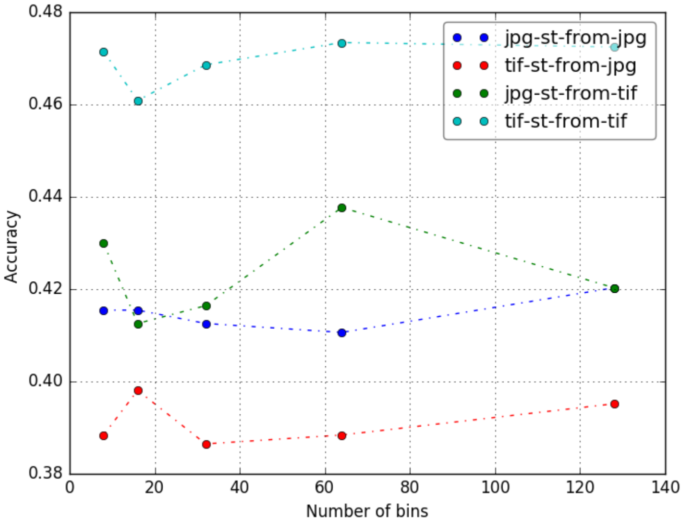

Figure 5.9: Comparing accuracies of treatment classification using images of different formats.

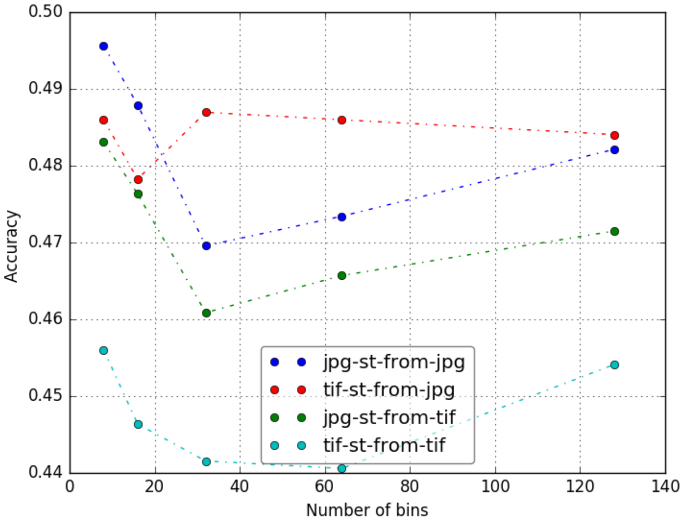

Figure 5.10: Comparing accuracies of variety classification using images of different formats.

be explored. More specifically, these four formats are an orthomosaic JPG image stitched from individual JPG images, an orthomosaic JPG image stitched from individual TIF images, an orthomosaic TIF image stitched from individual JPG images and an orthomosaic TIF image stitched from individual TIF images. For abbreviation, these four formats are denoted as jpg-st-from-jpg, jpg-st-from-tif, tif-st-from-jpg, and tif-st-from-tif.

The images used for this experiment are collected with the RGB camera (Survey 2, MAPIR, USA) and the NIR camera (Survey 2, MAPIR, USA) at 120 m, with the spatial resolution of 4.06 cm/pixel. These images are made in the four different formats and registered band to band. For each format, difference and normalized difference are calculated using the NIR band and the red band from the NIR camera (Survey 2, MAPIR, USA). Therefore, four images with 7 layers of four different formats are used as input for the classifiers.

Classification accuracies of treatments are shown in Fig. 5.9 and accuracies of variety in Fig. 5.10. The format of tif-st-from-tif performs best for treatment classification, and it is 6% better than the other formats, indicating that conversion in JPG does lose treatment related information. On the other hand, the format jpg-st-from-jpg introduces the best results for variety classification. The reason might be that JPG helps filter some noise that is not related to variety classification.

These results show that the proposed methods are able to extract more information as shown in the treatment classification. However, loss conversion sometimes might help filter some unwanted noise with regard to the target application.

5.4 Chapter Summary

In this Chapter, effects of some remote sensing related factors are evaluated in irrigation treatment classification and variety classification, with the best model in Chapter 4. These factors are spatial resolution, spectral configuration, band-to-band registration and image formats.

Based on the above experiments, the key contributions in this Chapter are as follows.

- Higher spatial resolution increases the accuracy of variety classification, but reduces the accuracy of irrigation treatment.
- More spectral bands, in particular TIR, can increase irrigation treatment classification accuracy, but do not introduce benefits in variety classification.
- Difference and normalized difference help improve classification performance of both varieties and treatments, although slightly better accuracy is obtained for variety classification. This indicates that for some application, it might not be necessary to do band-to-band registration in the pixel level to obtain band difference and normalized difference.

- Using TIF images in the whole process helps achieve better treatment classification, whereas noise is better filtered using JPG images to introduce higher accuracy of variety classification.

It is shown that for a given application, adding more information either in spectral domain or spatial domain does not necessarily increase the classification performance. One reason might be that it becomes harder to find the optimal parameters for ANN models when more features are added for each sample but the number of samples in the dataset is kept the same. The other explanation might be that more features introduce both application related information and noise at the same time. When there is no better feature extraction methods or noise filters applied, more features may not deliver better results.

Implications of these contribution to UAV-based remote sensing suggest that spatial resolution, spectral configuration, band-to-band registration and image formats all matter. It is always good to start with higher dimension data collection, i.e., higher spatial resolution, more spectral bands, higher accuracy of georeferencing and raw images, and then to conduct routine flight mission with optimized setting according to the target application.

Chapter 6

WATER STRESS MONITORING OF ALMOND TREES

6.1 Introduction

In Chapters 4 and 5, UAV-based remote sensing is used to infer irrigation treatments. It is helpful to detect trees that are under different irrigation treatments, either over irrigated or under irrigated during a long term. However, it is more desired to obtain real-time water stress monitoring of almond trees. Then farm managers can optimize irrigation schedules more frequently to minimize stress of almond trees and thus maximize the productivity.

As one of the popular water stress indicators, SWP has been proved to be a standard method for real-time water status monitoring, able to provide a short-time or medium-term plant response to water stress. Quite a few studies have been conducted on the correlation between SWP and vegetation indices in different species of crops using UAV based remote sensing. Crop water stress index (CWSI) showed a good correlation with SWP in peach trees [74], pistachio trees [75] and almond trees [76]. PRI was correlated well with SWP in olive trees [213] and significant correlation was found between PRI and CWSI in vineyards [214]. NDVI was correlated well with SWP in mandarin citrus trees [173]. Non-normalized NDVI showed a good correlation with SWP in almond trees [215]. Although the image spatial resolutions and camera band configurations in these studies were different, all these vegetation indices were obtained by averaging the pixel DN values or vegetation indices in the scales of canopies [85] or blocks.

This Chapter discusses how the proposed methodology in Chapter 4 can help improve prediction of SWP by using high resolution multispectral images. For the regression problem of SWP prediction, each pixel DN value in a spectral band or a format of vegetation indices is considered as an individual variable for the tree. Various methods are researched to explore the benefits of these high dimension pixels or variables to accurate SWP prediction. Considering relatively small SWP measurement dataset, only linear regression models are explored to minimize the prediction variance.

Section 6.2 describes data collection and preprocessing, a brief introduction about BRDF, linear model regression, regulation and dimensionality reduction in liner regression. Section 6.3.1 describes how NDVI means and variances change according to view angles. SWP regression using statistics moments is presented in

Section 6.3.2, where different linear regression methods are compared with regard to mean square error (MSE). Section 6.3.3 introduces SWP regression using canopy histograms and MSE of models with different bin sizes of histograms is discussed. Finally, all these linear regression models are compared in Section 6.4.

6.2 Materials and Methods

6.2.1 Data Collection

Midday stem water potential (SWP) was measured to monitor the plants water status using a pressure chamber (PMS Instrument Model 600, USA) following standard procedures [216]. The locations of sample trees are shown in Fig. 3.1, where each cell stands for a tree and the sample tree is marked in red. In 2015, three sample trees in the middle line of each plot were measured, hence there were fifteen measurements in each block. SWP measurements for the middle block, the west block, and the east block were rotated weekly. SWP measurements of 06/12/15, 06/18/15, 07/16/15, 08/20/15, 09/10/15 are used for regression analysis.

The modified NIR camera (ELP110HS, Canon, Japan) was flown at the same time of SWP measurement with the spatial resolution of 1.87 cm/pixel at 60 m AGL. The modified NIR camera contains three bands, NIR, green and blue. More detail of its specification is listed in Tab. 3.1 and Fig. 3.3. RAW images are captured during flights, and converted to TIF images for stitching in Photoscan (Agisoft, Russia). Canopy images of samples trees are cropped manually from the most nadir individual TIF image with the help of the stitched orthomosaic image. Both original and cropped canopy images of a sample tree are shown in Fig.6.1(a) and 6.1(b), where surrounding non-canopy pixels are filtered.

6.2.2 Data Pre-processing

Besides three bands NIR, green and blue provided in the camera, two more layers are added in the image array. One layer is difference between the NIR band and the blue band, as described in Equ. 6.1, where DN_{NIR} and DN_{blue} stand for digital value for a pixel. The other layer is normalized difference, in the format of Equ. 6.2, where pixels with zero sum of DN_{NIR} and DN_{blue} are filtered out. Therefore canopy images of five layers serve as input for later regression analysis. It needs to be noted that DN values are used instead of reflectance. This is reasonable because later regression is studied for measurements within one day rather than across days.

$$DVI = DN_{NIR} - DN_{blue} \tag{6.1}$$

$$NDVI = \frac{DN_{NIR} - DN_{blue}}{DN_{NIR} + DN_{blue}}. \tag{6.2}$$

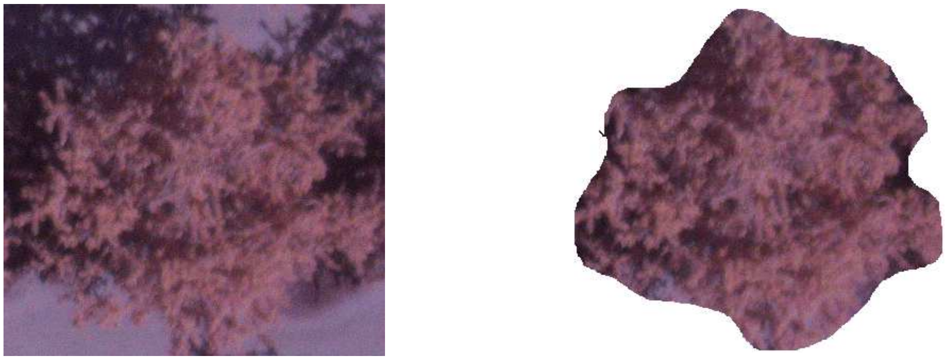

(a) (b)

Figure 6.1: A sample tree canopy before (a) and after cropped (b).

6.2.3 Linear Regression

The most popular regression method is simple linear regression. It predicts a quantitative response Y with regard to a single predictor variable X,

$$Y = \beta_0 + \beta_1 X + \epsilon, \tag{6.3}$$

where β_0 and β_1 represent the intercept and slope in the line model respectively, ϵ is the error term.

Given n observation points,

$$(x_1, y_1), (x_2, y_2), ..., (x_n, y_n)$$

define the residual sum of squares (RSS) as

$$\begin{aligned} RSS &= e_1^2 + e_2^2 + ... + +e_n^2, \\ e_i &= y_i - \widehat{\beta_0} - \widehat{\beta_1} x_1, i = 1, 2, ..., n, \end{aligned} \tag{6.4}$$

where $\widehat{\cdot}$ is used to denote an estimated value. Then $\widehat{\beta_0}$ and $\widehat{\beta_1}$ can be obtained by minimizing the RSS using the least squares approach,

$$\begin{aligned} \widehat{\beta_1} &= \frac{\sum_{i=1}^{n}(x_i - \overline{x})(y_i - \overline{y})}{\sum_{i=1}^{n}(x_i - \overline{x})^2}, \\ \widehat{\beta_0} &= \overline{y} - \widehat{\beta_1}\overline{x}, \end{aligned} \tag{6.5}$$

where

$$\begin{aligned}\overline{y} &= \frac{1}{n}\sum_{i=1}^{n} y_i, \\ \overline{x} &= \frac{1}{n}\sum_{i=1}^{n} x_i.\end{aligned} \tag{6.6}$$

When there are more than one predictors, instead of creating many simple linear regression models separately, multiple linear regression model can be used,

$$Y = \beta_0 + \beta_1 X_1 + \beta_2 X_2 ... + \beta_p X_p + \epsilon, \tag{6.7}$$

where X_i denotes the ith predictor and β_i the coefficients associated with that predictor, p is the number of predictors, and ϵ is the error term. Similarly, these coefficients $\beta_i, i = 1, 2, ..., p$ can be estimated by minimizing the RSS using the multiple least squares approach.

One of the most popular statistics to compare linear regression models is MSE defined as

$$MSE = \frac{1}{n}\sum_{i=1}^{n}(y_i - \hat{y}_i)^2. \tag{6.8}$$

6.2.4 Liner Model Regularization

When the number of predictors is grater than the number of observations, the least squares method becomes unstable. There are no longer unique least squares coefficients and the variance of these coefficients become infinite. To overcome this issue, three classes of methods are usually used, subset selection, shrinkage and dimensionality reduction [217].

6.2.4.1 Subset Selection

One method of subset selection is best subset selection. In best subset selection, 2^p models will be evaluated and the best model is selected according to Akaike information criterion (AIC), Bayesian information criterion (BIC) or adjusted R^2. The other method is stepwise regression. It adds or removes the variable one at a time according to the statistical significance. Different from best subset selection [217], stepwise regression does not search through all the possible subsets. But stepwise regression can save the computation a lot when p is large. It usually has a lower variance due to the more constrained search.

6.2.4.2 Shrinkage Methods

Two popular methods to shrink the regression coefficients are ridge regression and least absolute shrinkage and selection operator (LASSO) regression [217]. Ridge regression estimates the coefficients by minimizing the cost with ℓ_2 of coefficients,

$$\sum_{i=1}^{n}(y_i - \beta_0 - \sum_{i=1}^{p} \beta j x_{ij})^2 + \lambda \sum_{i=1}^{p} \beta_i^2, \tag{6.9}$$

where $\lambda \geq 0$ is a parameter for tuning the penalty on the coefficients β. Similarly, LASSO regression adds the penalty ℓ_1 of coefficients in the cost

$$\sum_{i=1}^{n}(y_i - \beta_0 - \sum_{i=1}^{p} \beta_j x_{ij})^2 + \lambda \sum_{i=1}^{p} |\beta_i|. \tag{6.10}$$

When the penalty grows with increasing λ, it will make the coefficients approach zero and less predictors will show up in the models.

6.2.4.3 Dimensionality Reduction Methods

In either subset selection, ridge regression or LASSO regression, original predictors are used in the regression model. Another approaches of model regularization transform predictors first and build the model with the transformed variables. These approaches are denoted as dimensionality reduction based methods [217].

The first dimensionality reduction method is principal component regression. In principal component regression (PCR), the first $M (M \ll p)$ principal components are extracted using PCA, and a linear regress model is fitted using these components. PCR can help avoid multicollinearity significantly, because these principal components are uncorrelated. When the assumption of PCR is true, that the predictors show the most variation in the directions associated with Y, it can reduce the coefficients to be estimated and hence reduces the risk of overfitting.

PCA is an unsupervised method, so PCR does not include information of the response while extracting the transformed components. Consequently, the directions representing the best variations of the predictors may not be the best directions to predict the response. Unlike PCR, the partial least squares (PLS) method finds the new features in a supervised way. PLS identifies the directions that can explain both the response and the predictors [218].

In both PCR and PLS, the number of M is chosen by cross-validation. The predictors and the responses are usually standardized before feature extraction.

6.3 Results and Discussion

6.3.1 Effects of View Angles on Canopy Vegetation Indices

It is well known that remote sensing measurement depends on both illuminating angles and view angles. Disturbance of illuminating angles can be minimized

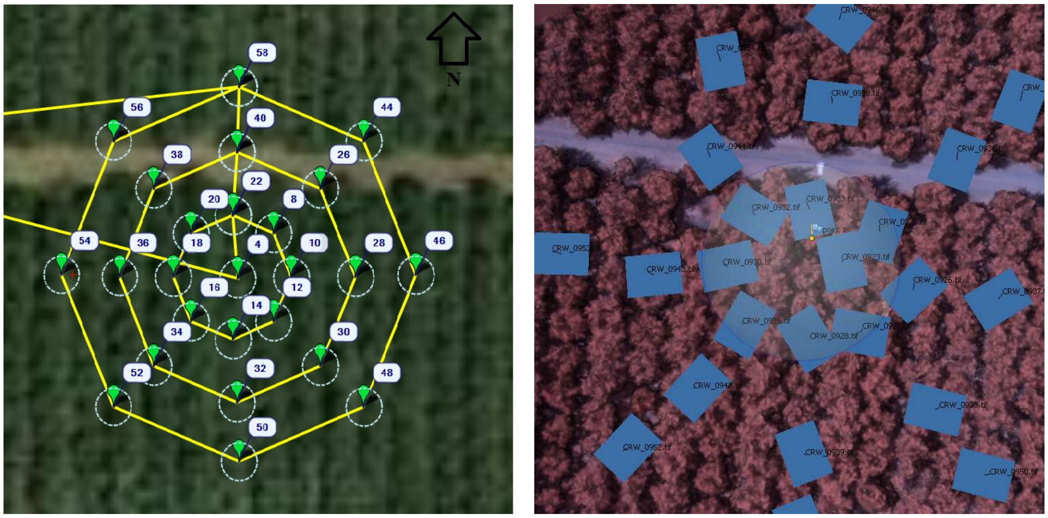

(a) Flight path in Mission Planner

(b) Collected images overlayed on the stitched image

Figure 6.2: Flight path and collected images of the circle mission.

Table 6.1: Specification of the circle mission

Zenith angle	30°
Azimuth angle	−111.95°
Altitude	120 m
Longitude	120.638 78°W
Latitude	37.495 104°N
Time (USA Pacific)	15:00

by finishing flight mission within a short time window. However, faster mapping usually requires larger overlap, so the target area can be covered with less flight paths. This leads to larger variations in view angles. Many simulations studies have been published about how vegetation indices such as NDVI changes with the illuminating angles or view angles [219, 220]. In this Section, a circular flight mission is designed to research how the view angles affect vegetation index NDVI.

A circle mission was conducted at 60 m in the west block, on June 4th, 2015. Detailed information about mission location and the solar angle is in Tab. 6.1. As shown in Fig. 6.2(a), the images were taken right above the tree, and eight points along each circles. The radiuses of the circles are 10 m, 20 m and 30 m respectively. The starting waypoint on the circle lies on the north of the target tree. The second tree in the row is chosen to avoid the border effects of sunlight. A white target is put on the road aligned with the sample row. The images are

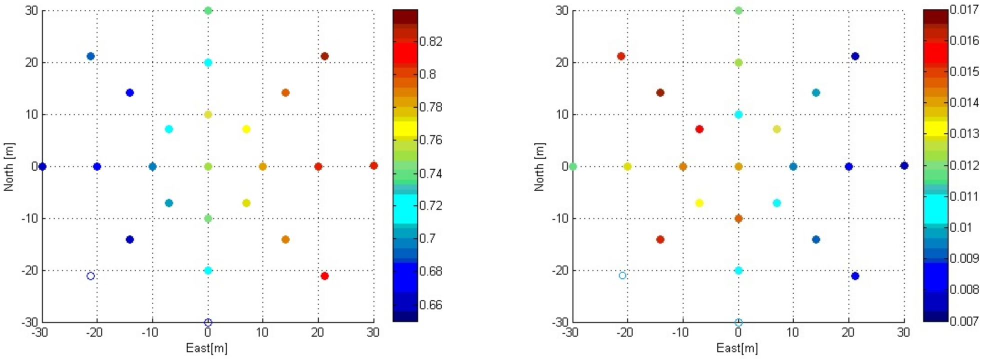

(a) (b)

Figure 6.3: (a) Canopy NDVI means under different view angles, (b) Canopy NDVI variances under different view angles.

stitched in Photoscan(Agisoft, Russia) first and a marker is placed on the target tree (Fig. 6.2(b)). According to the marker, the sample tree is cropped from each frame (Fig. 6.1(a)). Then the soil is cropped out and only the remaining canopy pixels (Fig. 6.1(b)) are used to calculate the canopy NDVI mean.

The distributions of canopy NDVI mean and variance are shown in Fig. 6.3(a) and Fig. 6.3(b), with the right side referring east, the up side north. The sample tree is not captured in two images, and these two images were marked with the hollow points. The hotspot appeared when the camera was on the southwest side of the tree, where the view angle was the same as the illumination angle (azimuth angle) of $-111.95°$ with regard to north, $60.35°$ measured from the horizontal. In the solar principle plane, canopy NDVI means become less when view angles get closer to the illumination angle and they become larger when the view angles move further from the illumination angle. The absolute error between the maximum and minimum is up to 0.16, 24% with regard to the lowest value 0.66. Therefore, it is necessary to conduct calibration to reduce the influence of view angles on canopy NDVI to infer SWP.

6.3.2 Water Stress Monitoring Using Descriptive Statistics

Studies using means, variances or higher order moments to monitor plant health have been published, where different order moments were applied to canopy temperature [76, 221, 222] or vegetation indices such as DVI [223, 224], NDVI, GDVI and SAVI [225].

Following the methodology proposed in Chapter 4, moments can be considered as a dimensionality reduction method to extract information from the tree

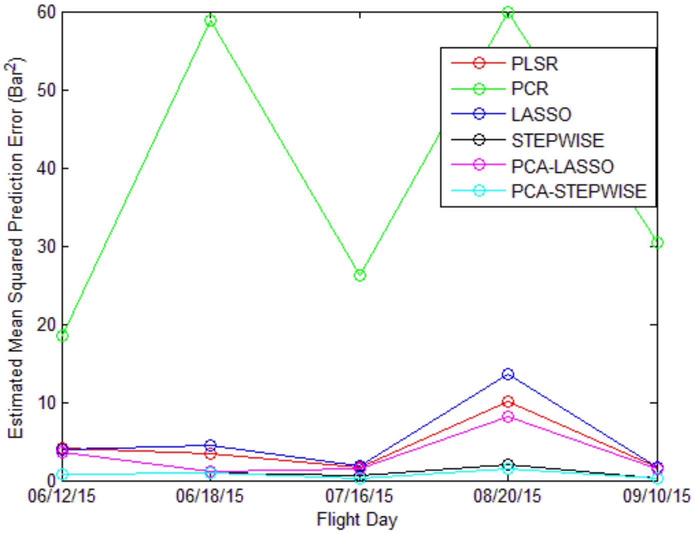

Figure 6.4: Comparing MSE of models using PLS, PCR, stepwise, LASSO, PCA plus stepwise, PCA plus LASSO based on means.

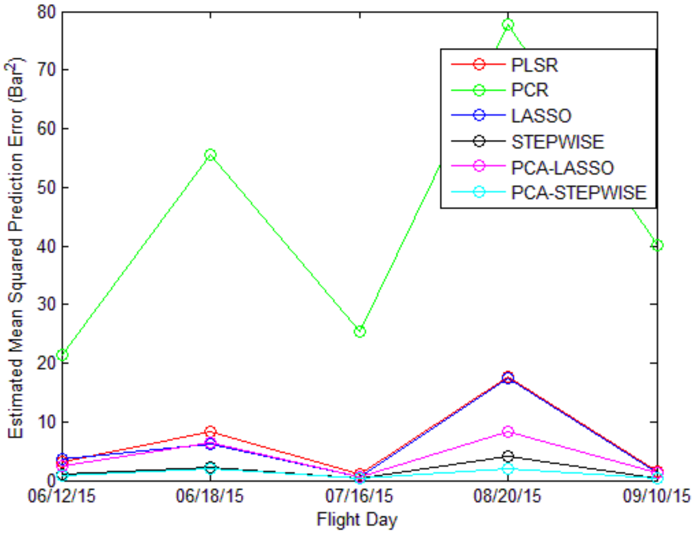

Figure 6.5: Comparing MSE of models using PLS, PCR, stepwise, LASSO, PCA plus stepwise, PCA plus LASSO based on means and variancse.

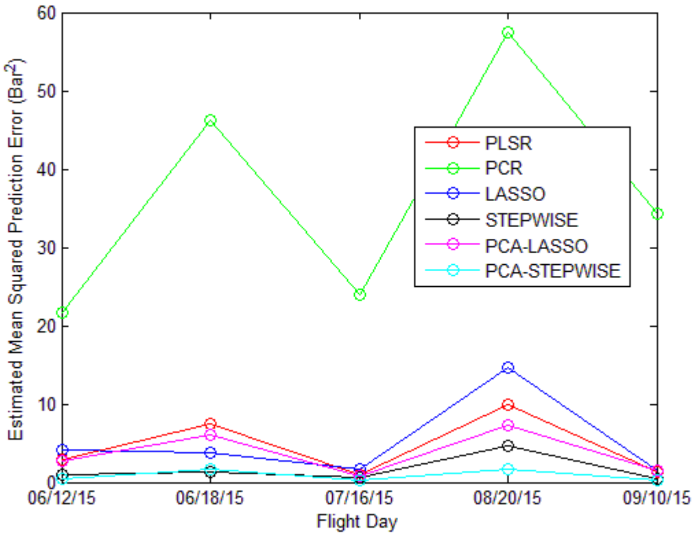

Figure 6.6: Comparing MSE of models using PLS, PCR, stepwise, LASSO, PCA plus stepwise, PCA plus LASSO based on means, variances and skewness.

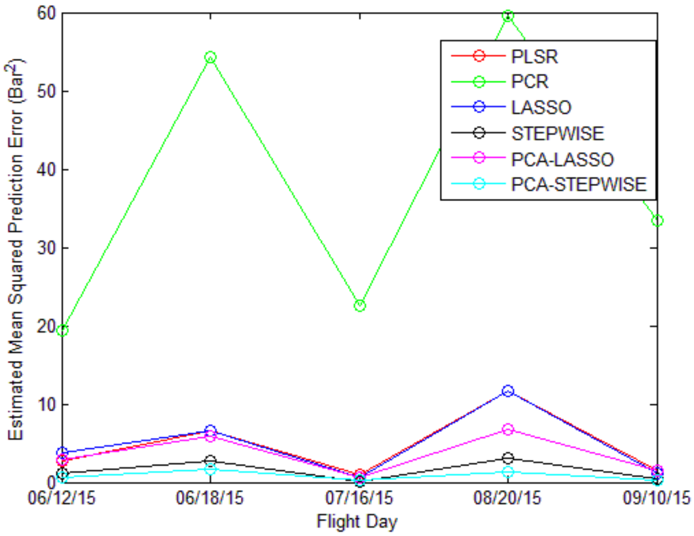

Figure 6.7: Comparing MSE of models using PLS, PCR, stepwise, LASSO, PCA plus stepwise, PCA plus LASSO based on means, variances, skewness and kurtosis.

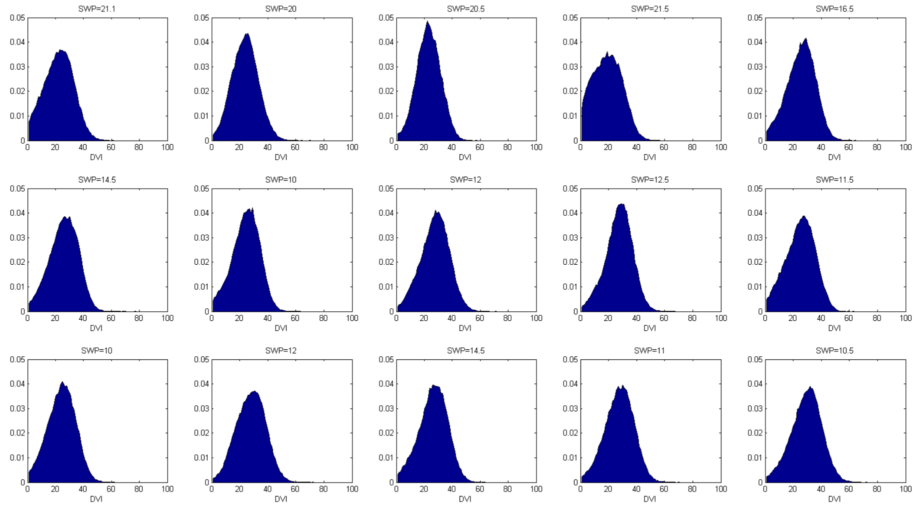

Figure 6.8: SWP values and histograms of pixel difference between the NIR band and the blue band for 15 samples using images collected on 08/20/15.

canopy pixel distributions. Therefore, moments can be applied not only to temperature, to vegetation indices, but also to each band of the images.

The first problem of extracting moments for each band is that too many variables are introduced for the regression model. This is particularly bad when there are only limited samples available. What is worse, as unsupervised methods, extracted moments do not necessarily correlate well with the predictor. To solve these two problems, regulation methods and dimensionality reduction methods are used before these moments are fed to the regression model.

In this Section, four different groups of moment combination are explored, including means, means and variances, means, variances and skewness, means, variances, skewness and kurtosis. Because the orthomosaic image contains 5 layers of NIR, green, blue, difference between the NIR band and the blue band, normalized difference between the NIR band and the blue band, the observation dimensions of each tree are 5, 10, 15 and 20 for different moment combinations, respectively.

Six different strategies of regularization or dimensionality reduction are used to build the regression model. Four separate strategies are partial least squares regression (PLSR), PCR, LASSO and stepwise, where moments are fed directly to regression models. The other two mixed methods are PCA plus LASSO, PCA plus stepwise, where extracted principal components from moments serve as input to LASSO or stepwise models.

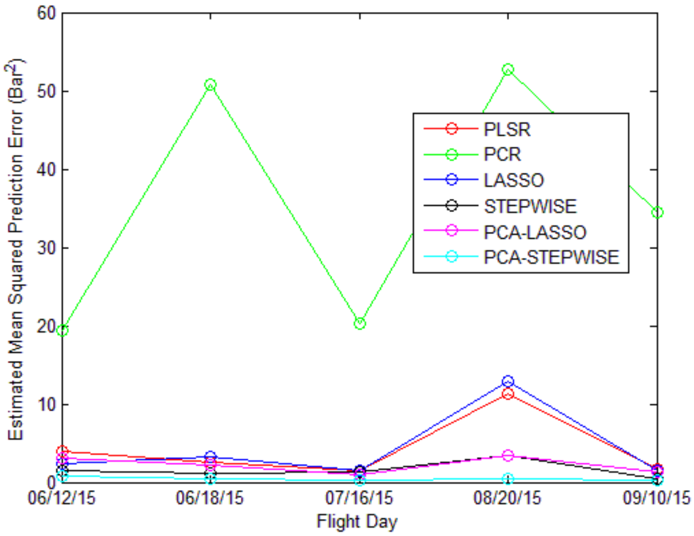

Figure 6.9: Comparing MSE of models using PLS, PCR, stepwise, LASSO, PCA plus stepwise, PCA plus LASSO based on histograms of 16 bins.

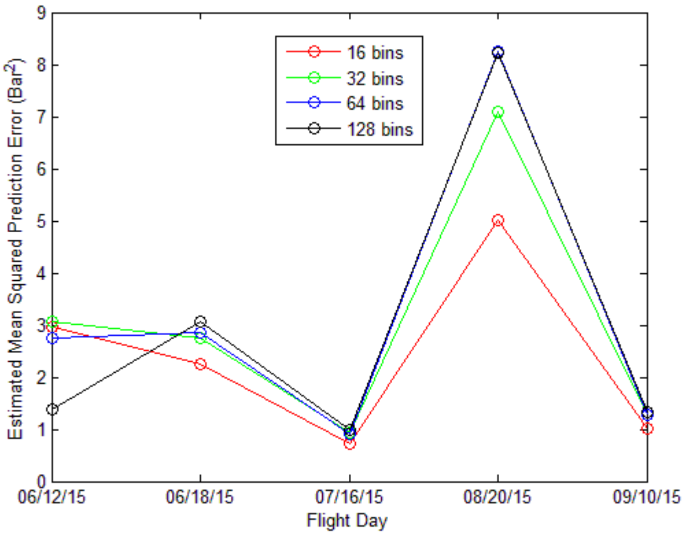

Figure 6.10: Comparing MSE of models using PCA plus LASSO based on histograms of 16, 32, 64, 128 bins.

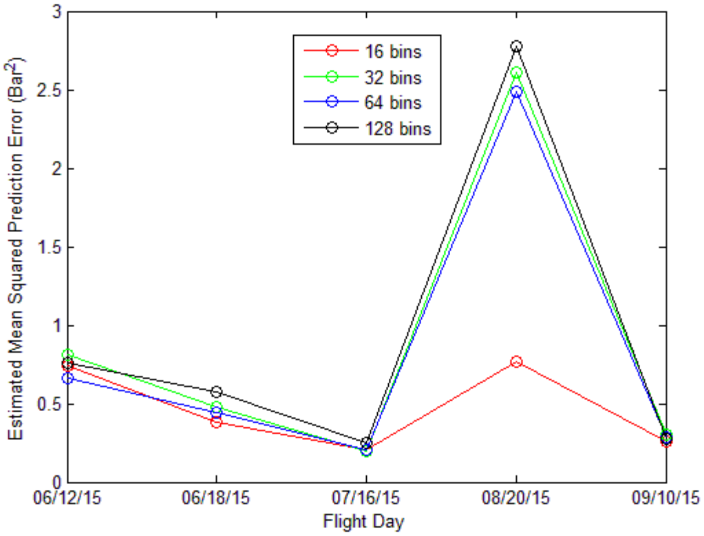

Figure 6.11: Comparing MSE of models using PCA plus stepwise based on histograms of 16, 32, 64, 128 bins.

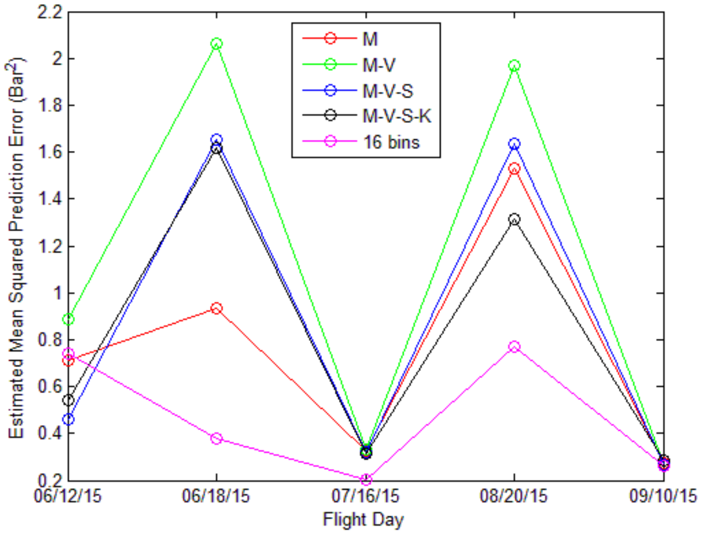

Figure 6.12: Comparing MSE of models using PCA plus stepwise based on both moments and histograms.

These models are compared based on five days' measurements, which include 75 measurements in total. The models are built for each day with 15 measurements and compared according to MSE. MSE is calculated via 5-fold cross-validation. The number of components extracted in PLSR and PCA related models is determined using cross-validation. All these models are implemented using libraries in Matlab2013b (Mathworks, USA).

Results of these models with different moment combinations are shown in Fig. 6.4, 6.5, 6.6, and 6.7. As for the regression strategies, stepwise performs consistently better than LASSO and PLSR. PCR is the worst. The performances of LASSO and PLSR depend on the dataset. For example, the MSE is small on the dataset of 07/16/15, but very large on the dataset of 08/20/15. In addition, stepwise models using principal components are better than the models based on direct moments, indicating that PCA can extract response related information and filter some unwanted noise.

MSE of stepwise models using PCA with different moment combinations are compared in Fig. 6.12. The results show that adding more moments to the models does not necessarily help increase the model performance. For example, on the dataset of 06/18/15, means based models are better than the models using more moment features. It also indicates that variances might not be good features for SWP regression, as adding variances in the models decreases MSE consistently.

6.3.3 Water Stress Monitoring Using Histograms

Similar to Section 4.3.2, because moments are the methods to describe canopy pixel distributions, histograms could provide a complete description about canopy pixel digital values. As an example, Fig.6.8 shows SWP values and the histograms of canopy pixel DN values of 15 sample trees in the middle block, where x axis represents difference between the NIR band and the blue band of the modified NIR camera (ELPH110HS, Canon, Japan), y axis is the percentage of the pixels with a certain DN value, and SWP values are on the top. Besides features captured by moments such as spread and skewness, other information of histograms might be filtered out, i.e. the shape of tails or tops. Therefore, instead of using moments for dimensionality reduction, it is promising that feeding histograms of canopy pixel DN values directly as the regression input could improve the regression performance.

Figure 6.9 compares six different regression strategies using histograms of 16 bins. The orthomosaic used for histograms based regression is the same as the one for moments based regression, which includes 5 layers. When the histograms are described with 16 bins, a feature vector for each tree will be 80 dimensions. It shows that stepwise with PCA is also the best for histograms based regression. Figure 6.10 and 6.11 show the results of LASSO with PCA, and stepwise with PCA fed with histograms of different bin sizes, where both indicate that histograms of 16 bins yield the consistently best model.

Finally, results of stepwise with PCA using histograms are compared with those of stepwise with PCA using moments in Fig. 6.12. It proves that histograms based models can extract more SWP related information and produce better SWP regression performances in terms of MSE.

In Fig. 6.9, it is also shown that there are day-to-day changes of MSE for both histogram-based regression and moment-based regression. For example, the MSE in 07/16/15 and 09/16/15 are small and the MSE in the other days are large. This variation might come from different crop dynamics during different growing stages or under different environment conditions. The variation might also be caused by SWP measurements. In our study, only one SWP measurement is taken for each sample tree by one technician. This practice usually introduces a significant measurement noise [226]. This might explain that PLSR, a supervised regression method, is not performing as well as the unsupervised regression methods, e.g., stepwise regression and LASSO regression.

6.4 Chapter Summary

A regression problem of predicting SWP using tree canopy pixel DN values is discussed in this Chapter. The key contributions of this Chapter are as follows.

- A circular flight mission is designed to study how view angles affect canopy NDVI means and variances. Different regression regularization methods are evaluated as well, Experiments shows that over 20% of canopy NDVI means could be introduced by view angles.

- Regression models using moments of tree canopy pixel DN values are compared in terms of SWP MSE. Six different regression regularization methods are evaluated as well, including PLSR, PCR, LASSO, stepwise, LASSO with PCA and stepwise with PCA. Results indicate that higher order moments can help produce better models sometimes, but the performance increase is not consistently. Out of these six regularization methods, stepwise with PCA yields the best performance consistently in all the datasets.

- Regression models using histograms of tree canopy pixel DN values are compared in terms of SWP MSE. Different regularization methods and bin sizes of histograms are studied as well. It is revealed that stepwise with PCA and histograms of 16 bins produce the best performance consistently across all the datasets.

- Comparing moment based models to histogram based models shows that histograms based model can provide consistently better models in terms of MSE.

Based on the above contributions, implications of these contributions to UAV based remote sensing in precision agriculture are listed as follows.

- View angles can introduce significant amount of noise to remote sensing measurements. In order to obtain consistent and precision measurements, it is necessary to take special care of view angles during flight mission planing and image collection.

- High resolution images not only provide a better capability to differentiate objects, but also contribute extra measurement dimensions about the objects. New types feature description and feature extraction methods are necessary to obtain extra benefits from these high resolution images. For example, in the application of almond tree SWP prediction, canopy description using histograms and regression using regularization methods PCA and subset selection can yield the best regression performance.

Chapter 7

SUMMARY AND FUTURE WORK

7.1 Summary

The development of UAVs and imaging sensor technologies makes it much easier to collect images with very high spatial resolution and even spectral resolution. It becomes possible to monitor crop health in the level of a single plant. However, there is lack of a workflow to make the best use of high resolution images for plant health monitoring. With almond tree water stress monitoring as a case study, this dissertation examines the whole process of remote sensing using UAVs, and three key parts are discussed throughout the forgoing Chapters, region of interest extraction, classification using high resolution images, and regression using high resolution images.

The first step for information extraction in high resolution images is to extract region of interest, or object segmentation. Chapter 3 proposes two types of methods for tree canopy segmentation. The first one is based on manual features such as color, textures and morphological features. The second is using deep learning based instance-segmentation. Instead of relying on many manual features and parameters, deep learning based segmentation provides a robust end-to-end solution for canopy segmentation. Chapter 4 addresses a problem of irrigation treatment classification using high resolution canopy images. Rather than traditional methods using mean vegetation indices, three methods are proposed to leverage the benefits of high dimensions of UAV-based high resolution images, moments based classifiers, histograms based classifiers and distance based classifiers. In Chapter 5, the best model developed in Chapter 4, that is based on histograms and ANN, is applied in two classification tasks of almond variety classification and irrigation treatment classification to the evaluate the effects of various factors involved in UAV based remote sensing on classification accuracy. These factors include spatial resolution, spectral configuration, band-to-band registration and image formats. Chapter 6 discusses a regression problem of predicting almond tree water stress via SWP using high resolution images. A circular flight mission is conducted to explore the effects of view angles on canopy NDVI means and variances. Then two feature extraction methods and six regression strategies are explored to predict SWP, where two extraction methods are the one using moments and the one using histograms, and six linear regression strategies include stepwise, PLSR, PCR, LASSO, stepwise with PCA and LASSO with PCA.

7.2 Future Work

The workflow of extracting plant health information using UAV-based remote sensing is far from being mature. The benefits from high resolution images are demonstrated but more challenges are coming along with these new opportunities.

7.2.1 Region of Interest Extraction

In Chapter 3, deep learning based instance-segmentation achieves a great success in almond tree canopy extraction, where canopy images of different lighting conditions and different growing stages are correctly segmented. However, this model only works in the images with the spatial resolution of 1.87 cm/pixel collected with the modified NIR camera (ELPH110HS, Canon, Japan). It does not work on the images with different bands, or different spatial resolution. According to current practice, to make it work in other situations, specific datasets in those situations need to be collected and a brand new model needs to be trained. In summary, more work is needed to minimize the data collection and labelling effort and to maximize its generalization for images of various spatial resolution, spectral configuration and plant species. Another issue is about the speed. Even just for inference, deep learning based algorithms need GPU to accelerate the computation. Ideally, field management needs real-time crop monitoring for decision making. It might help by running all these segmentations in the cloud, but then it requires that the onboard cameras have good access to the internet. A more promising solution is to run inferences in the edge devices, which not only releases communication load but also speeds up the processing.

7.2.2 Optimization of Model Parameters and Remote Sensing Settings

As shown in Chapters 4, 5 and 6, to design either a classifier or a regression model using UAV-based remote sensing images, many model parameters and data collection or preprocessing settings are involved. Examples of these parameters are bin sizes of histograms, the number of hidden layers and the number of components extracted in PCA. Examples of data collection settings are flight altitude, camera band configuration and image formats. Current practices are based on many experiments to grid search these best parameters and settings. However, these parameters or settings are application dependent, which means a new group of parameters or settings needs to be determined for each new application. It becomes very hard to develop classification models for many different applications. As a result, all the efforts in developing models are disconnected among different applications, rather than accumulated with one application by another application. In some time critical remote applications, i.e., monitoring the crops within a short growing windows, limited number of experiments are available to explore the optimal settings. Therefore, what is the right way to continue optimizing model parameters and remote sensing settings based on existing dataset and knowledge needs further research.

7.2.3 Minimizing the BRDF Effects

Chapter 6 discusses how BRDF affects canopy NDVI means, indicating that view angles will introduce significant disturbances for remote sensing based measurements. In real-world remote sensing applications, it is very hard to make sure all the observations of objects are under the same view angles and the same illuminating angles. It is hard to collect consistent remote sensing measurements, which adds large amount of uncertainties to the analysis results. Due to this inconsistency, only SWP measurements within a day are used to build the regression model to minimize the disturbances from solar angles between different days. Therefore, it is desired to research either the calibration method to minimize the inconsistency, or regression or classification models that are robust to these disturbances.

7.2.4 Development of Models Robust and Sensitive to Crop Changes

Besides the disturbance of BRDF effects, other big challenges are from the crops. Unlike man-made objects, the crops grow all the time. They adjust themselves in realtime according to water, soil nutrients, sun light and other environmental conditions. How to design the models both robust and sensitive to crop changes needs further exploration. For example, is the SWP prediction model for almond trees in June the same as the model in July? Is the SWP model for almond trees in Merced the same as the model for almond trees in Davis? More datasets are necessary to answer these questions.

BIBLIOGRAPHY

[1] F. Gassert, One-quarter of world's agriculture grows in highly water-stressed areas, `http://www.wri.org/blog/2013/10/one-quarter-world%E2%80%99s-agriculture-grows-highly-water-stressed-areas` (2013).

[2] Clarity from above, `https://www.pwc.pl/clarityfromabove` (2016).

[3] Llewellyn Data Processing, Camera technical description, `https://maxmax.com/RemoteSensingcamerasi.htm`.

[4] MAPIR, Camera parameters for flight management software, `https://www.mapir.camera/collections/survey2/products/survey2-camera-ndvi-red-nir`.

[5] TNAU, Agritech Portal, Role of water for growth and development of crops, `http://agritech.tnau.ac.in/agriculture/agri_irrigationmgt_roleofwater.html` (2016).

[6] S. Datko, What is plant transpiration?, `http://sdhydroponics.com/2012/05/30/what-is-plant-transpiration/` (2012).

[7] K. Roberts, Handbook of Plant Science, Vol. 1, Wiley-Interscience, 2007.

[8] V. Enne, How do plants use water in photosynthesis?, `https://sciencing.com/do-plants-use-water-photosynthesis-5513808.html` (2017).

[9] C. Van Leeuwen, O. Tregoat, X. Choné, B. Bois, D. Pernet, J.-P. Gaudillère, et al., Vine water status is a key factor in grape ripening and vintage quality for red Bordeaux wine. how can it be assessed for vineyard management purposes, J. Int. Sci. Vigne Vin 43 (3) (2009) 121–134.

[10] R. Slayter, Plant-Water Relationships, London and New York: Academic Press, 1967.

[11] T. Hsiao, E. Fereres, E. Acevedo, D. Henderson, Water stress and dynamics of growth and yield of crop plants, in: Water and Plant Life, Springer, 1976, pp. 281–305.

[12] S. Armstrong, How does water affect plant growth?, `https://www.gardeningknowhow.com/special/children/how-does-water-affect-plant-growth.htm` (2018).

[13] J. Castel, E. Fereres, Responses of young almond trees to two drought periods in the field, Journal of Horticultural Science 57 (2) (1982) 175–187.

[14] E. Fereres, D. Goldhamer, Deciduous fruit and nut trees, Agronomy (USA)(1990).

[15] S. J. Hake, T. Kerby, K. Hake, et al., Cotton production manual, Vol. 3352, University of California, Agriculture and Natural Resources, 1996.

[16] W. Micke, Almond production manual, University of California, Division of Agriculture and Natural Resources, 1996.

[17] World Economic Forum, Global Risks 2015, Geneva,Switzerland, 2015 (2015).

[18] M. M. Mekonnen, A. Y. Hoekstra, Four billion people facing severe water scarcity, Science Advances 2 (2) (2016) e1500323.

[19] Stateline, Drought returns to huge swaths of U.S., raising fears of shortages, `http://www.governing.com/topics/transportation-infrastructure/sl-drought-water-shortage.html`.

[20] D. Wyatt, 63% of California in drought, `https://www.mantecabulletin.com/news/local-news/63-california-drought/`.

[21] World Bank Group, Water in agriculture, `http://www.worldbank.org/en/topic/water-in-agriculture` (2017).

[22] W. J. Davies, M. J. Bennett, Achieving more crop per drop, Nat. Plants 1 (15118) (2015) 10–1038.

[23] M. W. Rosegrant, J. Koo, N. Cenacchi, C. Ringler, R. D. Robertson, M. Fisher, C. M. Cox, K. Garrett, N. D. Perez, P. Sabbagh, Food security in a world of natural resource scarcity: The role of agricultural technologies, Intl Food Policy Res Inst, 2014.

[24] T. Du, S. Kang, J. Zhang, W. J. Davies, Deficit irrigation and sustainable water-resource strategies in agriculture for China's food security, Journal of Experimental Botany 66 (8) (2015) 2253–2269.

[25] N. Zhang, M. Wang, N. Wang, Precision agriculture-a worldwide overview, Computers and Electronics in Agriculture 36 (2-3) (2002) 113–132.

[26] D. Mulla, P. Gowda, W. Koskinen, B. Khakural, G. Johnson, P. Robert, Modeling the effect of precision agriculture: pesticide losses to surface waters, ACS Publications, 2003.

[27] D. Mulla, C. Perillo, C. Cogger, A site-specific farm-scale GIS approach for reducing groundwater contamination by pesticides, Journal of Environmental Quality 25 (3) (1996) 419–425.

[28] L. Tian, Development of a sensor-based precision herbicide application system, Computers and Electronics in Agriculture 36 (2-3) (2002) 133–149.

[29] S. Park, D. Ryu, S. Fuentes, H. Chung, E. Hernández-Montes, M. O'Connell, Adaptive estimation of crop water stress in nectarine and peach orchards using high-resolution imagery from an unmanned aerial vehicle (UAV), Remote Sensing 9 (8) (2017) 828.

[30] J. V. Stafford, Implementing precision agriculture in the 21st century, Journal of Agricultural Engineering Research 76 (3) (2000) 267–275.

[31] G. Warren, G. Metternicht, Agricultural applications of high-resolution digital multispectral imagery, Photogrammetric Engineering & Remote Sensing 71 (5) (2005) 595–602.

[32] M. S. Moran, Y. Inoue, E. Barnes, Opportunities and limitations for image-based remote sensing in precision crop management, Remote Sensing of Environment 61 (3) (1997) 319–346.

[33] J.-H. Zhang, W. Ke, J. Bailey, W. Ren-Chao, Predicting nitrogen status of rice using multispectral data at canopy scale1, Pedosphere 16 (1) (2006) 108–117.

[34] J. A. Berni, P. J. Zarco-Tejada, L. Suárez, E. Fereres, Thermal and narrowband multispectral remote sensing for vegetation monitoring from an unmanned aerial vehicle, IEEE Transactions on Geoscience and Remote Sensing 47 (3) (2009) 722–738.

[35] M. F. Goodchild, D. A. Quattrochi, Scale in Remote Sensing and GIS, CRC Press, 1997.

[36] C. Anderson, 10 breakthrough technologies 2014, `https://www.technologyreview.com/lists/technologies/2014/` (2014).

[37] FAA releases aerospace forecast, `https://www.faa.gov/news/updates/?newsId=89870` (2018).

[38] K. C. Swain, H. P. Jayasuriya, V. M. Salokhe, Suitability of low-altitude remote sensing images for estimating nitrogen treatment variations in rice cropping for precision agriculture adoption, Journal of Applied Remote Sensing 1 (1) (2007) 013547.

[39] E. R. Hunt, W. D. Hively, S. J. Fujikawa, D. S. Linden, C. S. Daughtry, G. W. McCarty, Acquisition of NIR-green-blue digital photographs from unmanned aircraft for crop monitoring, Remote Sensing 2 (1) (2010) 290–305.

[40] J. Zhang, B. Basso, R. F. Price, G. Putman, G. Shuai, Estimating plant distance in maize using unmanned aerial vehicle (UAV), PloS One 13 (4) (2018) e0195223.

[41] H. Xiang, L. Tian, Method for automatic georeferencing aerial remote sensing (RS) images from an unmanned aerial vehicle (UAV) platform, Biosystems Engineering 108 (2) (2011) 104–113.

[42] J. Primicerio, S. F. Di Gennaro, E. Fiorillo, L. Genesio, E. Lugato, A. Matese, F. P. Vaccari, A flexible unmanned aerial vehicle for precision agriculture, Precision Agriculture 13 (4) (2012) 517–523.

[43] L. Johnson, S. Herwitz, B. Lobitz, S. Dunagan, Feasibility of monitoring coffee field ripeness with airborne multispectral imagery, Applied Engineering in Agriculture 20 (6) (2004) 845.

[44] D. J. Mulla, Twenty five years of remote sensing in precision agriculture: Key advances and remaining knowledge gaps, Biosystems Engineering 114 (4) (2013) 358–371.

[45] J. Flexas, J. M. Escalona, S. Evain, J. Gulías, I. Moya, C. B. Osmond, H. Medrano, Steady-state chlorophyll fluorescence (Fs) measurements as a tool to follow variations of net CO2 assimilation and stomatal conductance during water-stress in C3 plants, Physiologia Plantarum 114 (2) (2002) 231–240.

[46] J. Girona, M. Mata, J. Del Campo, A. Arbonés, E. Bartra, J. Marsal, The use of midday leaf water potential for scheduling deficit irrigation in vineyards, Irrigation Science 24 (2) (2006) 115–127.

[47] H. Düring, B. Loveys, Diurnal changes in water relations and abscisic acid in field grown Vitis vinifera cvs. I. leaf water potential components and leaf conductance under humid temperate and semiarid conditions, Vitis 21 (3) (1982) 223–232.

[48] J. M. Costa, O. M. Grant, M. M. Chaves, Thermography to explore plant–environment interactions, Journal of Experimental Botany 64 (13) (2013) 3937–3949.

[49] D. Sepúlveda-Reyes, B. Ingram, M. Bardeen, M. Zúñiga, S. Ortega-Farías, C. Poblete-Echeverría, Selecting canopy zones and thresholding approaches to assess grapevine water status by using aerial and ground-based thermal imaging, Remote Sensing 8 (10) (2016) 822.

[50] D. M. Deery, G. J. Rebetzke, J. A. Jimenez-Berni, R. A. James, A. G. Condon, W. D. Bovill, P. Hutchinson, J. Scarrow, R. Davy, R. T. Furbank, Methodology for high-throughput field phenotyping of canopy temperature using airborne thermography, Frontiers in Plant Science 7 (2016) 1808.

[51] D. Wang, J. Gartung, Infrared canopy temperature of early-ripening peach trees under postharvest deficit irrigation, Agricultural Water Management 97 (11) (2010) 1787–1794.

[52] J. Escalona, J. Flexas, H. Medrano, Drought effects on water flow, photosynthesis and growth of potted grapevines, Vitis 41 (2) (2002) 57–62.

[53] C. Poblete-Echeverría, S. Ortega-Farias, Evaluation of single and dual crop coefficients over a drip-irrigated Merlot vineyard (Vitis vinifera L.) using combined measurements of sap flow sensors and an eddy covariance system, Australian Journal of Grape and Wine research 19 (2) (2013) 249–260.

[54] D. Intrigliolo, J. Castel, Evaluation of grapevine water status from trunk diameter variations, Irrigation Science 26 (1) (2007) 49–59.

[55] F. Jara-Rojas, S. Ortega-Farías, H. Valdés-Gómez, C. Acevedo-Opazo, Gas exchange relations of ungrafted grapevines (cv. carménère) growing under irrigated field conditions, South African Journal of Enology and Viticulture 36 (2) (2015) 231–242.

[56] C. Camino, P. J. Zarco-Tejada, V. Gonzalez-Dugo, Effects of heterogeneity within tree crowns on airborne-quantified SIF and the CWSI as indicators of water stress in the context of precision agriculture, Remote Sensing 10 (4) (2018) 604.

[57] D. Glenn, J. Worthington, W. Welker, M. McFarland, Estimation of peach tree water use using infrared thermometry, Journal of the American Society for Horticultural Science (USA).

[58] M. Sano, Y. Nakagawa, T. Sugimoto, T. Shirakawa, K. Yamagishi, T. Sugihara, M. Ohaba, S. Shibusawa, Estimation of water stress of plant by vibration measurement of leaf using acoustic radiation force, Acoustical Science and Technology 36 (3) (2015) 248–253.

[59] A. Tong, Y. He, Estimating and mapping chlorophyll content for a heterogeneous grassland: comparing prediction power of a suite of vegetation indices across scales between years, ISPRS Journal of Photogrammetry and Remote Sensing 126 (2017) 146–167.

[60] F. Boochs, G. Kupfer, K. Dockter, W. Kühbauch, Shape of the red edge as vitality indicator for plants, Remote Sensing 11 (10) (1990) 1741–1753.

[61] J. Peñuelas, J. Gamon, A. Fredeen, J. Merino, C. Field, Reflectance indices associated with physiological changes in nitrogen-and water-limited sunflower leaves, Remote Sensing of Environment 48 (2) (1994) 135–146.

[62] I. Filella, J. Penuelas, The red edge position and shape as indicators of plant chlorophyll content, biomass and hydric status., International Journal of Remote Sensing 15 (7) (1994) 1459–1470.

[63] J. Vogelmann, B. Rock, D. Moss, Red edge spectral measurements from sugar maple leaves, Remote Sensing 14 (8) (1993) 1563–1575.

[64] K. A. Smith, Soil and Environmental Analysis: Physical Methods, Revised, and Expanded, CRC Press, 2000.

[65] X. Chone, C. Van Leeuwen, D. Dubourdieu, J. P. Gaudillère, Stem water potential is a sensitive indicator of grapevine water status, Annals of Botany 87 (4) (2001) 477–483.

[66] H. G. Jones, Monitoring plant and soil water status: established and novel methods revisited and their relevance to studies of drought tolerance, Journal of Experimental Botany 58 (2) (2006) 119–130.

[67] K. A. Shackel, H. Ahmadi, W. Biasi, R. Buchner, D. Goldhamer, S. Gurusinghe, J. Hasey, D. Kester, B. Krueger, B. Lampinen, et al., Plant water status as an index of irrigation need in deciduous fruit trees, HortTechnology 7 (1) (1997) 23–29.

[68] P. F. Scholander, H. Hammel, E. Hemmingsen, E. Bradstreet, Hydrostatic pressure and osmotic potential in leaves of mangroves and some other plants, Proceedings of the National Academy of Sciences 52 (1) (1964) 119–125.

[69] M. Moran, T. Clarke, Y. Inoue, A. Vidal, Estimating crop water deficit using the relation between surface-air temperature and spectral vegetation index, Remote Sensing of Environment 49 (3) (1994) 246–263.

[70] C. Acevedo-Opazo, B. Tisseyre, S. Guillaume, H. Ojeda, The potential of high spatial resolution information to define within-vineyard zones related to vine water status, Precision Agriculture 9 (5) (2008) 285–302.

[71] J. Baluja, M. P. Diago, P. Balda, R. Zorer, F. Meggio, F. Morales, J. Tardaguila, Assessment of vineyard water status variability by thermal and multispectral imagery using an unmanned aerial vehicle (UAV), Irrigation Science 30 (6) (2012) 511–522.

[72] S. Ortega-Farías, S. Ortega-Salazar, T. Poblete, A. Kilic, R. Allen, C. Poblete-Echeverría, L. Ahumada-Orellana, M. Zuñiga, D. Sepúlveda, Estimation of energy balance components over a drip-irrigated olive orchard using thermal and multispectral cameras placed on a helicopter-based unmanned aerial vehicle (UAV), Remote Sensing 8 (8) (2016) 638.

[73] S. Idso, R. Jackson, P. Pinter Jr, R. Reginato, J. Hatfield, Normalizing the stress-degree-day parameter for environmental variability, Agricultural Meteorology 24 (1981) 45–55.

[74] J. Bellvert, J. Marsal, J. Girona, V. Gonzalez-Dugo, E. Fereres, S. L. Ustin, P. J. Zarco-Tejada, Airborne thermal imagery to detect the seasonal evolution of crop water status in peach, nectarine and saturn peach orchards, Remote Sensing 8 (1) (2016) 39.

[75] V. Gonzalez-Dugo, D. Goldhamer, P. Zarco-Tejada, E. Fereres, Improving the precision of irrigation in a pistachio farm using an unmanned airborne thermal system, Irrigation Science 33 (1) (2015) 43–52.

[76] V. Gonzalez-Dugo, P. Zarco-Tejada, J. A. Berni, L. Suárez, D. Goldhamer, E. Fereres, Almond tree canopy temperature reveals intra-crown variability that is water stress-dependent, Agricultural and Forest Meteorology 154 (2012) 156–165.

[77] L. E. Williams, T. J. Trout, Relationships among vine-and soil-based measures of water status in a Thompson Seedless vineyard in response to high-frequency drip irrigation, American Journal of Enology and Viticulture 56 (4) (2005) 357–366.

[78] J. Bellvert, P. Zarco-Tejada, J. Girona, E. Fereres, Mapping crop water stress index in a 'pinot-noir'vineyard: comparing ground measurements with thermal remote sensing imagery from an unmanned aerial vehicle UAV, Precision Agriculture 15 (4) (2014) 361–376.

[79] C. Ballester, M. Jiménez-Bello, J. R. Castel, D. S. Intrigliolo, Usefulness of thermography for plant water stress detection in citrus and persimmon trees, Agricultural and Forest Meteorology 168 (2013) 120–129.

[80] M. González-Dugo, M. Moran, L. Mateos, R. Bryant, Canopy temperature variability as an indicator of crop water stress severity, Irrigation Science 24 (4) (2006) 233.

[81] M. Möller, V. Alchanatis, Y. Cohen, M. Meron, J. Tsipris, A. Naor, V. Ostrovsky, M. Sprintsin, S. Cohen, Use of thermal and visible imagery for estimating crop water status of irrigated grapevine, Journal of Experimental Botany 58 (4) (2007) 827–838.

[82] M. Fuchs, Infrared measurement of canopy temperature and detection of plant water stress, Theoretical and Applied Climatology 42 (4) (1990) 253–261.

[83] B. Gardner, B. Blad, D. Watts, Plant and air temperatures in differentially-irrigated corn, Agricultural Meteorology 25 (1981) 207–217.

[84] M. Li, R. Chu, Q. Yu, A. R. M. T. Islam, S. Chou, S. Shen, Evaluating structural, chlorophyll-based and photochemical indices to detect summer maize responses to continuous water stress, Water 10 (4) (2018) 500.

[85] C. Ballester, P. Zarco-Tejada, E. Nicolás, J. Alarcón, E. Fereres, D. Intrigliolo, V. Gonzalez-Dugo, Evaluating the performance of xanthophyll, chlorophyll and structure-sensitive spectral indices to detect water stress in five fruit tree species, Precision Agriculture 19 (1) (2018) 178–193.

[86] J. Gamon, L. Serrano, J. Surfus, The photochemical reflectance index: an optical indicator of photosynthetic radiation use efficiency across species, functional types, and nutrient levels, Oecologia 112 (4) (1997) 492–501.

[87] D. Haboudane, J. R. Miller, N. Tremblay, P. J. Zarco-Tejada, L. Dextraze, Integrated narrow-band vegetation indices for prediction of crop chlorophyll content for application to precision agriculture, Remote Eensing of Environment 81 (2-3) (2002) 416–426.

[88] M. Rossini, F. Fava, S. Cogliati, M. Meroni, A. Marchesi, C. Panigada, C. Giardino, L. Busetto, M. Migliavacca, S. Amaducci, et al., Assessing canopy

PRI from airborne imagery to map water stress in maize, ISPRS Journal of Photogrammetry and Remote Sensing 86 (2013) 168–177.

[89] I. Moya, L. Camenen, S. Evain, Y. Goulas, Z. Cerovic, G. Latouche, J. Flexas, A. Ounis, A new instrument for passive remote sensing: 1. measurements of sunlight-induced chlorophyll fluorescence, Remote Sensing of Environment 91 (2) (2004) 186–197.

[90] M. Meroni, R. Colombo, Leaf level detection of solar induced chlorophyll fluorescence by means of a subnanometer resolution spectroradiometer, Remote Sensing of Environment 103 (4) (2006) 438–448.

[91] O. Pérez-Priego, P. J. Zarco-Tejada, J. R. Miller, G. Sepulcre-Cantó, E. Fereres, Detection of water stress in orchard trees with a high-resolution spectrometer through chlorophyll fluorescence in-filling of the O_2-A band, IEEE Transactions on Geoscience and Remote Sensing 43 (12) (2005) 2860–2869.

[92] A. Damm, A. Erler, W. Hillen, M. Meroni, M. E. Schaepman, W. Verhoef, U. Rascher, Modeling the impact of spectral sensor configurations on the FLD retrieval accuracy of sun-induced chlorophyll fluorescence, Remote Sensing of Environment 115 (8) (2011) 1882–1892.

[93] P. Martí, M. Gasque, P. GonzáLez-Altozano, An artificial neural network approach to the estimation of stem water potential from frequency domain reflectometry soil moisture measurements and meteorological data, Computers and Electronics in Agriculture 91 (2013) 75–86.

[94] T. Poblete, S. Ortega-Farías, M. A. Moreno, M. Bardeen, Artificial neural network to predict vine water status spatial variability using multispectral information obtained from an unmanned aerial vehicle (UAV), Sensors 17 (11) (2017) 2488.

[95] M. Romero, Y. Luo, B. Su, S. Fuentes, Vineyard water status estimation using multispectral imagery from an UAV platform and machine learning algorithms for irrigation scheduling management, Computers and Electronics in Agriculture 147 (2018) 109–117.

[96] C. M. Bishop, Neural Networks for Pattern Recognition, Oxford University Press, 1995.

[97] A. J. Richardson, J. H. Everitt, Using spectral vegetation indices to estimate rangeland productivity, Geocarto International 7 (1) (1992) 63–69.

[98] M.-F. Courel, P. C. Chamard, M. Guenegou, J. Lerhun, J. Levasseur, M. Togola, Utilisation des bandes spectrales du vert et du rouge pour une meilleure évaluation des formations végétales actives, in: Congrès AUPELF-UREF, 1991.

[99] J. Qi, A. Chehbouni, A. Huete, Y. Kerr, S. Sorooshian, A modified soil adjusted vegetation index, Remote Sensing of Environment 48 (2) (1994) 119–126.

[100] J. Rouse Jr, R. Haas, J. Schell, D. Deering, Monitoring vegetation systems in the great plains with ERTS, in: the Proceedings of Third Symposium on Significant Results Obtained from the First Earth Resources Technology Satellite, Vol. 1, 1974, pp. 309–317.

[101] J. Gamon, J. Surfus, Assessing leaf pigment content and activity with a reflectometer, The New Phytologist 143 (1) (1999) 105–117.

[102] E. Barnes, T. Clarke, S. Richards, P. Colaizzi, J. Haberland, M. Kostrzewski, P. Waller, C. Choi, E. Riley, T. Thompson, et al., Coincident detection of crop water stress, nitrogen status and canopy density using ground based multispectral data, in: the Proceedings of the Fifth International Conference on Precision Agriculture, Bloomington, Minnesota, USA, Vol. 1619, 2000.

[103] G. Rondeaux, M. Steven, F. Baret, Optimization of soil-adjusted vegetation indices, Remote Sensing of Environment 55 (2) (1996) 95–107.

[104] J.-L. Roujean, F.-M. Breon, Estimating PAR absorbed by vegetation from bidirectional reflectance measurements, Remote Sensing of Environment 51 (3) (1995) 375–384.

[105] G. S. Birth, G. R. McVey, Measuring the color of growing turf with a reflectance spectrophotometer 1, Agronomy Journal 60 (6) (1968) 640–643.

[106] J. A. Moran, A. K. Mitchell, G. Goodmanson, K. A. Stockburger, Differentiation among effects of nitrogen fertilization treatments on conifer seedlings by foliar reflectance: a comparison of methods, Tree Physiology 20 (16) (2000) 1113–1120.

[107] J. Thomas, H. Gausman, Leaf reflectance vs. leaf chlorophyll and carotenoid concentrations for eight crops 1, Agronomy Journal 69 (5) (1977) 799–802.

[108] J. Penuelas, F. Baret, I. Filella, Semi-empirical indices to assess carotenoids/chlorophyll a ratio from leaf spectral reflectance, Photosynthetica 31 (2) (1995) 221–230.

[109] M. Maimaitiyiming, A. Ghulam, A. Bozzolo, J. L. Wilkins, M. T. Kwasniewski, Early detection of plant physiological responses to different levels of water stress using reflectance spectroscopy, Remote Sensing 9 (7) (2017) 745.

[110] A. R. Huete, A soil-adjusted vegetation index (SAVI), Remote Sensing of Environment 25 (3) (1988) 295–309.

[111] C. D. Elvidge, R. J. Lyon, Influence of rock-soil spectral variation on the assessment of green biomass, Remote Sensing of Environment 17 (3) (1985) 265–279.

[112] A. Huete, R. Jackson, D. Post, Spectral response of a plant canopy with different soil backgrounds, Remote Sensing of Environment 17 (1) (1985) 37–53.

[113] J. E. Colwell, Vegetation canopy reflectance, Remote Sensing of Environment 3 (3) (1974) 175–183.

[114] F. Baret, G. Guyot, Potentials and limits of vegetation indices for LAI and APAR assessment, Remote Sensing of Environment 35 (2-3) (1991) 161–173.

[115] M. Gilabert, J. González-Piqueras, F. Garcıa-Haro, J. Meliá, A generalized soil-adjusted vegetation index, Remote Sensing of Environment 82 (2-3) (2002) 303–310.

[116] R. Rud, M. Shoshany, V. Alchanatis, Spatial–spectral processing strategies for detection of salinity effects in cauliflower, aubergine and kohlrabi, Biosystems Engineering 114 (4) (2013) 384–396.

[117] R. Rud, Y. Cohen, V. Alchanatis, A. Levi, R. Brikman, C. Shenderey, B. Heuer, T. Markovitch, Z. Dar, C. Rosen, et al., Crop water stress index derived from multi-year ground and aerial thermal images as an indicator of potato water status, Precision Agriculture 15 (3) (2014) 273–289.

[118] M. Meron, J. Tsipris, V. Orlov, V. Alchanatis, Y. Cohen, Crop water stress mapping for site-specific irrigation by thermal imagery and artificial reference surfaces, Precision Agriculture 11 (2) (2010) 148–162.

[119] T. N. Carlson, D. A. Ripley, On the relation between NDVI, fractional vegetation cover, and leaf area index, Remote Sensing of Environment 62 (3) (1997) 241–252.

[120] R. Ballesteros, J. Ortega, D. Hernández, M. Moreno, Applications of georeferenced high-resolution images obtained with unmanned aerial vehicles. part i:

Description of image acquisition and processing, Precision Agriculture 15 (6) (2014) 579–592.

[121] Y. Cohen, V. Alchanatis, A. Prigojin, A. Levi, V. Soroker, Use of aerial thermal imaging to estimate water status of palm trees, Precision Agriculture 13 (1) (2012) 123–140.

[122] N. Kerle, L. L. Janssen, G. C. Huurneman, Principles of remote sensing, ITC, Educational Textbook Series 2 (2004) 250.

[123] J. Shell, Bidirectional Reflectance: An Overview with Remote Sensing Applications & Measurement Recommendations, Rochester NY, 2004.

[124] R. Smith, Introduction to remote sensing of environment (RSE), `http://www.hesc.it/tnt/tutorial/introrse-ENG.pdf` (2001).

[125] C. A. F. Ezequiel, M. Cua, N. C. Libatique, G. L. Tangonan, R. Alampay, R. T. Labuguen, C. M. Favila, J. L. E. Honrado, V. Canos, C. Devaney, et al., UAV aerial imaging applications for post-disaster assessment, environmental management and infrastructure development, in: the Proceedings of 2014 International Conference on Unmanned Aircraft Systems (ICUAS2014), Orlando, Florida, USA, IEEE, 2014, pp. 274–283.

[126] I. Colomina, P. Molina, Unmanned aerial systems for photogrammetry and remote sensing: A review, ISPRS Journal of Photogrammetry and Remote Sensing 92 (2014) 79–97.

[127] C. A. Rokhmana, The potential of UAV-based remote sensing for supporting precision agriculture in Indonesia, Procedia Environmental Sciences 24 (2015) 245–253.

[128] K. Kakaes, F. Greenwood, M. Lippincot, S. Dosemagen, P. Meier, S. Wich, Drones and aerial observation: New technologies for property rights, human rights, and global development: A primer, New America (2015) 6–103.

[129] W. Philpot, Topic 4: Geometric correction, `http://ceeserver.cee.cornell.edu/wdp2/cee6150/Monograph/615_04_GeomCorrect_rev01.pdf` (2018).

[130] J. A. Richards, Remote Sensing Digital Image Analysis, Vol. 3, Springer, 1999.

[131] Japan Association of Remote Sensing, Remote sensing notes, `http://wtlab.iis.u-tokyo.ac.jp/wataru/lecture/rsgis/rsnote/cp9/cp9-1.htm` (1999).

[132] C. Wang, S. W. Myint, A simplified empirical line method of radiometric calibration for small unmanned aircraft systems-based remote sensing, IEEE Journal of Selected Topics in Applied Earth Observations and Remote Sensing 8 (5) (2015) 1876–1885.

[133] R. Ryan, M. Pagnutti, Enhanced absolute and relative radiometric calibration for digital aerial cameras, in: Photogrammetric Week, 2009.

[134] Y. Zhang, L. Zhang, X. Yu, Region of interest extraction based on multiscale visual saliency analysis for remote sensing images, Journal of Applied Remote Sensing 9 (1) (2015) 095050.

[135] G. Chen, Q. Weng, G. J. Hay, Y. He, Geographic object-based image analysis (GEOBIA): emerging trends and future opportunities, GIScience & Remote Sensing 55 (2) (2018) 159–182.

[136] A. Schlamm, D. Messinger, W. Basener, Interest segmentation of large area spectral imagery for analyst assistance, IEEE Journal of Selected Topics in Applied Earth Observations and Remote Sensing 5 (2) (2012) 409–420.

[137] T. Li, J. Zhang, X. Lu, Y. Zhang, SDBD: A hierarchical region-of-interest detection approach in large-scale remote sensing image, IEEE Geoscience and Remote Sensing Letters 14 (5) (2017) 699–703.

[138] J. Schiewe, Segmentation of high-resolution remotely sensed data-concepts, applications and problems, International Archives of Photogrammetry Remote Sensing and Spatial Information Sciences 34 (4) (2002) 380–385.

[139] T. Zhao, Z. Wang, Q. Yang, Y. Chen, Melon yield prediction using small unmanned aerial vehicles, in: the Proceedings of Autonomous Air and Ground Sensing Systems for Agricultural Optimization and Phenotyping II, Anaheim, California, USA, Vol. 10218, International Society for Optics and Photonics, 2017, p. 1021808.

[140] Y. Yang, S. Hallman, D. Ramanan, C. C. Fowlkes, Layered object models for image segmentation, IEEE Transactions on Pattern Analysis and Machine Intelligence 34 (9) (2012) 1731–1743.

[141] L. Johnson, T. Scholasch, Remote sensing of shaded area in vineyards, HortTechnology 15 (4) (2005) 859–863.

[142] J. Llorens, E. Gil, J. Llop, et al., Ultrasonic and LIDAR sensors for electronic canopy characterization in vineyards: Advances to improve pesticide application methods, Sensors 11 (2) (2011) 2177–2194.

[143] R. R. Sola-Guirado, F. J. Castillo-Ruiz, F. Jiménez-Jiménez, G. L. Blanco-Roldan, S. Castro-Garcia, J. A. Gil-Ribes, Olive actual "on year" yield forecast tool based on the tree canopy geometry using UAS imagery, Sensors 17 (8) (2017) 1743.

[144] A. N. Skurikhin, S. R. Garrity, N. G. McDowell, D. M. Cai, Automated tree crown detection and size estimation using multi-scale analysis of high-resolution satellite imagery, Remote Sensing Letters 4 (5) (2013) 465–474.

[145] K. Karantzalos, D. Argialas, Towards automatic olive tree extraction from satellite imagery, in: Geo-Imagery Bridging Continents. XXth ISPRS Congress, Citeseer, 2004, pp. 12–23.

[146] S. Peedell, S. Kay, G. Giordino, Computer-assisted recognition of olive trees in digital imagery, Space Application Institute, Joint Research Center of Ispra, Italy, 2000.

[147] J.-D. Jang, V. Payan, A. Viau, A. Devost, The use of airborne lidar for orchard tree inventory, International Journal of Remote Sensing 29 (6) (2008) 1767–1780.

[148] J. Hyyppa, O. Kelle, M. Lehikoinen, M. Inkinen, A segmentation-based method to retrieve stem volume estimates from 3-D tree height models produced by laser scanners, IEEE Transactions on Geoscience and Remote Sensing 39 (5) (2001) 969–975.

[149] Y. She, R. Ehsani, J. Robbins, J. N. Leiva, J. Owen, Applications of small UAV systems for tree and nursery inventory management, in: the Proceedings of the 12th International Conference on Precision Agriculture, Sacramento, California, USA, 2014, pp. 20–23.

[150] D. S. Culvenor, TIDA: an algorithm for the delineation of tree crowns in high spatial resolution remotely sensed imagery, Computers & Geosciences 28 (1) (2002) 33–44.

[151] R. G. Allen, L. S. Pereira, D. Raes, M. Smith, et al., Crop evapotranspiration-guidelines for computing crop water requirements-FAO irrigation and drainage paper 56, FAO, Rome 300 (9) (1998) D05109.

[152] N. Otsu, A threshold selection method from gray-level histograms, IEEE Transactions on Systems, Man, and Cybernetics 9 (1) (1979) 62–66.

[153] R. C. Gonzalez, R. E. Woods, et al., Digital Image Processing, Prentice Hall New Jersey, 2002.

[154] D. Guru, Y. Sharath, S. Manjunath, Texture features and KNN in classification of flower images, IJCA, Special Issue on RTIPPR (1) (2010) 21–29.

[155] F. Albregtsen, et al., Statistical texture measures computed from gray level coocurrence matrices, Image Processing Laboratory, Department of Informatics, University of Oslo 5.

[156] R. M. Haralick, K. Shanmugam, et al., Textural features for image classification, IEEE Transactions on Systems, Man, and Cybernetics (6) (1973) 610–621.

[157] S. D. Newsam, C. Kamath, Retrieval using texture features in high-resolution multispectral satellite imagery, in: the Proceedings of Data Mining and Knowledge Discovery: Theory, Tools, and Technology VI, Orlando, Florida, USA, Vol. 5433, International Society for Optics and Photonics, 2004, pp. 21–33.

[158] X. Wu, V. Kumar, J. R. Quinlan, J. Ghosh, Q. Yang, H. Motoda, G. J. McLachlan, A. Ng, B. Liu, S. Y. Philip, et al., Top 10 algorithms in data mining, Knowledge and Information Systems 14 (1) (2008) 1–37.

[159] T. Cover, P. Hart, Nearest neighbor pattern classification, IEEE Transactions on Information Theory 13 (1) (1967) 21–27.

[160] Y. LeCun, Y. Bengio, G. Hinton, Deep learning, Nature 521 (7553) (2015) 436.

[161] S. Ren, K. He, R. Girshick, J. Sun, Faster R-CNN: Towards real-time object detection with region proposal networks, in: Advances in Neural Information Processing Systems, 2015, pp. 91–99.

[162] J. Long, E. Shelhamer, T. Darrell, Fully convolutional networks for semantic segmentation, in: the Proceedings of the IEEE Conference on Computer Vision and Pattern Recognition (CVPR2015), Boston, Massachusetts, USA, 2015, pp. 3431–3440.

[163] T. Zhao, H. Niu, E. de la Rosa, D. Doll, D. Wang, Y. Chen, Tree canopy differentiation using instance-aware semantic segmentation, in: the Proceedings of 2018 ASABE Annual International Meeting, Detroit, Michigan, USA, American Society of Agricultural and Biological Engineers, 2018, p. 1.

[164] K. He, G. Gkioxari, P. Dollár, R. Girshick, Mask R-CNN, in: the Proceedings of the IEEE International Conference on Computer Vision (ICCV2017), Venice, Italy, IEEE, 2017, pp. 2980–2988.

[165] J. Dai, K. He, Y. Li, S. Ren, J. Sun, Instance-sensitive fully convolutional networks, in: the Proceedings of the European Conference on Computer Vision (ECCV2016), Amsterdam, Netherlands, Springer, 2016, pp. 534–549.

[166] Y. Li, H. Qi, J. Dai, X. Ji, Y. Wei, Fully convolutional instance-aware semantic segmentation, arXiv preprint arXiv:1611.07709.

[167] V. Kulikov, V. Yurchenko, V. Lempitsky, Instance segmentation by deep coloring, arXiv preprint arXiv:1807.10007.

[168] M. Everingham, L. Van Gool, C. K. I. Williams, J. Winn, A. Zisserman, The PASCAL Visual Object Classes Challenge 2012 (VOC2012) Results, http://www.pascal-network.org/challenges/VOC/voc2012/workshop/index.html.

[169] E. Triantafillou, R. Zemel, R. Urtasun, Few-shot learning through an information retrieval lens, in: the Proceedings of Advances in Neural Information Processing Systems, Long Beach, California, USA, 2017, pp. 2255–2265.

[170] A. Shaban, S. Bansal, Z. Liu, I. Essa, B. Boots, One-shot learning for semantic segmentation, arXiv preprint arXiv:1709.03410.

[171] A. R. Zamir, A. Sax, W. Shen, L. Guibas, J. Malik, S. Savarese, Taskonomy: Disentangling task transfer learning, in: the Proceedings of the IEEE Conference on Computer Vision and Pattern Recognition (CVPR2018), Honolulu, Hawaii, USA, 2018, pp. 3712–3722.

[172] J. Gago, C. Douthe, R. Coopman, P. Gallego, M. Ribas-Carbo, J. Flexas, J. Escalona, H. Medrano, UAVs challenge to assess water stress for sustainable agriculture, Agricultural Water Management 153 (2015) 9–19.

[173] C. Romero-Trigueros, P. A. Nortes, J. J. Alarcón, J. E. Hunink, M. Parra, S. Contreras, P. Droogers, E. Nicolás, Effects of saline reclaimed waters and deficit irrigation on citrus physiology assessed by UAV remote sensing, Agricultural Water Management 183 (2017) 60–69.

[174] E. S. Köksal, Y. Güngör, Y. E. Yildirim, Spectral reflectance characteristics of sugar beet under different levels of irrigation water and relationships between growth parameters and spectral indexes, Irrigation and Drainage 60 (2) (2011) 187–195.

[175] J. Farifteh, R. R. Struthers, R. Swennen, P. Coppin, Plant spectral and thermal responses to water stress induced by regulated deficit irrigation, International Journal of Geosciences and Geomatics 1 (1) (2013) 17–22.

[176] J. L. Hatfield, J. H. Prueger, Value of using different vegetative indices to quantify agricultural crop characteristics at different growth stages under varying management practices, Remote Sensing 2 (2) (2010) 562–578.

[177] A. Matese, P. Toscano, S. F. Di Gennaro, L. Genesio, F. P. Vaccari, J. Primicerio, C. Belli, A. Zaldei, R. Bianconi, B. Gioli, Intercomparison of UAV, aircraft and satellite remote sensing platforms for precision viticulture, Remote Sensing 7 (3) (2015) 2971–2990.

[178] H. Zheng, X. Zhou, T. Cheng, X. Yao, Y. Tian, W. Cao, Y. Zhu, Evaluation of a UAV-based hyperspectral frame camera for monitoring the leaf nitrogen concentration in rice, in: the Proceedings of 2016 IEEE International Conference on Geoscience and Remote Sensing Symposium (IGARSS2016), IEEE, 2016, pp. 7350–7353.

[179] F. Pedregosa, G. Varoquaux, A. Gramfort, V. Michel, B. Thirion, O. Grisel, M. Blondel, P. Prettenhofer, R. Weiss, V. Dubourg, J. Vanderplas, A. Passos, D. Cournapeau, M. Brucher, M. Perrot, E. Duchesnay, Scikit-learn: Machine learning in Python, Journal of Machine Learning Research 12 (2011) 2825–2830.

[180] W. H. Press, S. A. Teukolsky, W. T. Vetterling, B. P. Flannery, Numerical Recipes 3rd Edition: the Art of Scientific Computing, Cambridge University Press, 2007.

[181] S. Dean, B. Illowsky, Descriptive statistics: skewness and the mean, median, and mode, Connexions website.

[182] P. H. Westfall, Kurtosis as peakedness, 1905–2014. RIP, The American Statistician 68 (3) (2014) 191–195.

[183] M. Welling, Fisher linear discriminant analysis, Department of Computer Science, University of Toronto 3 (1), 2005.

[184] S. Agatonovic-Kustrin, R. Beresford, Basic concepts of artificial neural network (ANN) modeling and its application in pharmaceutical research, Journal of Pharmaceutical and Biomedical Analysis 22 (5) (2000) 717–727.

[185] D. E. Rumelhart, G. E. Hinton, R. J. Williams, Learning representations by back-propagating errors, Nature 323 (6088) (1986) 533.

[186] E. Alpaydin, Introduction to Machine Learning, MIT Press, 2009.

[187] S.-H. Cha, Comprehensive survey on distance/similarity measures between probability density functions, City 1 (2) (2007) 1.

[188] V. Vaithiyanathan, K. D. Lakshmi, K. J. A. Sundar, M. I. Ahmed, V. Sangeetha, R. Sivagami, Evaluation of distance functions for the comparison of gradient orientation histograms, Indian Journal of Science and Technology 8 (35).

[189] H. Duda, P. E. Hart, G. David, Pattern Classification, John Wiley & Sons, 2001.

[190] P. A. Marín-Reyes, J. Lorenzo-Navarro, M. Castrillón-Santana, Comparative study of histogram distance measures for re-identification, arXiv preprint arXiv:1611.08134.

[191] T. Sørensen, A method of establishing groups of equal amplitude in plant sociology based on similarity of species and its application to analyses of the vegetation on Danish commons, Biol. Skr. 5 (1948) 1–34.

[192] D. Francois, V. Wertz, M. Verleysen, The concentration of fractional distances, IEEE Transactions on Knowledge and Data Engineering 19 (7) (2007) 873–886.

[193] M.-M. Deza, E. Deza, Dictionary of Distances, Elsevier, 2006.

[194] D. G. Gavin, W. W. Oswald, E. R. Wahl, J. W. Williams, A statistical approach to evaluating distance metrics and analog assignments for pollen records, Quaternary Research 60 (3) (2003) 356–367.

[195] S. Kullback, R. A. Leibler, On information and sufficiency, The Annals of Mathematical Statistics 22 (1) (1951) 79–86.

[196] R. De Maesschalck, D. Jouan-Rimbaud, D. L. Massart, The Mahalanobis distance, Chemometrics and Intelligent Laboratory Systems 50 (1) (2000) 1–18.

[197] M. M. Verstraete, B. Pinty, Designing optimal spectral indexes for remote sensing applications, IEEE Transactions on Geoscience and Remote Sensing 34 (5) (1996) 1254–1265.

[198] A. L. Nguy-Robertson, Y. Peng, A. A. Gitelson, T. J. Arkebauer, A. Pimstein, I. Herrmann, A. Karnieli, D. C. Rundquist, D. J. Bonfil, Estimating green LAI in four crops: Potential of determining optimal spectral bands for a universal algorithm, Agricultural and Forest Meteorology 192 (2014) 140–148.

[199] B. Stark, Y. Chen, A framework of optimal remote sensing using small unmanned aircraft systems, in: the Proceedings of 2016 12th IEEE/ASME International Conference on Mechatronic and Embedded Systems and Applications (MESA2016), Auckland, New Zealand, IEEE, 2016, pp. 1–6.

[200] B. Zitova, J. Flusser, Image registration methods: a survey, Image and Vision Computing 21 (11) (2003) 977–1000.

[201] Y. Ye, J. Shan, L. Bruzzone, L. Shen, Robust registration of multimodal remote sensing images based on structural similarity, IEEE Transactions on Geoscience and Remote Sensing 55 (5) (2017) 2941–2958.

[202] M. A. Goforth, Sub-pixel registration assessment of multispectral imagery, in: the Proceedings of Imaging Spectrometry XI, Vol. 6302, International Society for Optics and Photonics, 2006, p. 63020S.

[203] Y. Xie, X. Xiong, J. J. Qu, N. Che, L. Wang, Sensitivity analysis of MODIS band-to-band registration characterization and its impact on the science data products, in: Remote Sensing and Modeling of Ecosystems for Sustainability IV, Vol. 6679, International Society for Optics and Photonics, 2007, p. 667908.

[204] H. Tran, R. Tam, A. Traboulsee, D. Li, Assessing the impact of image registration on texture analysis of MR images, Lect Notes Comput Sci 4190 (2006) 760–767.

[205] P. M. Patel, V. M. Shah, Image registration techniques: a comprehensive survey, International Journal of Innovative Research and Development, 2014.

[206] K. Chureesampant, J. Susaki, Automatic GCP extraction of fully polarimetric SAR images, IEEE Transactions on Geoscience and Remote Sensing 52 (1) (2014) 137–148.

[207] A. J. Mathews, A practical UAV remote sensing methodology to generate multispectral orthophotos for vineyards: estimation of spectral reflectance using compact digital cameras, International Journal of Applied Geospatial Research (IJAGR) 6 (4) (2015) 65–87.

[208] M. Sean, Image types: JPEG & TIFF files, `https://www.cambridgeincolour.com/tutorials/imagetypes.htm`.

[209] C. C. Lelong, P. Burger, G. Jubelin, B. Roux, S. Labbé, F. Baret, Assessment of unmanned aerial vehicles imagery for quantitative monitoring of wheat crop in small plots, Sensors 8 (5) (2008) 3557–3585.

[210] E. R. Hunt, M. Cavigelli, C. S. Daughtry, J. E. Mcmurtrey, C. L. Walthall, Evaluation of digital photography from model aircraft for remote sensing of crop biomass and nitrogen status, Precision Agriculture 6 (4) (2005) 359–378.

[211] V. Lebourgeois, A. Bégué, S. Labbé, B. Mallavan, L. Prévot, B. Roux, Can commercial digital cameras be used as multispectral sensors? a crop monitoring test, Sensors 8 (11) (2008) 7300–7322.

[212] S. Von Bueren, A. Burkart, A. Hueni, U. Rascher, M. Tuohy, I. Yule, Deploying four optical UAV-based sensors over grassland: challenges and limitations, Biogeosciences 12 (1) (2015) 163–175.

[213] L. Suárez, P. Zarco-Tejada, V. González-Dugo, J. Berni, E. Fereres, Detecting water stress in orchard crops using PRI from airborne imagery, in: the Proceedings of the 6th EARSeL SIG IS Workshop Imaging Spectroscopy: Innovative Tool for Scientific and Commercial Environmental Applications, Tel-Aviv, Israel, 2009, pp. 16–19.

[214] P. J. Zarco-Tejada, V. González-Dugo, L. Williams, L. Suárez, J. A. Berni, D. Goldhamer, E. Fereres, A PRI-based water stress index combining structural and chlorophyll effects: Assessment using diurnal narrow-band airborne imagery and the CWSI thermal index, Remote Sensing of Environment 138 (2013) 38–50.

[215] T. Zhao, B. Stark, Y. Chen, A. Ray, D. Doll, More reliable crop water stress quantification using small unmanned aerial systems (SUAS), IFAC-PapersOnLine 49 (16) (2016) 409–414.

[216] A. Fulton, J. Grant, R. Buchner, J. Connell, Using the pressure chamber for irrigation management in walnut, almond, and prune, Oakland: University of California Division of Agriculture and Natural Resources Publication 8503.

[217] J. Friedman, T. Hastie, R. Tibshirani, The Elements of Statistical Learning, Vol. 1, Springer Series in Statistics New York, NY, USA, 2001.

[218] S. De Jong, SIMPLS: an alternative approach to partial least squares regression, Chemometrics and Intelligent Laboratory Systems 18 (3) (1993) 251–263.

[219] B. J. Stark, Optimal remote sensing with small unmanned aircraft systems and risk management, Ph.D. thesis, UC Merced (2017).

[220] B. Stark, T. Zhao, Y. Chen, An analysis of the effect of the bidirectional reflectance distribution function on remote sensing imagery accuracy from small unmanned aircraft systems, in: the Proceedings of 2016 International Conference on Unmanned Aircraft Systems (ICUAS2016), Arlington, Virginia, USA, IEEE, 2016, pp. 1342–1350.

[221] N. Agam, E. Segal, A. Peeters, A. Levi, A. Dag, U. Yermiyahu, A. Ben-Gal, Spatial distribution of water status in irrigated olive orchards by thermal imaging, Precision Agriculture 15 (3) (2014) 346–359.

[222] R. Giuliani, J. Flore, Potential use of infra-red thermometry for the detection of water stress in apple trees, in: the Proceedings of III International Symposium on Irrigation of Horticultural Crops 537, Lisbon, Portugal, 1999, pp. 383–392.

[223] T. Zhao, Y. Chen, A. Ray, D. Doll, Quantifying almond water stress using unmanned aerial vehicles (UAVs): correlation of stem water potential and higher order moments of non-normalized canopy distribution, in: the Proceedings of ASME 2017 International Design Engineering Technical Conferences and Computers and Information in Engineering Conference, Cleveland, Ohio, USA, American Society of Mechanical Engineers, 2017, pp. V009T07A058–V009T07A058.

[224] T. Zhao, D. Doll, Y. Chen, Better almond water stress monitoring using fractional-order moments of non-normalized difference vegetation index, in: the Proceedings of 2017 ASABE Annual International Meeting, Spokane, Washington, USA, American Society of Agricultural and Biological Engineers, 2017, p. 1.

[225] S. Candiago, F. Remondino, M. De Giglio, M. Dubbini, M. Gattelli, Evaluating multispectral images and vegetation indices for precision farming applications from UAV images, Remote Sensing 7 (4) (2015) 4026–4047.

[226] D. Goldhamer, E. Fereres, et al., Simplified tree water status measurements can aid almond irrigation, California Agriculture 55 (3) (2001) 32–37.